Two-dimensional Glasses

by

Seyed Mahdi Sadjadi

A Dissertation Presented in Partial Fulfillment
of the Requirements for the Degree
Doctor of Philosophy

Approved June 2018 by the
Graduate Supervisory Committee:

Michael F. Thorpe, Chair
Oliver Beckstein
Kevin E. Schmidt
Michael M.J. Treacy

ARIZONA STATE UNIVERSITY

August 2018

ABSTRACT

The structure of glass has been the subject of many studies, however some details remained to be resolved. With the advancement of microscopic imaging techniques and the successful synthesis of two-dimensional materials, images of two-dimensional glasses (bilayers of silica) are now available, confirming that this glass structure closely follows the continuous random network model. These images provide complete in-plane structural information such as ring correlations, and intermediate range order and with computer refinement contain indirect information such as angular distributions, and tilting.

This dissertation reports the first work that integrates the actual atomic coordinates obtained from such images with structural refinement to enhance the extracted information from the experimental data. The correlations in the ring structure of silica bilayers are studied and it is shown that short-range and intermediate-range order exist in such networks. Special boundary conditions for finite experimental samples are designed so atoms in the bulk sense they are part of an infinite network. It is shown that bilayers consist of two identical layers separated by a symmetry plane and the tilted tetrahedra, two examples of added value through the structural refinement. Finally, the low-temperature properties of glasses in two dimensions are studied. This dissertation presents a new approach to find possible two-level systems in silica bilayers employing the tools of rigidity theory in isostatic systems.

To Azam, Mahmood, Varda, Mehrdad

ACKNOWLEDGMENTS

Yes, it does! It takes a village to finish Ph.D. and I would like to thank the people who made graduate school some of the best years of my life. First and foremost, I should thank my advisor Michael Thorpe for his academic and financial support. I am grateful to Mike for his dedication to my academic life, his advice and patience and our stimulating and fun discussions ranging from physics to politics. I cannot count how many times I am told how lucky I am to have Mike as my advisor and I have agreed, wholeheartedly, every single time.

I would like to thank my partner in life and science Varda F. Hagh. Varda has been a tremendous positive force in my life. I have been blessed with her intelligence, creativity, amazing sense of humor, deep insight to life, and her unconditional love and support. I have been fortunate to have many discussions with Varda about research, physics, and science throughout the years.

During my Ph.D. years, I had the privilege to work and collaborate with many great scientists. I should thank Mark wilson for our invaluable discussions that had a significant effect on me as a scientist. I sincerely thank Bob Connelly, Shlomo Gortler, Miranda Holmes-Cerfon, Meera Sitharam, Louis Theran, for our countless insightful discussions on mathematics and rigidity. I also thank Mike Treacy, David Drabold, Bishal Bhattarai and Avishek Kumar for teaching me about glasses and our invaluable discussions.

I thank the entire community at ASU Department of Physics and Center for Biological Physics (CBP) for being always supportive and helpful. In particular, I would like to thank Peter Bennett to give me the opportunity to be part of ASU family, and Deanna Clark, Araceli Vizcarra, Deborah Denson, Jamie Severson, Ixchell Paape and Linda Raish for always patiently listening to the complicated requests of

an international student and making my life much easier. I also thank John Kazan, Taylor Colburn, Morteza Moghimi and Salman Seyedi.

I greatly appreciate the generosity of Department of Physics, Graduate and Professional Student Association, travel awards from ASU graduate college and APS, the dissertation fellowship of ASU graduate college, and NSF for financial support. Especially, I should remember and thank the late Bill Motil for his support through William J. and Carol M. Motil Scholarship. Any interaction with him and his passion for science was truly inspiring.

Last but not the least, I would like to extend my sincerest gratitude to my parents. They encouraged me from an early age to learn and never stop learning. They gave me the passion for knowledge as a gift and I am always thankful to them. Many thanks for your unconditional support, and many sacrifices. I also thank my brother who always believes in me and makes me laugh.

TABLE OF CONTENTS

CHAPTER Page

LIST OF TABLES

LIST OF FIGURES

Figure Page

Figure Page

Figure Page

Figure Page

Figure Page

Chapter 1

INTRODUCTION

Since the dawn of civilization, humans have developed tools to dominate and explore *nature* and their mastery at tool-making coupled with their creativity has paved the way to their advancement. It is, thus, not surprising that a large segment of our intellectual activity has been focused on the understanding of materials behavior.

In the last 100 years, we have witnessed a rapid growth in our understanding of materials and a paradigm shift from heuristic approaches to designer materials customized even at the atomic level. Glasses are among the materials with most applications. However, historically their structure has been the subject of various debates. The comparison between non-crystalline and crystalline materials can justify possible disagreements. Crystals are known as an ordered material with a (usually) small unit repeating in space. In crystals, the knowledge of unit cell, basis and its symmetry is sufficient to fully describe a crystal. The periodicity lends itself well to a rigorous mathematical formulation and reductionist style of physics to describe the properties of crystals. Such language is missing in non-crystalline materials and in addition, they have some properties that are not present in crystals. Two great examples are the thermal properties of glasses in low temperatures [11] and the excess of low-frequency vibrational modes [12]. This means that models have a greater significance in understanding glassy properties. In fact, an amorphous structure represents a degenerate state since uncountably many structures can generate observations that match our experimental data.

Modeling of glass dates back to more than 80 years ago and several models explain the experimental observations but many exciting advancements are yet to come.

The last two decades in materials physics is characterized by the great interest in two-dimensional (2D) materials. After the successful synthesis of graphene [13], researchers are determined to expand the library of 2D materials. Dimensionality can strongly impact the materials properties and indeed it has proven to be extremely important for glasses as recently microscopic imaging of archetypal glassy network-formers *i.e.* vitreous silica (a-SiO_2) [8, 4], and germania (a-GeO_2) [14] have shown. This is a remarkable breakthrough which allows us to look into the glass structure, independent of any model.

Here, the aim is to combine the experimental data with the mathematical and computational techniques to gain a better understanding of the glass structure. This dissertation is structured as follows. This chapter briefly reviews structural properties of glass and related topics. This is followed by a review of experimental and computational studies with a focus on recent breakthroughs in imaging of 2D glass. Chapter 2 will describe the correlations in the ring structure of the random networks. Chapter 3 will present a set of novel boundary conditions that are designed to maximize the available information from the experimental network glasses. The results of refining a 2D glass are given in Chapter 4. Finally, Chapter 5 discusses the low-temperature properties of glasses and our attempt to find geometrical signatures of tunneling states.

1.1 Theories of Glass Structure

The lack of periodicity in glasses comes at the cost of losing an exact formalism to describe their structures, and inevitably different models are presented to relate the glassy structures to the observed data. Historically, there have been two competing models for the structure of glass: crystallite theory, and continuous random network theory. In short, *crystallite theory* asserts that glass consists of many small crystalline

regions. *Random network* theory, however, states that glass is locally similar to crystals. On the short-range scales the interactions between atoms are the same, but due to variations in angles in which atoms bond, a disordered network is formed, with no micro-crystallites.

The history of crystallite theory goes back to 1835 where Frankenheim speculated that glass is made of very small crystalline regions (named *crystallites*) that vary in size [15]. This was about 81 years before the very first powder diffraction experiments performed by Debye and Scherrer in 1916 [16]. However, textbooks usually consider that Lebedev proposed this theory in 1921 [17].

Continuous random network (CRN) theory is also based on the similarity of crystals and glasses but only up to very short-range structure. CRN states that the nature of atomic bonding is the same for crystals and glasses which means in the case of oxide glasses such SiO_2, the tetrahedral SiO_4 can form a very large network but as opposed to crystals, these building blocks are joined at (somewhat) random angles which in turn leads to lack of long-range order and periodicity in glasses. This model is often attributed to Zachariasen [18] but in fact Rosenhain [19] was the first to suggest that due the directionality of (covalent) bonds, the glass is a network of randomly connected tetrahedral units. The network is not truly random since ordering exists both on short- and medium-range. But as Warren writes [2], the network is called *random* since "it does not repeat itself at regular intervals, and the material is accordingly noncrystalline." Essentially random is used as a synonym to noncrystalline[1].

Fig. 1.1 shows a two-dimensional diagram of A_2O_3 vitreous network as imagined by Zachariasen. The network consists of regular equilateral triangles (AO_3 blocks) that are connected with some local distortions eventually forming the ring structure

[1]The history of glass science, like glass, is very colorful and Ref. [20] by A.C. Wright is strongly recommended for more historical insights.

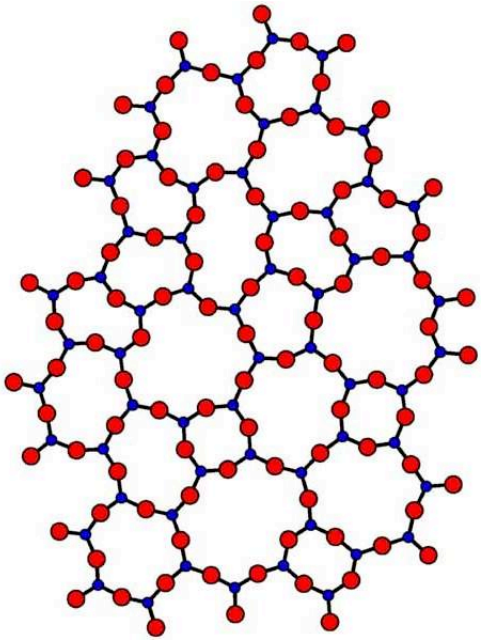

Figure 1.1: The original but colored Zachariasen's diagram of the planar glass A_2O_3 based on the continuous random network hypothesis as appeared in [1]. Red points are O atoms and blue points represent A atoms. This sketch is particularly interesting because of the meticulous drawing of regular AO_3 blocks which are equilateral triangles.

of the glass [21]. Therefore, we expect that short-range order in glass is very similar to crystalline silica. But the medium-range clearly exhibits signatures of glassy states as the way the tetrahedra are connecting is different. In addition, the ring structure also impacts the ordering at the intermediate range. Topological and geometrical correlations between rings from short- to long-range are studied in Chapter 2.

Order in amorphous solids is characterized by the correlation functions. If we know the position of all atoms, a conditional probability can be formed to quantify the probability of finding another atom in position **r** from a given atom. We can at least partially characterize the short-range order in well-studied materials such as silica. If the random network model is correct, we expect that distances between nearest atoms in glass are similar to that in quartz [22, 2]. Each silicon is surrounded by four oxygens at about 1.6Å, and four silicons at about 3.10Å. Therefore the probability of

finding any atom from a Si with the distance less than ~ 1.6Å is zero.

Correlation functions can be defined based on the number density of atoms. Let's assume that N atoms are confined in the volume V so that the average number density is $\rho_0 = N/V$. For a typical atom chosen at origin, the number density at position $\mathbf{r}$ is $\rho(\mathbf{r})$. For an isotropic medium such as glass: $\rho(\mathbf{r}) = \rho(r)$. Since the whole space contains N atoms:

$$N = \int_V \mathrm{d}V \rho(\mathbf{r}) = \int_V \mathrm{d}V \rho_0 g(r). \tag{1.1}$$

$g(r)$ measures the local deviation of the number density ρ from the average local density ρ_0 and is called the radial distribution function or more generally pair correlation function. Based on this equation, the average number of atoms $\mathrm{d}N(r)$ located within the volume element $\mathrm{d}V$ around r is:

$$\mathrm{d}N(r) = \rho_0 g(r) \mathrm{d}V. \tag{1.2}$$

This equation immediately provides an algorithm to compute $g(r)$. Take an atom as the origin and count the number of atoms located in volume dV at distance r. Repeat this process until all atoms are taken as the origin. Then take the average as the expected number of atoms at that distance. Note that if there is no correlation, the expected number of atoms is $\rho_0 \mathrm{d}V$ or $g(r) = 1$. In glasses, we expect that for sufficiently large distances, $g(r) \to 1$, similar to liquids since no long-range order is expected.

The radial distribution function of a two-dimensional glass with composition similar to Zachariasen diagram (Fig. 1.1, see also Fig. 1.6) is shown in Fig. 1.2. In this figure, Si atoms are selected as the origin and their distance to all other atoms (including Si and O) is calculated and averaged. Each peak corresponds to a high probability of finding an atom at that distance. The first peak in the radial distribution function corresponds to the spacing between Si and nearest O at around 1.6Å. The following

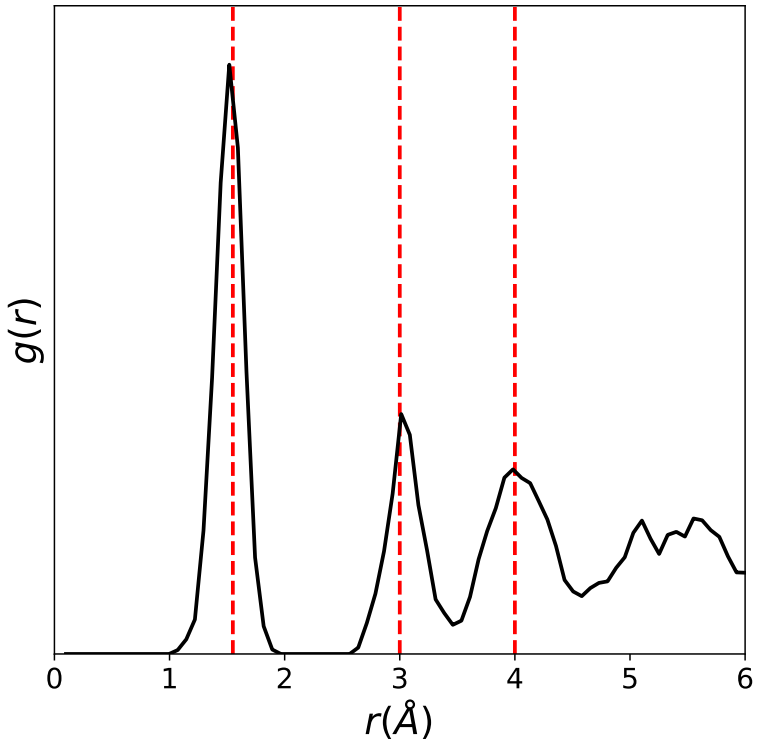

Figure 1.2: The radial distribution of two-dimensional Si_2O_3 (similar to Zachariasen's diagram). The three dashed lines are approximately drawn at 1.6, 3.0, and 4.0Å, respectively. The averaging is done assuming that only Si atoms are at the center but $g(r)$ is calculated for both Si and O atoms, with equal weighting.

peak occurs at ~ 3.0Å which is the distance between two Si atoms in the middle of two joined triangles. Note that triangles do not necessarily link at 180° to accommodate the ring closure and in addition the structure is a projection from 3D to 2D, therefore this distance is slightly less than 2×1.6Å. The third peak is located at 4.0Å and corresponds to the distance of a typical Si to the second-nearest O atoms on the non-joint corners of the linked triangles. These peaks are the signature of short-range ordering but at larger distances, peaks will gradually diminish and the atoms are free of correlations. At sufficiently large distances $g(r)$ tends to 1. In comparison, since the atoms in a crystal are located at deterministic positions, $g(r)$ would be a series of sharp peaks (delta functions), if atoms were stationary.

The radial distribution function is experimentally available as the Fourier transform of diffraction data. To gain any spatial information about the detailed structure, if the typical distance between atoms is a, then the scattering wave should have a wavelength λ comparable to this spacing which corresponds to a wavenumber of order $k \approx 2\pi/a$ which is in agreement with Bragg's law. As the atoms are separated by a few Å, x-ray or neutron scattering are the common techniques to probe the structure of glass. In experiments, the scattered intensity from atoms is the measurable quantity and depends on the local electron concentration. In general, two beams diffracted from two regions $\mathbf{r}$ apart, have a difference in the phase factor as $\exp(i(\mathbf{k}-\mathbf{k}').\mathbf{r})$ where $\mathbf{k}$ and $\mathbf{k}'$ are respectively the wavevectors of the incident and the diffracted beams. This means that the total scattered intensity depends on (static) structure factor S which in fact is the inverse Fourier transform of the radial distribution function:

$$S(\mathbf{k}-\mathbf{k}') = 1 + \rho_0 \int \mathrm{d}V\,[g(\mathbf{r})-1]\,e^{-i(\mathbf{k}-\mathbf{k}').\mathbf{r}}. \tag{1.3}$$

For an elastic scattering $|\mathbf{k}| = |\mathbf{k}'|$. If we define $\mathbf{q} = \mathbf{k} - \mathbf{k}'$, we can simplify the expression for an isotropic system. Since the integral over the volume element depends on the dimension, the structure factor takes different forms for 2D:

$$S(q) = 1 + 2\pi\rho_0 \int [g(r)-1]\,J_0(qr) r \mathrm{d}r \tag{1.4}$$

where $J_0(qr)$ is the zeroth order Bessel function of the first kind, and for 3D:

$$S(q) = 1 + 4\pi\rho_0 \int [g(r)-1] \left(\frac{\sin qr}{qr}\right) r^2 \mathrm{d}r. \tag{1.5}$$

Once the intensity measurements are done, the radial distribution is available through the inverse Fourier transform of the structure factor.

In 1934, Warren developed a method for analyzing the X−ray diffraction patterns of amorphous solids [2] based on the pioneering work of Debye and Scherrer [16] on

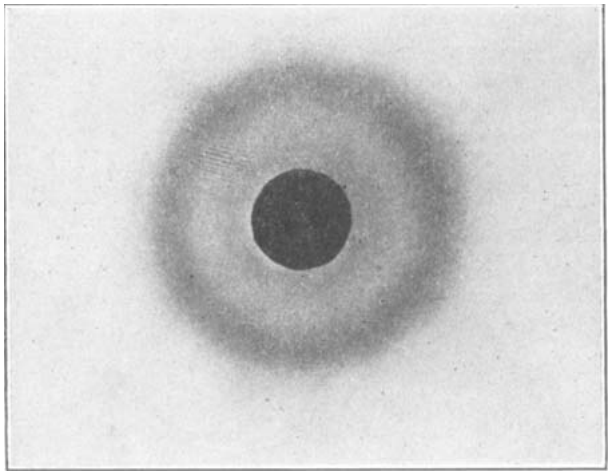

Figure 1.3: X-ray diffraction pattern of vitreous silica; Reproduced from [2].

powder diffraction. Prior to this work, numerous studies of x-ray diffraction from glass were reported but no serious attempt had been made to interpret the results ([2] and references therein). However, it was already established that the diffraction pattern of glass was reminiscent of liquids (Fig. 1.3). Warren compared the diffraction results to the predictions of crystallite and random network models. He confirmed the fact that in vitreous silica, each oxygen is shared between two tetrahedral units while each unit surrounds a silicon which was considered as evidence supporting the continuous random network model.

The diffraction experiments and the radial distribution function are important methods to study glassy structures but, in practice, cannot uncover all detailed structural information of amorphous systems. Firstly, ideas such as presented here do not include the atomic thermal vibrations in the analysis. In addition, experiments have a limited real-space resolution. Secondly, diffraction experiments can offer a single one-dimensional radial distribution function but there is no possible way to uniquely identify the actual structure of the glass generating the correlations. From this perspective, modeling of amorphous systems is an extremely important tool to gain far more detailed structural information.

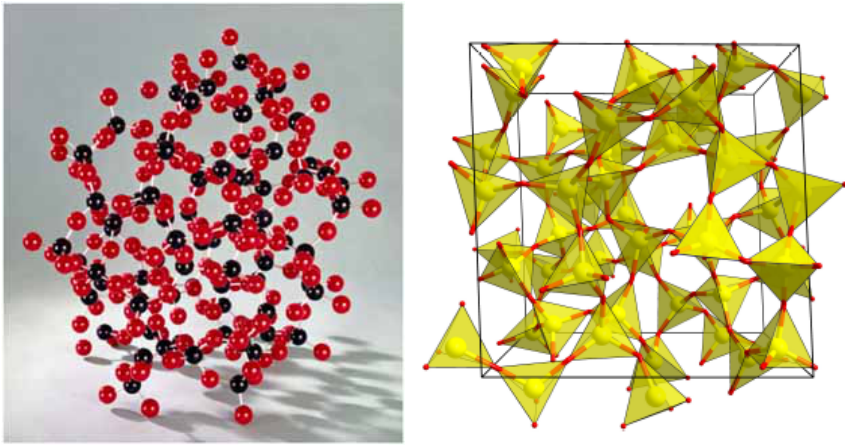

Figure 1.4: (Left) Part of Bell and Dean's 1972 model of vitreous silica, courtesy of the Science Museum, London. Reproduced from [1]. (Right) Computer-generated model of a-SiO_2 with periodic boundary conditions. Reproduced from [3].

Until 1960s, researchers were mostly focused on the interpretation of the experimental diffraction data based on two competing theories. Feasibility of such structures became only an issue during this decade. The research in this era were followed under two themes of (a) realization of glass in three dimensions and (b) consistency of such realizations with the diffraction data [20]. In December of 1966, Nature published two back-to-back papers, by Evans and King [23], and by Bell and Dean [24]. The papers were first reports of modeling of virtuous silica structure based on continuous random network model. Evans-King model with 1953 atoms was considerably larger then Bell-Dean model with 614 atoms (Fig. 1.4). While the Evans-King model is largely forgotten today, the Bell-Dean model is still highly cited[2] since they published the atomic coordinates of their model in 1972 [25].

Measurements in any reasonably large table-top model is tedious and soon researchers used molecular dynamics simulations to study the structure of glass in 1970s. Initial simulations were mostly two-body potentials including electrostatic and ionic interactions [26] but since the angular distributions (O-Si-O) did not match

[2]There is a lesson in this story!

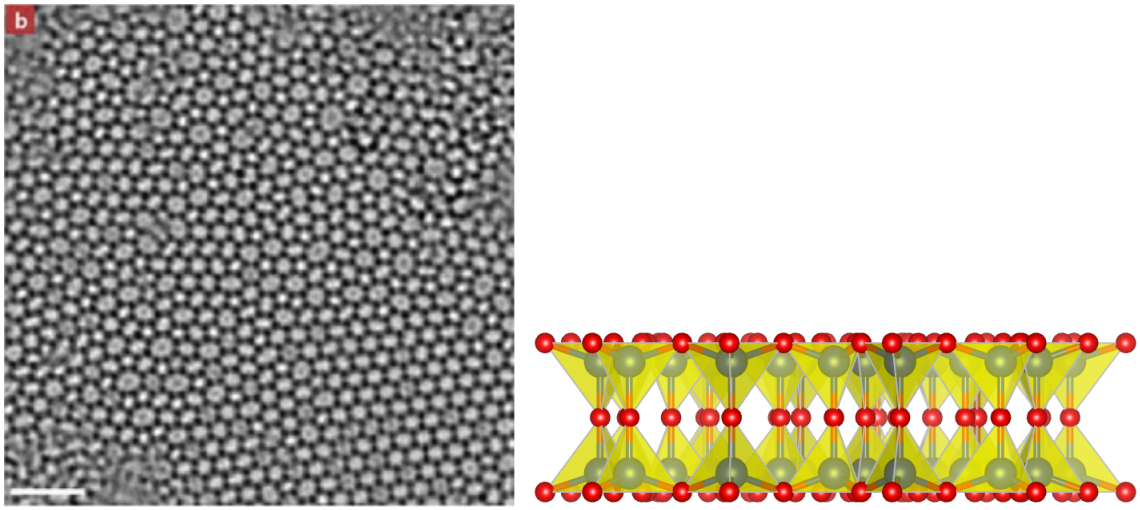

Figure 1.5: (Left) A TEM image of glassy region in the bilayer of silica supported on graphene reproduced from [4]. The scale bar is 2 nm. (Right) A side-view of silica bilayer model in which oxygen atoms (red) form a tetrahedral network while silicons (blue) are located at the center of tetrahedra.

the experimental data, later angle bending terms were added [27] (Fig. 1.4).

Computational tools have significantly improved our understanding of vitreous materials but the most exciting and promising path to grow our knowledge of such materials is imaging techniques that reveal the exact structure of an amorphous material independent of any model. The electron microscopy techniques can resolve the structure of crystals in 3D, but the structural determination of amorphous materials in 3D is still elusive despite the recent advancements [28]. One way to circumvent this limitation is to reduce the dimensionality from 3 to 2 which has led to the discovery and imaging of thin films of silica in both crystalline and noncrystalline forms. The thin films are in the form of the monolayer and bilayer of silica which are grown on graphene [4], on Ru(0001) [29, 8, 30] and Pd(100) [31] substrates and imaged using scanning probe microscopy (SPM) techniques. This advancement is not limited to silica as imaging of a monolayer of germania on a metal substrate is recently reported [14].

Although the bilayer structure extends in the $z-$direction, since it is the thinnest

stable form of silica, it is referred to as *2D glass*. The 2D glass consists of two layers of silica where each layer is a network of SiO_4 tetrahedron. The layers are connected through bridging oxygens and all atoms have perfect coordination (see Fig. 1.5) except those on the boundary. In addition, the ring structure of two layers are identical. Therefore topological and in-plane geometrical properties of silica bilayer are in fact present in 2D representation of the network; a two-dimensional network of corner-sharing triangles which oxygens are at the corners and silicons are at the center of triangles.

These microscopic images reveal the actual atomic arrangement of glass and open a new benchmark which models can be evaluated against. This offers a unique opportunity to not only revisit previous studies in the light of new findings but also to look into the realm that was previously impossible, already leading to new insights [32, 33, 34, 35]. In the following sections, a more detailed account of the structure of silica bilayers is given.

1.2 2D Amorphous Networks: Three Representations

Two-dimensional (2D) amorphous networks are used to model various materials from foams, and amorphous graphene (a-G) to silica bilayers (a-SiO_2). Such 2D networks have three representations which shed light on their different properties. The first one is a *cellular* representation. In this representation, the material is viewed as a packing of polygons in plane. The cellular patterns have long been the subject of studies in foams and grains [36], biological tissues [37], metallurgical aggregates, geographical structures, crack networks [38], ecological territories, Voronoi tessellations [39, 40] and even the universe at large scale [41] and fractals [42]. The broad range of materials and physical interactions is a remarkable property of cellular networks. In the bilayers of silica, this picture can be achieved by omitting the oxygen

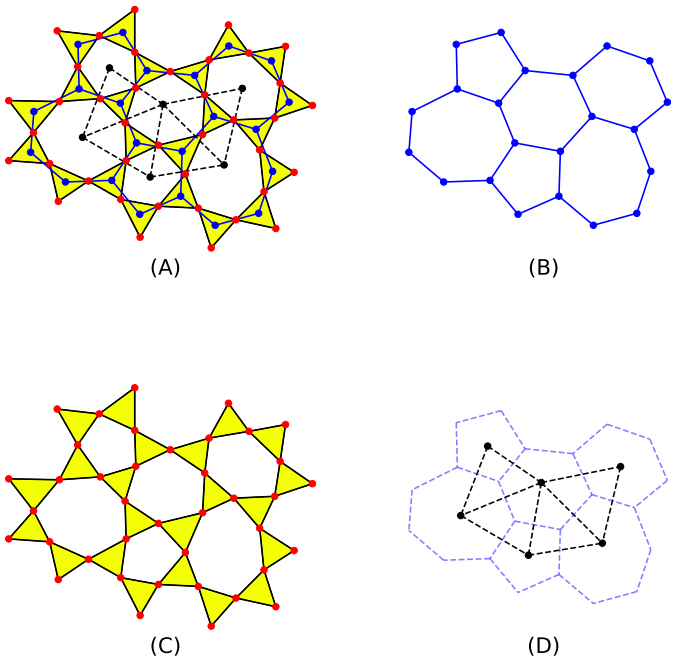

Figure 1.6: Three representations of a two-dimensional amorphous network. In reference to silica, the red and blue points are oxygen and silicon atoms, respectively. (A) An overlay of three representations and how they can be transformed to one another, (B) The cellular representation by emphasizing Si atoms, (C) The corner-sharing representation by connecting nearest-neighbors O atoms, and (D) Triangulation representation formed by the replacing polygons with their centroid. This representation is not the same as Delaunay triangulation.

atoms but emphasizing silicons (Fig. 1.6-B). In solid state physics literature, polygons or cells are often called rings. A ring is defined as a closed loop which obeys the shortest-path criterion [43]. Rings allow us to study order and correlations beyond short-range order which is focused on ordering on the scale of a bond length.

The rich history of studying ring structure in cellular patterns has uncovered a set of laws governing such structures which shows they are far from being random. Independent of the structural details and solely based on the topological considerations, Euler's theorem would apply to the cellular patterns :

$$N - N_B + N_R = \chi. \tag{1.6}$$

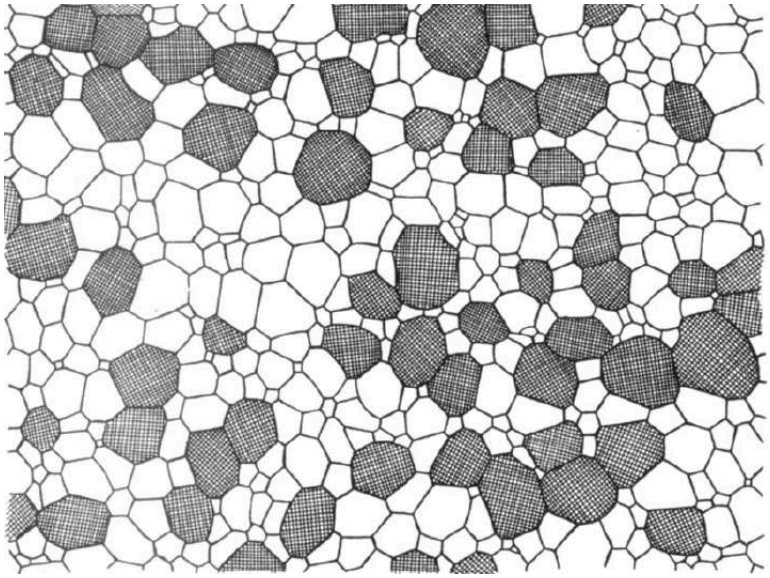

Figure 1.7: Polycrystalline magnesium oxide (MgO) reproduced from [5].

If N is the number of sites or vertices, N_B denotes the number of bonds or edges, N_R is the number of rings or cells, and χ is the topologically invariant Euler–Poincaré characteristic which its value depends on the embedding space but is a number of order 1([44], chapter 6).

Cellular patterns are almost universally made of trivalent sites meaning that each site is connected to three other sites. Since each site has three incident bonds and each bond is shared between two sites: $3N = 2N_B$. In addition, each bond is shared between two rings, so counting each ring would doubly count each bond. If we have N_n rings with $n-$sides, then $\sum_r N_n n = 2N_B$. We can finally find the mean ring size in trivalent cellular patterns using Eq. 1.6:

$$\langle n \rangle = \frac{\sum_n N_n n}{N_R} = 6(1 + \frac{3\chi}{N_B})^{-1}. \tag{1.7}$$

For graphs with topology of a torus as is the case for periodic boundary conditions, $\chi = 0$ and the mean ring size is exactly 6. For a planar graph, $\chi = 1$ and the mean ring size is slightly less than 6 but in the limit of a large system ($N \to \infty$), the mean ring size approaches 6.

Table 1.1: The fitting parameter in Aboav-Weaire law in various materials.

Material	α
Foam	0.2
Voronoi polygons	0.1
Silica bilayers (experiments)	0.33
Silica bilayers (computer models)	0.23

Although the global average ring size in cellular networks is fixed at 6 by topology, some local variations from this value are expected. Aboav observed that locally, *larger rings tend to be surrounded by smaller rings and vice versa*. Aboav's work on grain size distribution date back to 1965 [45] , but he is most famous for his 1970's paper on the arrangement of grains in polycrystals (Fig. 1.7) [5]. He found out that the average size of rings $m_1(n)$ around rings with n sides follows the following form:

$$m_1(n) = 5 + \frac{8}{n}. \tag{1.8}$$

The subscript 1 in $m_1(n)$ emphasizes that this is written for the nearest neighbors. Later, Weaire showed that this law cannot be general [46]. After several modifications, the above equation was written in the form of what is now called Aboav-Weaire law [21]:

$$nm_1(n) = 36 + \mu + 6(1 - \alpha)(n - 6) \tag{1.9}$$

where μ is the second moment of the ring distribution and α is a fitting parameter. The exact meaning of α is still debated [21]. The values of α for some materials are given in Table 1.1. The computer generated models of silica bilayers have a value of α close to the foams but smaller than that for experiments (microscopic images). This requires further investigation of ring correlations and modification of the bond-switching algorithm (see Figure 1.9).

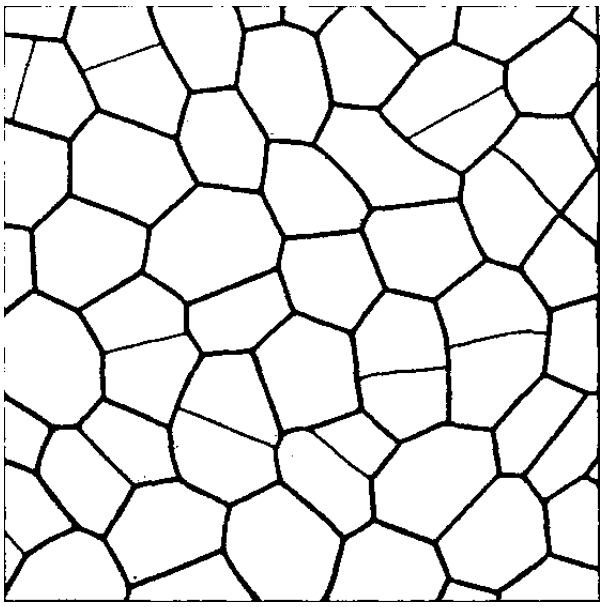

Figure 1.8: Cross section of cells in cucumber, reproduced from [6].

In fact, Lewis many years before Aboav had studied cellular networks in 1928 [6]. Lewis not only studied the cells of Cucumis (aka Cucumber!) but also compared the results to cooled wax and Giant's Causeway (Fig. 1.8). He confirmed that the mean ring size is indeed close to 6 and the ring distribution is dominated by the number of pentagons, hexagons and heptagons. But in particular, he found out that the area of a ring with n sides increases linearly with n (Lewis's law).

Both the Aboav-Weaire and the Lewis laws are observed and confirmed numerous times in cellular networks in a broad range of length scales governed by various interaction [39]. In fact, it has been shown that bilayers of silica also obey the Aboav-Weaire law. However, the Lewis law does not hold in 2D glasses. The reason is the remarkable symmetry of polygons in 2D glasses where they are very close to being regular, therefore the area law should be modified for such networks [47]. Chapter 2 employs this representation of 2D glasses and discusses the short- and medium-range order and generalizes Aboav-Weaire law to further neighbors.

Second representation of a 2D glass is a network of *corner-sharing triangles*. In

the case of a silica bilayer, such a network is formed by connecting nearest-neighbor oxygens while silicons are omitted (see Fig. 1.6-C). Mathematically, this is the "line graph" of a cellular network[3], where each edge is decorated by a new vertex. New vertices will be connected if their parent edges had a vertex in common. In this representation, each vertex (oxygen atom) is connected to four (six) vertex (atoms) in two (three) dimensions which makes the network locally isostatic, i.e. the degrees of freedom are balanced by the constraints. One application of such a representation is the structural refinement of the experimental samples of silica bilayer [9]. Microscopic images of silica naturally exhibit some uncertainty in atomic positions. In addition, experimental samples are finite and surface effects need to be removed to achieve high quality refinement. We can develop special boundary conditions to elevate both concerns which is the subject of Chapter 3. The goal is to add back enough constraints to the network to balance missing constrains on the surface. This is achieved by either freezing the motion of (some) surface atoms or limiting the motion along a direction [48].

In comparison to cellular networks, this representation is largely unexplored. However, its crystalline form is the Kagome lattice which is extensively studied in topics as diverse as antiferromagnetism [49], colloidal self-assembly [50] and optical lattices [51]. The most relevant studies are those concerned with elastic properties. For example, it is shown that geometrical distortion in the Kagome lattice controls its phonon structure and elastic properties [52]. To the best of our knowledge, the only example with topological disorder (apart from the studies in this thesis) is of the amorphous topological insulators [53].

The third case is a *triangulation representation* where *dual network* of a cellular network is constructed by placing a vertex at the centroid of each ring and connecting

[3]Also called "covering graph" or "the edge-to-vertex dual".

vertices that their rings share an edge (Fig. 1.6-D) to create a network of edge-sharing triangles. This is equivalent of triangulation of the plane and it can be shown that such a triangulation is approximately a Delaunay triangulation, provided that the polygons are not too distorted. The abundance of edges in this representation makes it a suitable choice for designer materials [54, 55, 56] since it allows full control over the structural properties by tuning its geometry and topology.

1.3 2D Amorphous Networks: Computational Considerations

As available experimental systems are small, computational tools can be used to create much larger systems to eliminate the finite size effects. Since the three discussed representations have widely different geometrical and topological properties, the algorithms to generate them are distinct but there is a transformation to convert one type to another.

Since cellular patterns are the most studied type of 2D amorphous networks, it is no surprise that they have the most well-established generating method. The method is essentially a 2D version of Wooten-Winer-Weaire (WWW) algorithm [57]. Starting from a perfect honeycomb lattice, a single bond-switching move will convert a cluster of four hexagons to a pair of pentagons and a pair of heptagons (Fig. 1.9). This transformation is also known as T1 move [39] or Stone-Wales defect [58]. By randomly and iteratively applying this transformation, a network of polygons varying in size is created. Each move is accepted through a Metropolis probability. Since this transformation alters the geometry of the network, the system is periodically relaxed using some potential such as the Keating potential [59] which would penalize the deviation from the ideal bond length and bond angle. It is worth noting that this is a zero-temperature algorithm but has been generalized to finite-temperature regime to account for thermal fluctuations of atoms [60]. To be complete, it is worth mentioning

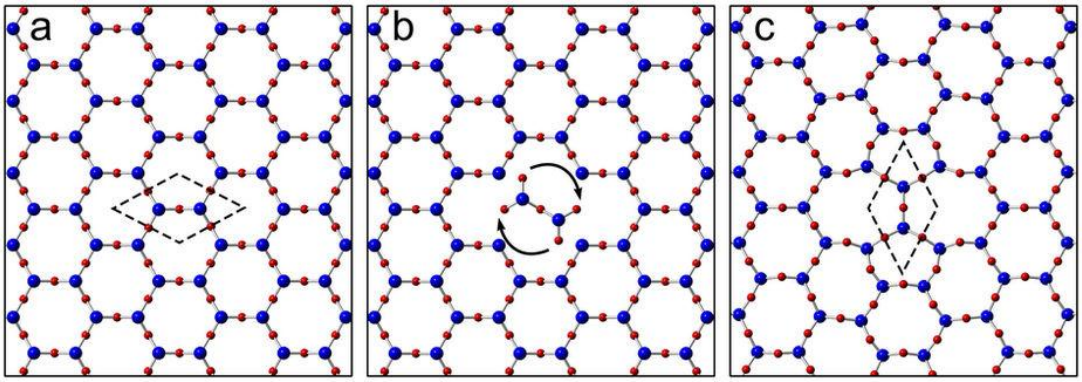

Figure 1.9: Transformation of honeycomb lattice (a) by a rotation of a structural unit to create a Stone-Wales defect (c). Reproduced from [7]

that corner-sharing representation [61] and edge-sharing representation [55] can be generated directly through other algorithms.

2D amorphous networks can be generated through Molecular Dynamics (MD) techniques, as well. A planar honeycomb lattice (*e.g.* pristine graphene) is melted and then the liquid is rapidly cooled down by different cooling rates. The energy minimization cycles are done through Tersoff-II potential [62]. Recently, A new two-body force field is presented based on Yukawa potentials [63].

All algorithms have good agreements with the available experimental data, but WWW algorithm has some advantages over MD methods. The WWW algorithm is successfully used to create networks with up to 10^5 atoms while the system size in MD simulations is of order of 10^3 atoms. The other advantage of WWW algorithm is that it maintains the perfect coordination throughout the simulations but in MD simulations, a small fraction of atoms are two- and four-coordinated (0.6% and 0.3% respectively) [64, 21].

1.4 From Monolayer to Bilayer

As it was discussed, a large part of structural information of a 2D glass is visible in its planar representation which is directly available through microscopic images. However, there is still some critical information hidden in the out-of-plane direction in order to have a complete picture of silica bilayers. In simulations, we can use the in-plane information to make the full three-dimensional structure of the bilayer. This is achieved in several steps. First, we raise Si atoms from the plane to complete the tetrahedra by adding an O for each Si, such that each Si atom is at the center of a tetrahedron. Then we form the mirror image of this monolayer. Finally two layers are connected via bridging oxygens to form the full bilayer as depicted in Fig. 1.5 (Right). Therefore, stoichiometry requirements are satisfied and all atoms gain their full coordination except those on the boundary.

An important piece of structural information of silica is encoded in the angle distribution. In particular, Si-O-Si angles are important since in-plane angles are projected on 2D and out-of-plane (bridging) angles are hidden in the microscopic images. When we joined the original monolayer and its mirror image, we implicitly assumed that these monolayers are connected at 180°, but in fact there is some evidence to the contrary. From studies of Si-O-Si angle in Cristobalite [65], it is shown that although 180° has a low-energy, it does not sit at the minimum energy and lower angles are preferred. The situation is more severe for Ge since the energy penalty is very steep for angles significantly deviated from $\sim 130°$. This might mean that synthesis of bilayers of germania is more difficult. However this assumption of a straight angle can be investigated in computational studies. Indeed, it turned out the Si-O-Si bridging angle is on average $\sim 175°$ and can be reproduced by variety of models including harmonic potential, polarizable-ion model molecular dynamics, and

density functional theory [9]. More surprisingly, the symmetry plane of the bilayer is maintained despite the tilt in the out-of-plane angles. This results on the structural refinement of silica bilayer are the subject of Chapter 4.

Chapter 2

RING CORRELATIONS IN RANDOM NETWORKS

This chapter is a reprint of the following journal article:

Sadjadi, Mahdi, and M. F. Thorpe. "Ring correlations in random networks." Physical Review E 94, no. 6 (2016): 062304.

My contributions to this work are the development of computer codes and mathematical formalism of the shell structure, generalization of the Aboav-Weaire law, creating the figures and writing the manuscript.

2.1 Abstract

We examine the correlations between rings in random network glasses in two dimensions as a function of their separation. Initially, we use the topological separation (measured by the number of intervening rings), but this leads to pseudo-long-range correlations due to a lack of topological charge neutrality in the shells surrounding a central ring. This effect is associated with the non-circular nature of the shells. It is, therefore, necessary to use the geometrical distance between ring centers. Hence we find a generalization of the Aboav-Weaire law out to larger distances, with the correlations between rings decaying away when two rings are more than about 3 rings apart.

2.2 Introduction

The structure of network glasses is often described by continuous random network (CRN) model. In this model, building units form a random network where short-

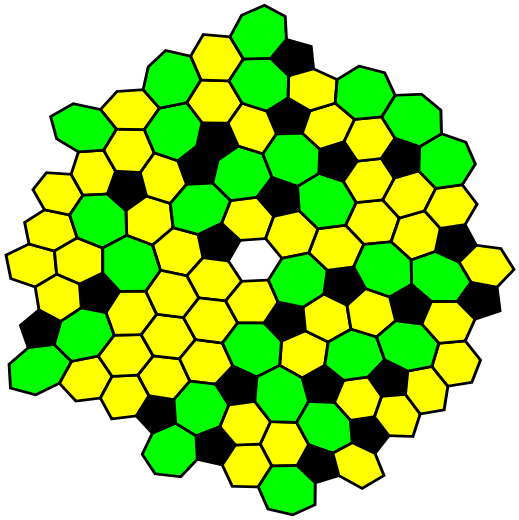

Figure 2.1: A piece of a two dimensional cellular network generated by bond-switching algorithm from a honeycomb lattice. Rings are colored based on their size. On the bottom left corner, a group of six-fold rings can be seen which also happens in experimental samples and is a feature of amorphous materials, due to statistical correlations. A central six fold ring has been left uncolored and shells of rings will be found around this. Any ring can be used as a central location.

range order is preserved similar to that in crystals but translational long-range order is absent due mainly to distorted bond angles [19, 18, 1]. Such structures have been generally studied by models [66] and diffraction experiments [2] which have provided invaluable information on short-range and medium-range order, mostly in the form of pair distribution functions (PDFs) [67, 68, 69, 70].

One challenge in using diffraction data is that this only provides average properties such that the structure cannot be reconstructed uniquely. Meanwhile, Scanning Probe Microscopy (SPM) and Electron Microscopy (EM) techniques have radically shortened the resolution limit and recently true atomic resolution images of silica bilayers and other two-dimensional (2D) amorphous surfaces have become available [8, 4]. However, high resolution imaging of bulk amorphous materials remains elusive [71]. These new results on 2D glasses have opened up numerous opportunities to study the structure of glasses using actual atomic coordinates. Recent work on 2D

glasses includes modeling of silica bilayers [72, 73], ring distribution [47], medium-range order [74], suitable boundary conditions to recover missing constraints in the surface [48] and the refinement of experimental samples [9]. Rigidity theory has also uncovered a connection between 2D glasses and jammed disk packings [75, 76].

The remarkable images of vitreous bilayer silica (SiO_2) unveil a ring structure which is the characteristic of covalent glasses. But similar underlying structure also can be found in various amorphous materials such as amorphous graphene [77, 64, 78]. In fact, these atomic materials are members of a larger class of materials (many with larger length scales) collectively known as *cellular networks*. Examples are foams and grains [36], biological tissues [37], metallurgical aggregates, geographical structures, crack networks [38], ecological territories, Voronoi tessellations [39, 40] and even the universe at large scale [41] and fractals [42]. Given the wide range of length scales, formation mechanisms and physical properties, cellular networks have been the subject of many studies [79, 80]. Despite the topological resemblance between 2D amorphous systems and other cellular networks, one should note that these materials are microscopic systems with a very different nature of bonds and forces and hence they can shed light on new properties of cellular networks, in particular those related to geometry.

These glassy networks are almost entirely $3-$coordinated networks, i.e., each vertex is connected to three other vertices through edges which form the boundary of polygonal rings (Fig. 2.1). In the case of amorphous graphene - vertices represent carbon atoms. In silica bilayer, rings are formed by connecting silicon atoms while intervening oxygen atoms are omitted.

These glassy networks, to some extent, are random and their study requires a statistical approach but experimental samples of amorphous materials are relatively small [81]. Additionally, the small size of many samples does not permit the study

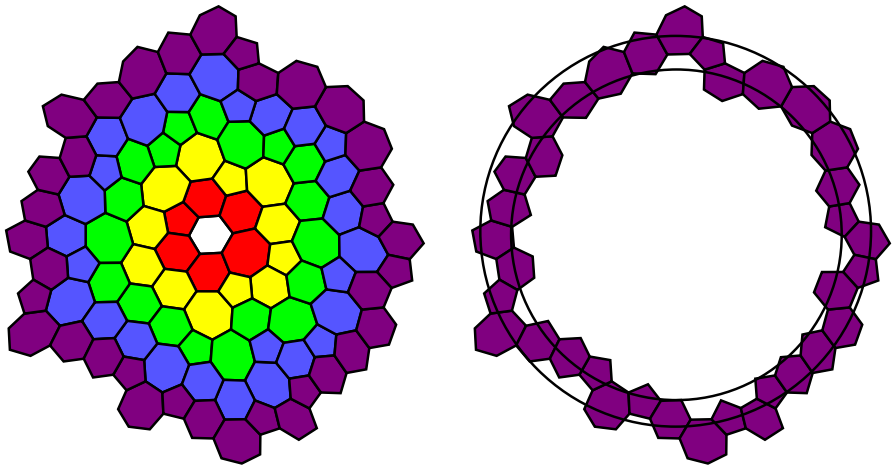

Figure 2.2: (a): Partitioning of the random network in Fig. 2.1 into topological shells. The shells grow roughly in circular shapes. This piece also has a triplet inclusion in the forth (blue) shell where a 5-ring is isolated from the fifth (purple) shell. (b) Although shells are roughly circular, no circle can sweep all rings within a single shell; hence ring distributions with topological and geometrical definitions are different.

of ring correlations at larger distances with good statistics. In this work, we employ large computer models to study correlations among the rings. In the literature, the focus has been on the correlation among adjacent rings where well-known Aboav-Weaire's law captures the tendency of smaller and larger rings to be adjacent. This paper studies various correlation functions out to large topological and geometrical distances and generalizes the Aboav-Weaire's law.

2.3 Shell Analysis and Correlations

We define an $n-$ring as a ring with n adjacent rings. The ring distribution of a network with a total of N rings is characterized by $p(n)$, the fraction of $n-$rings, its mean $\langle n\rangle = \sum_n np(n)$, and the second moment about the center $\mu = \langle n^2\rangle - \langle n\rangle^2$. According to Euler's theorem, the mean ring size for a network with periodic bound-

ary conditions (PBCs) is exactly $\langle n \rangle = 6$ [1]. The ensemble average of a quantity x is defined as $\langle x \rangle = \sum_n p(n)x$. To overcome the finite size effect in the experimental samples, we use computer-generated models under PBCs with ∼100000 vertices (∼50000 rings) generated from an initially honeycomb lattice using bond-switching algorithm. Here, a bond between two nearest neighbor sites is selected and replaced by a dual bond at right angle and local topology is reconstructed to maintain the three-fold coordination everywhere [57, 58]. Although, experimental samples contain rings with size 4 to 9, but fraction of rings with sizes other than 5 to 7 are statistically quite rare [47]. We studied two networks one with only 5 to 7 rings and one with 5 to 8 but no essential difference was observed. Therefore we report results of the network with 5 to 8−fold rings with the following ring distribution: $p(5) = 0.262$, $p(6) = 0.494$, $p(7) = 0.227$, $p(8) = 0.0172$ and $\mu = 0.558$. Nevertheless, the measures of this paper are general and can be applied to all glassy and cellular networks.

The correlation among rings is usually defined over a *topological distance* t. The topological distance between two rings is defined as the minimum number of bonds should be traversed to connect two rings. This distance is the equivalent of distance of two nodes in the dual graph (when each ring is represented by a node) of Fig. 2.1. The distance of a ring from itself is zero ($t = 0$). All rings which have one common side with a given central ring are located at $t = 1$ (first shell). Adjacent rings to the first shell, excluding the central ring, are at $t = 2$ (second shell). This process can be continued to find shells at any topological distance similar to Fig. 2.2. A ring at shell t is adjacent to at least one ring at shell $t-1$ and usually adjacent to at least one ring

[1] The mean ring size in the finite experimental samples is slightly less than 6 since the surface sites are under-coordinated. Although for sufficiently large systems, boundary effects are negligible. Note that the outer perimeter is also a ring and should be counted in Euler's theorem but our definition of ring only considers shortest paths.

in shell $t+1$, otherwise this ring is trapped and forms a *triplet inclusion* (Fig. 2.2). This definition naturally divides/partitions the network into concentric shells around any given ring. Therefore, all properties of the network are studied as a function of the topological distance and the size of the central ring [82, 83], as first pointed out by Aste et al [84, 85].

A shell at distance t from an $n-$ring is characterized by three numbers: number of n'-rings $N_t(n,n')$; total number of rings (shell size) $K_t(n)$, and total number of sides (edges) $M_t(n)$. These quantities are related as follows:

$$K_t(n) = \sum_{n'} N_t(n,n'), \tag{2.1}$$

$$M_t(n) = \sum_{n'} n' N_t(n,n'). \tag{2.2}$$

Since these equations are linear, they are also valid for the averaged values over all $n-$rings. More importantly, note that $N_t(n,n')$ is not symmetric in respect to n and n'. This reflects the fact that local order of the rings is strongly dependent on the size of the central ring. Specially, $N_t(n,n')$ should not be confused by the number of $n-n'$ pairs at topological distance t:

$$Np(n)N_t(n,n') = Np(n')N_t(n',n), \tag{2.3}$$

which by definition is symmetric. This symmetry can relate the ensemble average of the number of sides (Eq. 2.2) to the ensemble average of shell size (Eq. 2.1) at any topological distance:

$$\begin{aligned}\langle M_t \rangle &= \sum_n p(n) M_t(n) = \sum_n \sum_{n'} p(n) n' N_t(n,n') \\ &= \sum_{n'} n' p(n') K_t(n') = \langle n K_t \rangle \,. \end{aligned} \tag{2.4}$$

This relation is the generalized Weaire sum rule which was originally proposed for the first shell where it takes the form $\langle M_1 \rangle = \langle n^2 \rangle = \langle n \rangle^2 + \mu$ [46, 86]. Note that the

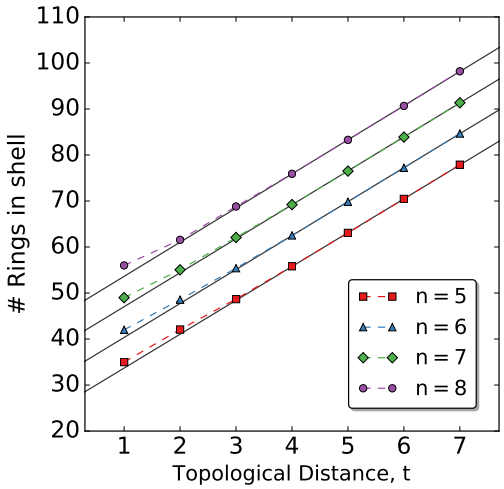

Figure 2.3: Dependence of the number of rings $K_t(n)$ on topological distance t and size of the central ring n. $K_t(n)$ grows linearly for $t \geq 4$. Solid lines are fitted lines to the last three points. Points are offset for clarity with $6n$.

first shell is the only shell for which K is exactly determined $[K_1(n) = n]$ but Eq. 2.4 surprisingly encapsulates all the statistical variation in the local ring distribution in a simple form.

The space-filling nature of rings in the network requires that $K_t(n)$ scales linearly with t in the absence of correlation. This means that the growth rate of the shell size is a constant number independent of the size of the central ring. Although, geometrical constraints on the polygonal tiling of the plane does not allow a complete independence from the central ring simply because shell closure around a larger ring requires more rings. As a result, the intercept of $K_t(n)$ remains a function of n. Therefore we expect that:

$$K_t(n) = At + B(n), \tag{2.5}$$

for $t \geq \xi$, where ξ is the ring correlation length. In a hexagonal lattice, the growth rate A is 6 but as Fig. 2.2 shows, in a random network, shells grow roughly in circular form and simple geometrical arguments predict that the growth rate should be 2π. However, because rings meet each other at random orientations and the shell

surface is rough, the actual growth rate is usually greater than 2π and A can be a measure of this roughness [87]. Figure 2.3 shows the number of the rings in the shells around different central rings. The linear behavior of the shell size is observed in various systems and is present in 2D glass, as expected. However, in 2D glasses $A = 7.31 \pm 0.1$ which is much smaller compared to the reported values for Voronoi tessellation (11.0 ± 0.2) and soap (9.45 ± 0.1) [84], probably due to the bond bending interactions which result in the high symmetry (close to the maximum area for given edge lengths) of the rings in the 2D glass [47].

Another useful quantity is the topological charge of an n-ring defined as $6 - n$ (also called "disclination"). Since the mean ring size in the network is 6, equivalently total charge of the network is zero. However a piece of the network can contain any amount of charge depending on the local ring distribution. Hence, topological charge is a useful quantity that monitors the local deviation from the bulk properties. In particular, the topological charge of a shell $q_t(n)$ can be defined as the sum of the charge of its rings:

$$q_t(n) = \sum_{n'} (\langle n \rangle - n') N_t(n, n') = \langle n \rangle \, K_t(n) - M_t(n). \tag{2.6}$$

From short- and medium-range order, it is expected that rings around a given ring are distributed such that the charge of the central ring is screened by the charge of the neighboring shells and for $t > \xi$, the ring distribution is similar to the bulk (charge per shell is zero). But as Eq. 2.5 shows, the shell size is a function of n for any distance and therefore rings are counted with different weights in calculating the charge per shell. In fact, Eqs. 2.4, 2.5 and 2.6 readily yield an asymptotic value for the shell charge for $t > \xi$:

$$\langle q_t \rangle = \langle (\langle n \rangle - n) K_t \rangle \approx p(5)B(5) - p(7)B(7), \tag{2.7}$$

which is exact for a network with $n = 5, 6, 7$ and approximately correct as long

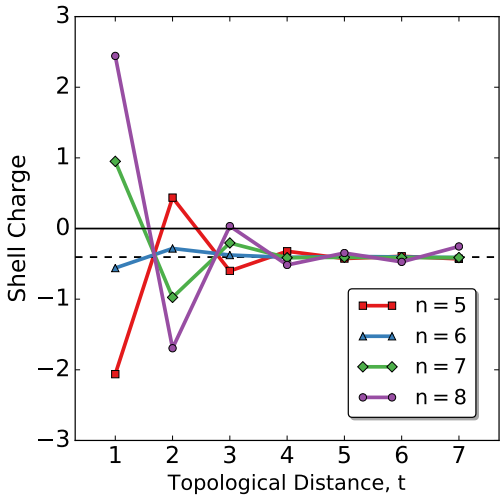

Figure 2.4: Shell charge $q_t(n)$ vs. topological distance t. The shell charge settles to a constant non-zero number for $t \geq 4$. The dashed line shows the asymptotic offset -0.4.

as fraction of the other rings is negligible. Therefore $\langle nK_t \rangle$ does not factorize and statistically, there is a tendency to have larger rings in a shell [$\langle q_t \rangle < 0$ since $B(7) > B(5)$] .

The results of calculating the charge per shell is shown in Fig. 2.4. For $t = 1$, the total shell charge has an opposite sign to the charge of the central ring to screen the charge but for $t > 1$ screening does not happen and the charge per shell reaches a non-zero constant value, conjectured in Eq. 2.7. It is interesting to note that although the charge of 5- and 7-rings have the same magnitude, the strength of screening for these two is considerably different in the first shell. This shows that geometry has a strong effect on the ring distribution. Note that hexagons have short-range correlations ($\xi = 1$) but other rings are correlated up to $\xi = 3$ (medium-range correlation) with different strengths.

Topological charge gives a rather complete picture of correlations in the shell structure, but the most studied measure of correlations in the literature is the mean ring size in the first shell around a central ring, through the well-known Aboav-Weaire

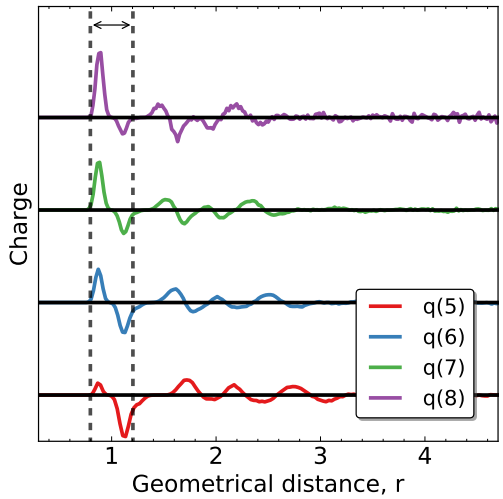

Figure 2.5: The topological charge $q_r(n)$ per shell is plotted against the geometrical distance r. The shell charge approaches zero for distances about three rings away. This figure should be compared to Fig. 2.4. The two dashed lines represent the geometrical distance corresponding to the minimum and maximum values for the first shell with $t = 1$. Curves are offset for clarity where horizontal solid lines show the expected asymptotic values of zero.

law that a ring with large size tends to have smaller rings in its neighborhood and vice versa [88, 89]. Mathematically, the mean ring size $m_1(n)$ around a ring with n neighbors can be written (to a very good approximation) as [5, 46]:

$$nm_1(n) = \langle n \rangle^2 + \mu + \langle n \rangle (1 - \alpha)(n - \langle n \rangle), \tag{2.8}$$

where α is a fitting parameter which depends on the specific network. Usually a network is characterized by (μ, α). The meaning of α is not clear but it has been argued that it is a metrical quantity [90] or the average excess curvature [89] but these definitions only work in special cases. In our network, $\alpha \approx 0.23$ which is somewhat smaller than values extracted from experiments [47] showing computer generated models still need further refinement.

We would like to extend Aboav-Weaire law to longer distances to study correlation of a ring with the shells around it. The above form can be used to propose a

generalized Aboav-Weaire law as:

$$nm_t(n) = \langle n \rangle^2 + \mu_t + \langle n \rangle (1 - \alpha_t)(n - \langle n \rangle), \tag{2.9}$$

where for $t = 1$ we recover Eq. 2.8 with $\mu_1 = \mu$. A similar argument presented to derive Eq. 2.7 can be used to find an asymptotic value for $m_t(n)$. At sufficiently long distances, the ring distribution in the shells is independent of the size of the central ring and $\langle M_t \rangle \approx \langle m_t K_t \rangle = \langle m_t \rangle \langle K_t \rangle$, therefore for $t > \xi$:

$$\langle m_t \rangle = \frac{\langle M_t \rangle}{\langle K_t \rangle} = \frac{\langle nK_t \rangle}{\langle K_t \rangle} = 6 - \frac{\langle q_\infty \rangle}{\langle K_t \rangle}. \tag{2.10}$$

While we expect $\alpha_\infty = 0$ but we showed, $\langle q_\infty \rangle < 0$, so the asymptotic value of $m_\infty(n)$ is larger than the bulk value 6. For this reason, $m_t(n)$ approaches 6 as t^{-1} (since $K_t(n) \sim t$) which is sometimes interpreted as a long-range correlation [91, 92]. However this should be regarded as an artifact because the shells are defined in such a way (topologically) which results(unfortunately) in the topological charge never going to zero, even at very large distances, and in fact approaching a constant as shown here. This is due to the non-circular nature of the shells, and can be avoided if the shells are chosen in such a way as to make them more nearly circular. Unfortunately this is not possible with a purely topological definition, and so we are forced to adopt a *geometrical definition* for the ring-shell correlations.

Figure 2.2 shows the difference between topological and geometrical distance. Despite the fact that shells found by topological distance are roughly circular, it is not possible to find a single circle which contains all the rings in the shell, therefore ring distributions etc. are different in the two cases.

The *geometrical* distance r between two rings is defined as the Euclidean distance between their centroids. Therefore, instead of using the discrete integer distance t,

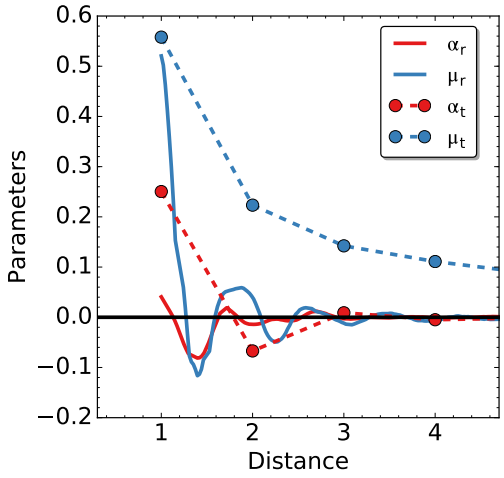

Figure 2.6: Plot of two coefficients in the generalized Aboav-Weaire law, α_r and μ_r with their topological counterparts, α_t and μ_t. Geometrical definitions show that correlation quickly decays to zero while pseudo-correlations in the topological case last over a long-range for μ_t. The geometrical distances are chosen so the geometrical and topological distances agree for the first shell.

the quantities q and m are written as a function of a continuous distance r:

$$q_r(n) = 6K_r(n) - M_r(n), \tag{2.11}$$

$$nm_r(n) = \langle n \rangle^2 + \mu_r + \langle n \rangle (1 - \alpha_r)(n - \langle n \rangle). \tag{2.12}$$

Since r is continuous, a binning procedure is used to compare with the previous results using topological distance. Small bins are used with a windowing procedure where the width of the window mimics unity in topological distance. Results for the charge are shown in Fig. 2.5. It is evident that correlations last about 3 shells and are quite short-ranged with the charge going to 0 over the same range, as expected. Therefore this definition of a shell using geometrical distance is more useful. Because of the different size of the rings, e.g., distance between a $5-6$ pair is greater than a $7-8$ pair so a range of geometrical distances corresponds to a single topological distance. To compare the two distances, we rescale the geometrical distance by the average distance between adjacent rings, which is defined to be unity. Fig. 2.5 shows

this for the first neighbors with two dashed lines. Within this window, all four curves show a common trend: a maximum followed by a minimum. The former corresponds to 5−rings (positively charge) and the latter to 7− and 8−rings (negatively charged). The point in the middle corresponds to neutral 6−rings. The horizontal axis is normalized such that these three points line up for all curves. According to Aboav-Weaire law, smaller rings surround a larger ring; the pronounced minimum of $q_r(5)$ due to 7− and 8−rings and the pronounced maximum of $q_r(7)$ and $q_r(8)$ due to 5−rings admit this law. In the case of $q_r(6)$, minimum and maximum have the same amplitude due to uniform distribution of the rings around hexagons hence their weak correlations with other rings.

It is also constructive to look at the Aboav-Weaire law using geometrical distance. In this case, we expect that both α_r and μ_r decay rapidly to zero in accordance with the absence of correlations for large r. This is confirmed in Fig. 2.6 which clearly for distances larger than 3, the mean ring size is essentially exactly 6. This confirms our assertion that ring correlations in glassy networks are either short-range or medium-range and using geometrical distance in the calculations of topological charge and mean ring size resolves the issue of excess topological charge in the shells found by topological distance which is shown by the long-tail of μ_2 in Fig. 2.6.

Fig. 2.7 shows linearity of the generalized Aboav-Weaire law for the third neighbors. The plot shows that $nm(n)$ is indeed a linear function of n but because of pseudo-correlations, the average ring size using topological distance is slightly larger than expected for geometrical distance, where the mean ring size is 6 for three-fold coordinated networks.

Although the topological charge and Aboav-Weaire law are useful tools to quantify correlations, they only measure correlations between a ring and shells. The ring-ring correlation function is perhaps a better measure of correlations especially since, as

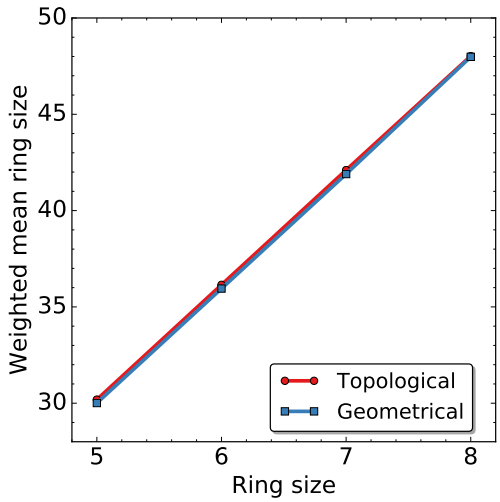

Figure 2.7: Plot of weighted mean ring size $nm(n)$ versus ring size n for the third neighbors using both geometrical and topological distance. This plot shows that the mean ring size for all shells follows the generalized Aboav-Weaire law (Eq. 2.9). Note that the topological definition leads to a slightly larger mean ring size.

it was shown, definition of shells using the topological distance do introduce some artifacts such as excess charge.

To find out the correlation between two single rings, we need to derive an expression for the probability $p_t(n, n')$ of finding a pair of n, n' rings with distance t. For a given $n-$ring, the number of $n'-$rings at distance t is $N_t(n, n')$ while on average a typical shell has $\langle K_t \rangle$ rings. Therefore the probability of having a pair of rings is [93]:

$$p_t(n, n') = \frac{p(n) N_t(n, n')}{\langle K_t \rangle}. \tag{2.13}$$

This equation is important as it relates ring distributions of the shell structure to of the network (For $t = 1$, this equation reduces to the correlation function defined in Ref. [94]). If the rings were independent, this probability is simply product of the individual probabilities but we showed the ring distribution of a shell is different from the bulk and rings are topologically dependent even for large t. This motivates us to define the probability of having an $n-$ring at shell t (independent of the central ring)

as:

$$p_t(n) = \sum_{n'} p_t(n', n) = p(n)\frac{K_t(n)}{\langle K_t \rangle}, \tag{2.14}$$

which can be derived using Eqs. 2.1 and 2.3. The probability of having $n-$ring is proportional to the average shell size around $n-$fold rings and the ensemble averaged shell size. We define correlation function between two n and n' sided rings as:

$$C_t(n, n') = p_t(n, n') - p_t(n)p_t(n') \tag{2.15}$$

Figure 2.8 shows the results for the above correlation function. This clearly shows the medium-range order of the rings except for hexagons where correlations are weak and short-range. In contrast with the results in Ref. [93], hexagon-hexagon is short-range and only non-zero for adjacent cells ($t = 1$) which is a signature of microcrystal regions in the network (see Fig. 2.1). If we had used $p(n)p(n')$ instead of $p_t(n)p_t(n')$, ring-ring correlation shows a long-range behavior due to topological effect [95, 96] but Eq. 2.14 correctly captures the nature of correlations in the random network.

2.4 Discussion and Conclusion

We have shown that correlations between rings in glassy networks can be treated best if geometrical rather than topological distances between rings are used. Using topological distances, which would be preferable, unfortunately leads to spurious long range correlations as the topological charge for each shell around a central ring does not approach zero at large distances, due to the non-circular nature of the shells. These issues are absent if the geometrical distances between the centers of rings are used. We find in this case that correlations only extend out to about third neighbor rings, and can be described by a generalized Aboav-Weaire law. These studies have been done on a very large computer-generated network with periodic boundary conditions [57, 58]. Experimental samples of bilayer of vitreous silica are

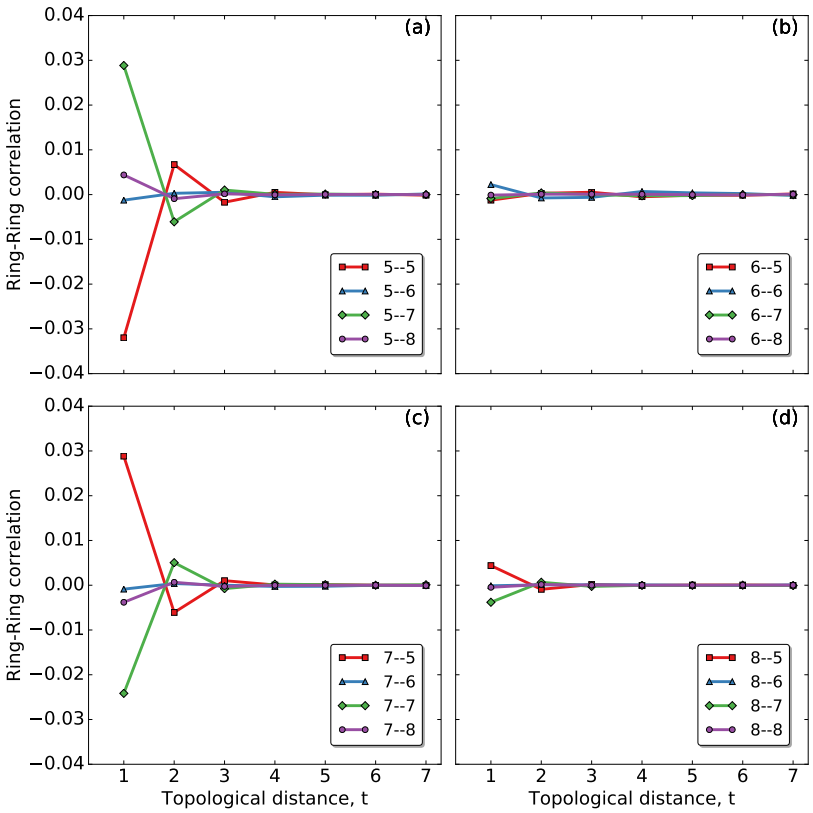

Figure 2.8: Ring-ring correlation $C_t(n, n')$ versus topological distance t. The correlations are short or medium range depending on the size of the interacting rings. Although hexagons are weakly correlated with their neighbor rings, other rings show a high degree of correlations up to three rings away. Very similar results are obtained using geometrical distances. Note that correlations are symmetric so that $5-6$ is the same as $6-5$ etc. where panel (a) is for five-fold rings, panel (b) six-fold rings, panel (c) seven-fold rings, and panel (d) eight-fold rings.

currently too small to allow for the study of longer range correlations, but the main conclusion of the paper that geometrical rather than topological distances should be used is expected to hold. Future studies comparing experimental and computer-generated networks (both three-coordinated with similar ring distributions) should help explain why different values of α are obtained in these two cases [47].

We should thank Avishek Kumar for providing the computer-generated networks, and David Sherrington and Mark Wilson for useful ongoing discussions. MS was partially supported by the Arizona State University Graduate and Professional Student

Association's JumpStart Grant Program. MS was aided in this work by the training and other support offered by the Software Carpentry project. Support through NSF grant # DMS 1564468 is gratefully acknowledged.

Chapter 3

ANCHORED BOUNDARY CONDITIONS FOR LOCALLY ISOSTATIC NETWORKS

This chapter is a reprint of the following journal article:

> Theran, Louis, Anthony Nixon, Elissa Ross, Mahdi Sadjadi, Brigitte Servatius, and Michael F. Thorpe. "Anchored boundary conditions for locally isostatic networks." Physical Review E 92, no. 5 (2015): 053306.

My contributions to this work are the preparation of the network of corner-sharing triangles, designing and construction of figures and captions, developing codes for implementation of sliding and anchored boundary conditions, and writing the manuscript.

3.1 Abstract

Finite pieces of locally isostatic networks have a large number of floppy modes because of missing constraints at the surface. Here we show that by imposing suitable boundary conditions at the surface, the network can be rendered *effectively isostatic*. We refer to these as *anchored boundary conditions*. An important example is formed by a two-dimensional network of corner sharing triangles, which is the focus of this paper. Another way of rendering such networks isostatic, is by adding an external wire along which all unpinned vertices can slide (*sliding boundary conditions*). This approach also allows for the incorporation of boundaries associated with internal *holes* and complex sample geometries, which are illustrated with examples. The recent synthesis of bilayers of vitreous silica has provided impetus for this work.

Experimental results from the imaging of finite pieces at the atomic level needs such boundary conditions, if the observed structure is to be computer-refined so that the interior atoms have the perception of being in an infinite isostatic environment.

3.2 Introduction

Boundary conditions are paramount in many areas of computer modeling in science. At the atomic level, finite samples require appropriate boundary conditions in order that atoms in the interior behave as if they were part of a larger or infinite sample, or as closely to this as is possible. One example of this is the calculation of the electronic properties of covalent materials where the surface is terminated with H atoms so that all the chemical valency is satisfied. In this way the HOMO (highest occupied molecular orbital) and the LUMO (lowest unoccupied molecular orbital) states inside the sample can be obtained that are not very different from those expected in the bulk sample. In materials science the electronic band structure of a sample of crystalline Si could be obtained by determining the electronic properties of a finite cluster terminated with H bonds at the surface. In practice this is rarely done, as it is more convenient to use periodic boundary conditions and hence use Bloch's theorem, but this technique has been used recently in graphene nanoribbons [97].

For most samples, the nature of the boundary, fixed, free or periodic only alters the properties of the sample by the ratio of the number of atoms on the surface to those in the bulk. This ratio is $N^{-1/d}$ where N is the number of atoms (*later referred to as vertices*) and d is the dimension. Of course this ratio goes to zero in the thermodynamic limit as the size of the system $N \to \infty$ and leads to the important result that properties become independent of boundary conditions for large enough systems.

Similar statements can be made about the mechanical and vibrational properties of

systems *except* for isostatic networks that lie on the border of mechanical instability. In this case the boundary conditions are important no matter how large N, and special care must be taken with devising boundary conditions so that the interior atoms behave as if they were part of an infinite sample, in as much as this is possible [98, 99, 76].

In Figure 3.1, we show a part of a Scanning Probe Microscope (SPM) image [8] of a bilayer of vitreous silica which has the chemical formula SiO_2. The sample consists of an upper layer of tetrahedra with all the apexes pointing downwards where they join a mirror image in the lower layer. In the figure we show the triangular faces of the upper tetrahedra, which form rigid triangles with a (red) Si atom at the center and the (black) O atoms at the vertices of the triangles which are freely jointed to a good approximation. We refer to these networks as *locally isostatic* as the number of degrees of freedom of the equilateral triangle in two dimensions is exactly balanced by the shared pinning constraints (2 at each of the 3 vertices, so that $3-2\times 3/2=0$). While the 3D bilayers are locally isostatic, so too are the 2D projections of corner-sharing triangles which are the focus of this paper. We will use the *Berlin A* sample as the example throughout [72, 47] so that we can focus on this single geometry for pedagogical purposes.

Because experimental samples are always finite in extent and usually have irregular boundaries, including internal regions that are either absent, or not imaged it is necessary to develop appropriate boundary conditions. Note that the option of cutting a rectangular piece out of the experimental image is not available because of the amorphous nature of the network, which means that it is not possible for the left side to connect to the right side as with a regular crystalline network. Even if this were possible, it would be unwise to discard experimental data and hence lose information. In this paper we show how boundary conditions can be applied to locally isostatic

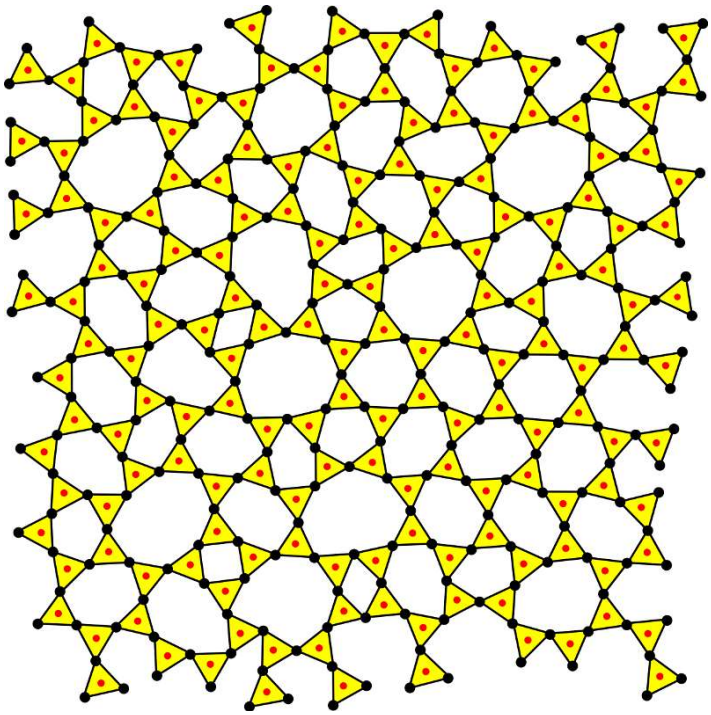

Figure 3.1: Showing a piece of bilayer of vitreous silica imaged in SPM (Scanning Probe Microscope) [8] to show the Si atoms as red discs and the O atoms as black discs. The local covalent bonding leads to the yellow almost-equilateral triangles that are freely jointed, which we will refer to as *pinned*. The triangles at the surface have either one or two vertices unpinned.

systems which are not periodic.

In this paper, we show rigorously that there are various ways to add back the exact number of missing constraints at the surface, in a way that they are sufficiently uniformly distributed around the boundary that the network is guaranteed to be isostatic everywhere. There is some limited freedom in the precise way these boundary conditions are implemented, and the boundary can be general enough to include internal holes. The proof techniques used here involve showing that *all* subgraphs have insufficient edge density for redundancy to occur [100]. In the appendix, we give an algorithmic description of our boundary conditions and discuss in detail how to ensure the resulting boundary is sufficiently generic.

Using the pebble game [101, 102], we verified on a number of samples that anchored

boundary conditions in which alternating free vertices are pinned results in a global isostatic state. The pebble game is an integer algorithm, based on Laman's theorem [100], which for a particular network performs a rigid region decomposition, which involves finding the rigid regions, the hinges between them, and the number of floppy (zero-frequency) modes. We have used it to confirm that the locally isostatic samples such as that in this paper are isostatic overall with anchored boundary conditions. The results of this paper imply that, under a relatively mild connectivity hypothesis, this procedure is provably correct, and thus, relatively robust. Additionally, the necessity of running the pebble game for each individual case is avoided.

Figure 3.2 shows *sliding* boundary condition [103]. These make use of a different, simpler kind of geometric constraint at each unpinned surface site. The global effect on the network's degrees of freedom is like that of the anchored boundary conditions, and this setup is computationally reasonable. At the same time, the proofs for this case are simpler, and generalize more easily to handle situations such as holes in the sample.

In Figure 3.3, we show the anchored boundary conditions. We have trimmed off the surface triangles in Figure 3.1 that are only pinned at one vertex. This makes for a a more compact structure whose properties are more likely to mimic those of a larger sample, and makes our mathematical statements easier to formulate. In addition we have had to remove the 3 purple triangles at the lower right hand side in order to get an even number of unpinned surface sites. When the network is embedded in the plane, this is possible, except for very degenerate samples (see Figure 3.3).

3.3 Combinatorial Anchoring

Intuitively, the internal degrees of freedom of systems like the ones in Figures 3.1 and 3.3 correspond to the corners of trianges that are not shared. This is, in essence,

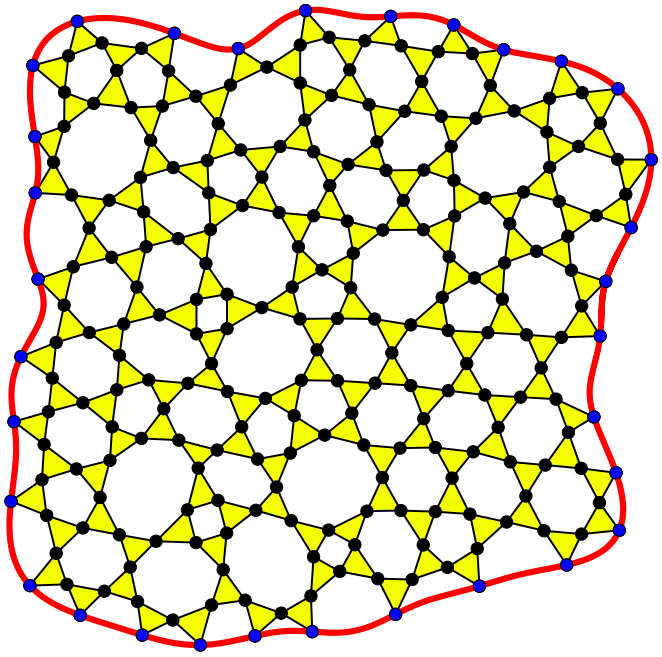

Figure 3.2: Illustrating sliding boundary conditions, used for a piece of the sample shown in Figure 3.1. The boundary sites are shown as blue discs and the 3 purple triangles at the lower right Figure 3.3 have been removed. The red Si atoms at the centers of the triangles in Figure 3.1 have also been removed for clarity. The boundary is formed as a smooth analytic curve by using a Fourier series with 16 sine and 16 cosines terms to match the number of surface vertices, where the center for the radius $r(\theta)$ is placed at the centroid of the 32 boundary vertices [9]. Note that sliding boundary conditions do not require an even number of boundary sites.

the content of Lemma 1 proved below. Proving Lemma 1 requires ruling out the appearance of *additional* degrees of freedom that could arise from *sub-structures* that contain more constraints than degrees of freedom.

The essential idea behind combinatorial rigidity [1] is that *generically* all geometric constraints are visible from the topology of the structure, as typified by Laman's [100] striking result showing the sufficiency of Maxwell counting [105] in dimension 2. Genericity means, roughly, that there is no special geometry present; in particular, generic instances of any topology are dense in the set of all instances.

[1] See, e.g., the monograph by Graver, et al. [104] for an introduction.

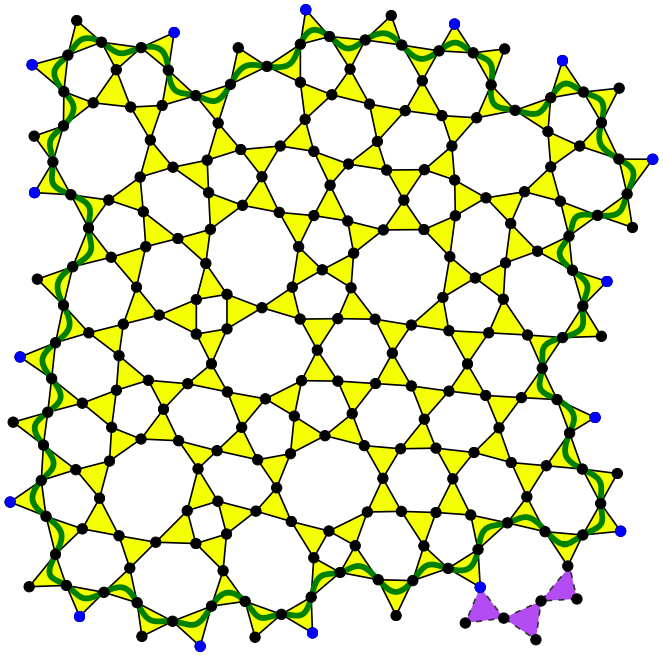

Figure 3.3: Illustrating the anchored boundary conditions used for the sample shown in Figure 3.1. The alternating anchored sites on the boundary are shown as blue discs and the 3 purple triangles at the lower right are removed to give an even number of unpinned surface sites. The red Si atoms at the centers of the triangles in Figure 3.1 have been suppressed for clarity.

In what follows, *we will be assuming genericity*, and then use results similar to Laman's, in that they are based on an appropriate variation of Maxwell counting. Our proofs have a graph-theoretic flavor, which relate certain hypotheses about connectivity [2] to hereditary Maxwell-type counts.

3.3.1 Triangle ring networks

We will model the flexibility in the upper layer of vitrious silica bilayers as systems of 2D triangles, pinned togehter at the corners. The joints at the corners are allowed to rotate freely. A triangle ring network is *rigid* if the only available motions preserving triangle shapes and the network's connectivity are rigid body motions; it is *isostatic*

[2] To make this paper somewhat self-contained, we will briefly explain the concepts we use. Our terminology is standard, and can be found in, e.g., the textbook by Bondy and Murty [106].

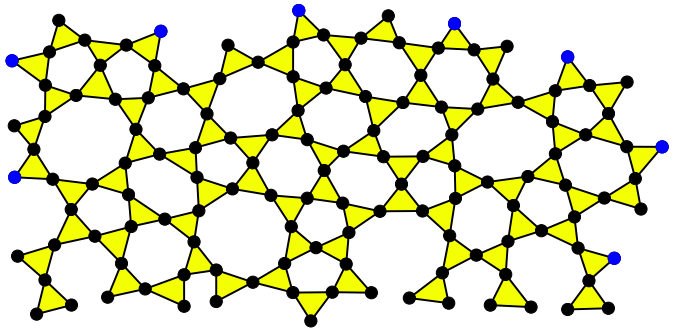

Figure 3.4: Showing a typical subgraph from Figure 3.3 used in the proof that there are no rigid subgraphs larger than a single triangle. (See Lemma 9.)

if it is rigid, but ceases to be so once any joint is removed. These are an examples of body-pin networks [3] from rigidity theory.

The combinatorial model is a graph G that has one vertex for each triangle and an edge between two triangles if they share a corner (Figure 3.6). Since we are assuming genericity, we will identify a geometric realization with the graph G from now on. In what follows, we are interested in a particular class of graphs G, which we call *triangle ring networks*. The definition of a triangle ring is as follows: (a) G has only vertices of degree 2 and 3; G is 2-connected [4] ; (b) there is a simple cycle C in G that contains all the degree 2 vertices, and there are at least 3 degree 2 vertices; (c) any edge cut set [5] in G that disconnects a subgraph containing only degree 3 vertices has size at least 3.

To set up some terminology, we call the degree 2 vertices *boundary vertices* and the degrees 3 vertices *interior vertices*. A subgraph spanning only interior vertices is

[3]Since only two triangles are pinned together at any point, we are dealing with the 2-dimensional specialization of body-hinge frameworks first studied by Tay [107] and Whiteley [108] in general dimensions. In 2D, there is a richer combinatorial theory of "body-multipin" structures, introduced by Whiteley [109]. See Jackson and Jordán [110] and the references therein for an overview of the area.

[4]This means that to disconnect G, we need to remove at least 2 vertices.

[5]This is an inclusion-wise minimal set of edges that, when removed from G, results in a graph 2 connected components.

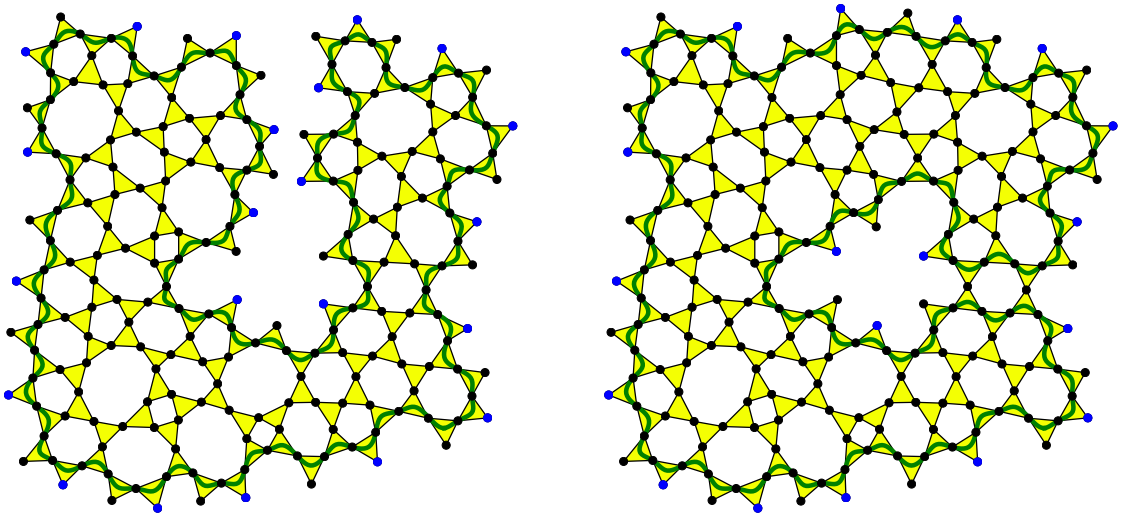

Figure 3.5: Illustrating two, at first sight, more complex anchored boundary conditions that by our results can be used for the sample shown in Figure 3.2, with the 3 purple triangles at the lower right are removed to give an even number of unpinned surface sites. The anchored sites are shown as blue discs, with an even number of surface sites in both graphs. The graph at the right has an even number of surface sites in *both* the outer and inner boundary. The red Si atoms at the centers of the triangles have been suppressed for clarity. The green line goes through the boundary triangles.

an *interior subgraph*.

The reader will want to keep in mind the specific case in which G is planar with a given topological embedding and C is the outer face, as is the case in our figures. This means that subgraphs strictly interior to the outer face have only interior vertices, which explains our terminology. However, as we will discuss in detail later, the setup is very general. If the sample has holes, C can leave the outer boundary and return to it: provided that it is simple, all the results here still apply.

A theorem of Tay–Whiteley [108, 107] gives the degree of freedom counts for networks of 2-dimensional bodies pinned together. Generically, there are no stressed subgraphs in such a network, with graph G, of v bodies and e pins if and only if

$$2e' \leq 3v' - 3 \qquad \text{for all subgraphs } G' \subset G. \tag{3.1}$$

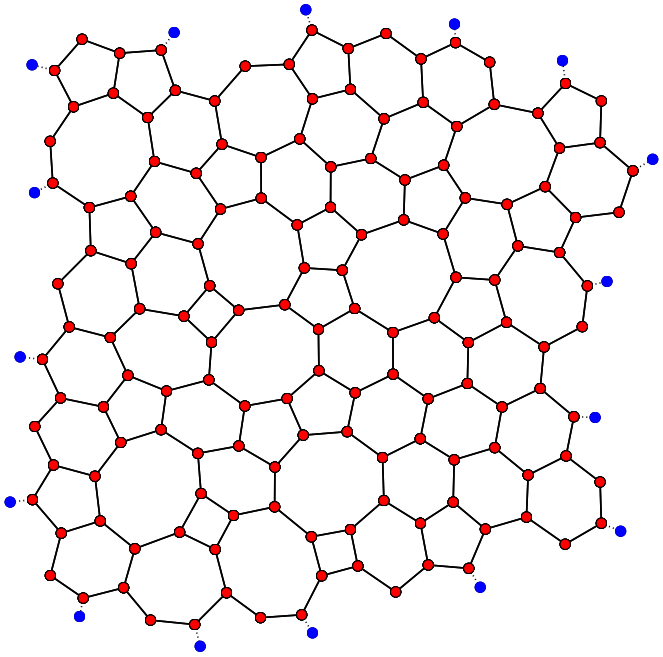

Figure 3.6: The triangle ring network, complementary to that in Figure 3.3, where the Si atoms, shown as red discs, at the center of each triangle are emphasized in this three-coordinated network. Dashed edges are shown connecting to the anchored sites.

where v' and e' are the number of vertices and edges of the subgraph. If (3.1) holds for all subgraphs, the rigid subgraphs are all isostatic, and they are the subgraphs where (3.1) holds with equality.

Lemma 1. *Any triangle ring network G satisfies (3.1).*

Proof. Suppose the contrary. Then there is a vertex-induced subgraph T on v' vertices that violates (3.1). If T contains a vertex v of degree 1 then $T-v$ also violates (3.1) so we may assume that T has minimum degree 2. In this case, T has at most 2 vertices of degree 2, since it has maximum degree 3. In particular, T may be disconnected from G by removing at most 2 edges. If T is an interior subgraph, we get a contradiction right away. Alternatively, at least one of the degree 2 vertices in T is degree 2 in G, and so on C. If exactly one is, then G is not 2-connected. If both are, then $T = G$

and there are only 2 boundary vertices. Either case is a contradiction. □

Corollary 2. *The rigid subgraphs of a triangle ring network G are the subgraphs containing exactly* 3 *vertices of degree* 2 *and every other vertex has degree* 3*. Moreover, any proper rigid subgraph contains at most one boundary vertex of G.*

Proof. The first statement is straightforward. The second follows from observing that if a rigid subgraph T has two vertices on the boundary of G, then G cannot be 2-connected, since all the edges detaching T from G are incident on a single vertex. □

When G is planar, these rigid subgraphs are regions cut out by cycles of length 3 in the Poincaré dual. More generally in the planar case, subgraphs corresponding to regions that are smaller triangle ring networks with t degree 2 vertices have t degrees of freedom.

3.3.2 Anchoring with sliders

Now we can consider our first anchoring model, which uses *slider pinning* [103]. A *slider* constrains the motion of a point to remain on a fixed line, rigidly attached to the plane. When we talk about attaching sliders to a vertex of the graph, we choose a point on the corresponding triangle, and constrain its motion by the slider. In the results used below, this point should be chosen generically; for example the theory does not apply if the slider is attached at a pinned corner shared by two of the triangles. Since we are only attaching sliders to triangles corresponding to degree 2 vertices in G, we may always attach sliders at an unpinned triangle corner.

The notion of rigidity for networks of bodies with sliders is that of being *pinned*: the system is completely immobilized. [6] A network with sliders is *pinned-isostatic* if it is pinned, but ceases to be so if any pin or slider is removed.

[6] Rigid body motions are not "trivial", because slider constraints are not preserved by them.

The equivalent of the White-Whiteley counts in the presence of sliders is a theorem of Katoh and Tanigawa [111], which says that a generic slider-pinned body-pin network G is independent if and only if the body-pin graph satisfies (3.1) and

$$2e' + s' \leq 3v' \qquad \text{for all subgraphs } G' \subset G, \tag{3.2}$$

where s' is the number of sliders on vertices of G'. Here is our first anchoring procedure.

Theorem 3. *Adding one slider to each degree* 2 *boundary vertex of a triangle ring network* G *gives a pinned-isostatic network.*

Proof. Let T be an arbitrary subgraph with v' vertices and v'' vertices of degree at most 2. That (3.1) holds is Lemma 1. The fact that the only vertices of T which get a slider are vertices with degree 2 in G implies that (3.2) is also satisfied, and, by construction $2e + s = 3v$. □

We may think of this anchoring as rigidly attaching a rigid wire to the plane then constraining the boundary vertices to move on it. Provided that the wire's path is smooth and sufficiently non-degenerate, this is equivalent, for analyzing infinitesimal motions, to putting the sliders in the direction of the tangent vector at each boundary vertex. See also Figure 3.2.

3.3.3 Anchoring with immobilized triangle corners

Next, we consider anchoring G by immobilizing (pinning) some points completely. Combinatorially, we model pinning a triangle's corner by adding two sliders through it. Since we are still using sliders, the definitions of pinned and pinned-isostatic are the same as in the previous section.

The analogue for (3.2) when we add sliders in groups of 2 is:

$$2e' + 2s' \leq 3v' \qquad \text{for all subgraphs } G' \subset G, \tag{3.3}$$

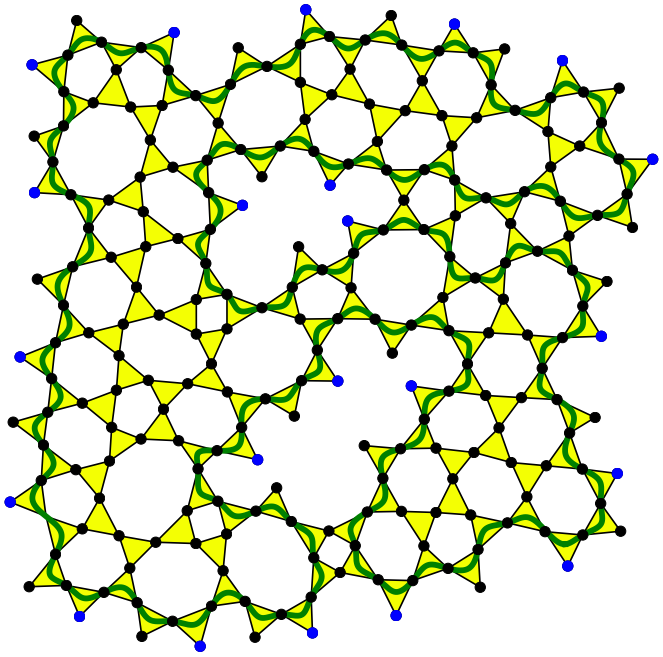

Figure 3.7: Illustrating even more complex boundaries, developed from the sample shown in Figure 3.3 by removing triangles to form two internal *holes*. The boundary sites are shown as blue discs and the 3 purple triangles at the lower left Figure 3.3 have been removed. The red Si atoms at the centers of the triangles in Figure 3.1 have also been removed for clarity. The green line forms a continuous *boundary* which goes through all the surface sites which must be an even number. The anchored (blue) sites then alternate with the unpinned sites on the green boundary curve which has to cross the bulk sample in two places to reach the two internal holes. Here there are 32 boundary sites, 5 boundary sites in the upper hole and 7 in the lower hole, giving a total even number of 44 boundary sites. Where these crossings take place is arbitrary, but it is important that the anchored and unpinned surface sites alternate along whatever (green) boundary line is drawn.

where s' is the number of immobilized corners.

Theorem 4. *Let G be a triangle ring network with an even number t of degree 2 vertices on C. Then, following C in cyclic order, pinning every other boundary vertex that is encountered results in a pinned-isostatic network.*

Proof. Let T be an arbitrary subgraph of G. If at most one of the vertices of T are pinned, there is nothing to do. For the moment, suppose that no vertex of degree 1 in T is pinned. Let t be the number of pinned vertices in T.

We will show that for each of the t pinned vertices, there is a distinct unpinned vertex of degree 1 or 2 in t. This implies that $2e' \leq 3v' - 2t$ in T, at which point we know (3.3) holds for T.

To prove the claim, let v be a pinned vertex of T. Traverse the boundary cycle C from v. Let w be the next pinned vertex of T that is encountered. If the chain from v to w along C is in T, the alternating pattern provides an unpinned degree 2 vertex that is degree 2 in G. Otherwise, this path leaves T, which can only happen at a vertex with degree 1 or 2 in T. Continuing the process until we return to v, produces at least t distinct unpinned degree 2 vertices, since each step considers a disjoint set of vertices of C.

Now assume that T does have a pinned vertex v of degree 1. The theorem will follow if (3.3) holds strictly for $T - v$. Let w and x be the pinned vertices in T immediately preceding and following v. The argument above shows that there are at least 2 unpinned degree 1 or 2 vertices in T on the path in C between w and x on C. Since these are in $T - v$, we are done. □

When there are an odd number of boundary vertices in G, Theorem 4 does not apply. This next lemma gives a simple reduction in many cases of interest.

Theorem 5. *Let G be a planar triangle ring network, with C the outer face. Suppose that there are an odd number t of boundary vertices. If G is not a single cycle, then it is possible to obtain a network with an even number of boundary vertices by removing the intersection of a facial cycle of G with C, unless $G = C$.*

Proof sketch. The connectivity requirements for a triangle ring network, combined with planarity of G imply that the intersection of C and any facial cycle D of G is a single chain. Every boundary vertex is in the interior of such a chain, so some facial cycle D contributes an odd number of boundary vertices. Removing the edges in

$D \cap C$ changes the parity of the number of boundary vertices. □

3.3.4 Anchoring with additional bars

So far, we have worked with networks of triangles pinned together. Now we augment the model to also include bars between pairs of the triangles. We will always take the endpoints of the bars to be free corners of triangles that are boundary vertices in the underlying network G. Combinatorially we model this by a graph H on the same vertex set as G, with an edge for each bar between a pair of bodies. In this case, the Tay–Whiteley count becomes:

$$2e' + b' \leq 3v' - 3 \qquad \text{for all subgraphs } G' \subset G. \tag{3.4}$$

where e' is the number of edges in G' and b' is the number of edges in H spanned by the vertices of G'. The anchoring procedures with sliders or immobilized vertices have analogues in terms of adding bars to create an isostatic network. These boundary conditions are illustrated on the right hand side of Figure 3.8. Also shown in Figure 3.8 in the left panel is a triangular scheme involving alternating unpinned surface sites, that is equivalent to anchoring. In both cases shown here the sample is free to rotate with respect to the page.

Theorem 6. *If G has boundary vertices $v_1, \ldots, v_t$, we obtain an isostatic framework by taking the edges of H to be $v_1v_2, v_2v_3, \ldots, v_{t-3}v_{t-2}$.*

Proof. Consider the $t-3$ new bars. By construction and Lemma 1 we have $2e+t-3 = 3v - t + t - 3 = 3v - 3$. Corollary 2 and the connectivity hypotheses imply that no rigid subgraph of G has more than 1 of its 3 degree 2 vertices on the boundary of G. This shows that no rigid subgraph of G has a bar added to it. □

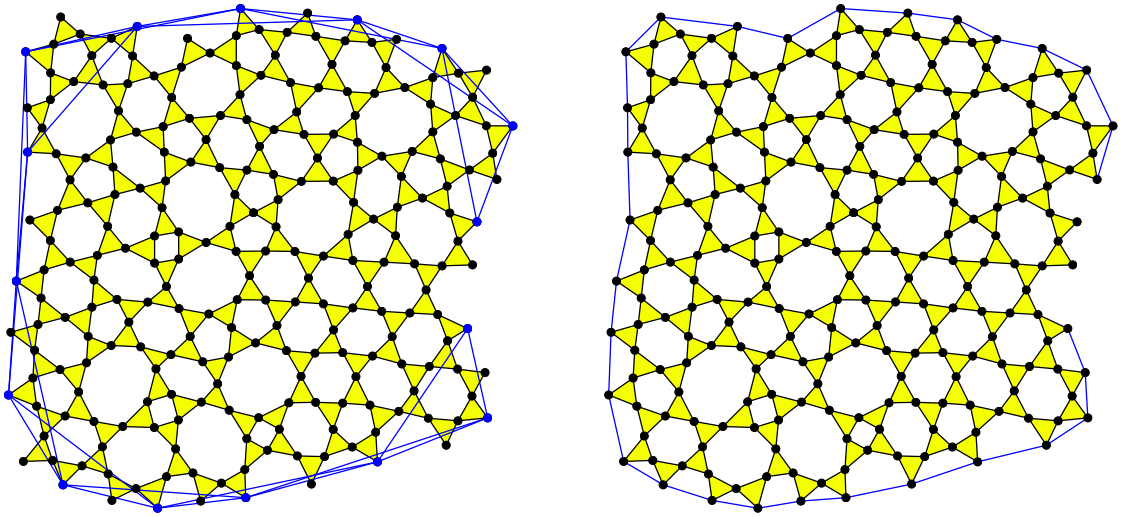

Figure 3.8: Illustrating two additional boundary conditions used for the sample shown in Figure 3.3, with the 3 purple triangles at the lower right removed to give an even number of unpinned surface sites. On the left, alternating surface sites are connected to one another through triangulation of first and second neighbors, with the last three connections not needed (these would lead to redundancy). Hence there are three additional macroscopic motions when compared to Figure 3.3 which can be considered as being pinned to the page rather than to the *internal frame* shown by blue straight lines. On the right we illustrate anchoring with additional bars which connect all unpinned surface sites, except again three are absent, to avoid redundancy, and to give the three additional macroscopic motions when compared to Figure 3.3

Theorem 7. *If G has t boundary vertices and t is even, then taking H to be any isostatic bar-joint network with vertex set consisting of $t/2$ boundary vertices chosen in an alternating pattern around C results in an isostatic network.*

A triangulated $t/2$-gon is a simple choice for H.

Proof sketch. By Lemma 1, we are adding enough bars to remove all the internal degrees of freedom. The desired statement then follows from Theorem 4 by observing that pinning down the boundary vertices is equivalent, geometrically, to pinning down H and then identifying the boundary vertices of G to the vertices of H. □

A result of White and Whiteley[112] on "tie downs", then gives:

Corollary 8. *In the situation of Theorems 6 and 7, adding* any 3 *sliders results in a pinned-isostatic network.*

3.3.5 Stressed Regions

So far, we have shown how to render a floppy triangle ring network isostatic or pinned-isostatic. It is interesting to know when adding a single extra bar or slider results in a network that is stressed over all its members. This is a somewhat subtle question when adding bars or immobilizing vertices, but it has a simple answer for the sliding boundary conditions.

We say that a triangle ring network is *irreducible* if: (a) every minimal 2 edge cut set either detaches a single vertex from G or both remaining components contain more than one boundary vertex of G; (b) every minimal 3 edge cut set disconnects one vertex from G.

Lemma 9. *A triangle ring network G has no proper rigid subgraphs if and only if G is irreducible.*

Proof. Recall, from Corollary 2, that a proper rigid subgraph T of G has exactly 3 vertices of degree 2 and the rest degree 3. Thus, T can be disconnected from G by a cut set of size 2 or 3.

In the former case, Corollary 2 implies that exactly one of the degree 2 vertices in T is a boundary vertex of G. This means that T witnesses the failure of (a), and G is not irreducible. Conversely, (a) implies that, for a 2 edge cut set not disconnecting one vertex, either side is either a chain of boundary vertices or has at least 4 vertices of degree 2.

Finally, observe that cut sets of size 3 are minimal if and only if they disconnect an interior subgraph on one side. Corollary 2 then implies that there is a proper rigid

component that is an interior subgraph of G if and only if (b) fails. □

Theorem 10. *Let G be a triangle ring network anchored using the procedure of Theorem 3. Adding* any *bar or slider to G results in a network with all its members stressed if and only if G is irreducible.*

Proof. First consider adding a slider. Because G is pinned-isostatic, the slider creates a unique stressed subgraph T. A result of Streinu-Theran[103] implies that T must have been fully pinned in G. Since any proper subgraph has an unpinned vertex of degree 1 or 2, (3.2) holds strictly. Thus, the stressed graph is all of G. [7]

If we add a bar, there is also a unique stressed subgraph. This will be all of G, again by the result of Streinu-Theran[103], unless both endpoints of the bar are in a common rigid subgraph. That was ruled out by assuming that G is irreducible. □

3.4 Conclusions

In this paper we have demonstrated boundary conditions for locally isostatic networks that incorporate the right number of constraints at the surface so that the whole network is isostatic. These boundary conditions should be useful in numerical simulations which involve finite pieces of locally isostatic networks. The boundary can be quite complex and involve both an external boundary with internal holes.

Our derivation of the new boundary conditions is based on a structural characterization of graphs which capture the combinatorics of silica bilayers. This shows that the degrees of freedom are associated with unpinned triangle corners on the boundary. We then present two methods to completely immobilize a triangle ring network: by attaching the boundary to a wire rigidly attached to the plane; and by completely immobilizing alternate vertices on the boundary. To render a triangle ring network

[7] It is worth noting that, so far, irreducibility of G was not required. It is needed only for adding bars.

isostatic, we also have two methods: adding bars between adjacent boundary vertices in cyclic order; and attaching alternating boundary vertices to an auxiliary graph that functions as a rigid frame.

Although our definition of a triangle ring network is most easily visualized when G is planar and C is the outer face, the combinatorial setup is quite a bit more general. The natural setting for networks with holes is to assume planarity, and then that all the degree 2 vertices are on disjoint facial cycles in G. The key thing to note is that the cycle C in our definition does not need to be facial for Theorem 4. For example, in Figure 3.7, C goes around the boundary of an interior face that contains degree 2 vertices. In general, the existence of an appropriate cycle C is a non-trivial question, as indicated by Figure 3.7 (See also Figure 3.5 for other examples of complex anchored boundary conditions).

What is perhaps more striking is that Theorem 3 still applies whether or not such a C exists, provided faces in G defining the holes in the sample are disjoint from the boundary and each other.

In applying anchored boundary conditions, it is important that the complete boundary has an even number of unpinned sites, which can include internal holes, which must then be connected using the green lines shown in the various figures. This gives a practical way of setting up calculations with anchored boundary conditions in samples with complex geometries and missing areas.

Support by the Finnish Academy (AKA) Project COALESCE is acknowledged by LT. We thank Mark Wilson and Bryan Chen for many useful discussions and comments. This work was initiated at the AIM workshop on configuration spaces, and we thank AIM for its hospitality.

Chapter 4

REFINING GLASS STRUCTURE IN TWO DIMENSIONS

This chapter is a reprint of the following journal article:

Sadjadi, Mahdi, Bishal Bhattarai, D. A. Drabold, M. F. Thorpe, and Mark Wilson. "Refining glass structure in two dimensions." Physical Review B 96, no. 20 (2017): 201405.

My contributions to this work are the determining atomic positions, developing and implementing an algorithm to correct the unimaged regions of silica bilayers, calculations of the bond angle distributions in the resulting structures from the harmonic potential, molecular dynamics and density functional theory, and the construction of the figures.

4.1 Abstract

Recently determined atomistic scale structures of near-two dimensional bilayers of vitreous silica (using scanning probe and electron microscopy) allow us to refine the experimentally determined coordinates to incorporate the known local chemistry more precisely. Further refinement is achieved by using classical potentials of varying complexity; one using harmonic potentials and the second employing an electrostatic description incorporating polarization effects. These are benchmarked against density functional calculations. Our main findings are that (a) there is a symmetry plane between the two disordered layers; a nice example of an emergent phenomenon, (b) the layers are slightly tilted so that the Si-O-Si angle between the two layers is not 180° as originally thought but rather $175 \pm 2°$ and (c) while interior areas that are not

completely imaged can be reliably reconstructed, surface areas are more problematical. It is shown that small crystallites that appear are just as expected statistically in a continuous random network. This provides a good example of the value that can be added to disordered structures imaged at the atomic level by implementing computer refinement.

4.2 Introduction

The atomic structure of covalent network glasses has been a subject of both experimental and theoretical interest since the introduction of the Continuous Random Network (CRN) model by Zachariasen [18]. Almost all of these studies have focused on the Pair Distribution Function (PDF) which is the Fourier transform of a diffraction intensity pattern [1]. Experimental diffraction studies offer useful information, in particular regarding pair-wise ordering [113]. However, simulation models can greatly aid the interpretation of these data as the atom positions are known unequivocally. As a result, information such as the ring statistics, which is in many ways a natural language for discussing network structure [114, 115, 21], is directly accessible. While this work has been very informative and clearly established the correctness of the CRN model for materials like vitreous silica, it is not accurate enough to distinguish between different models with varying ring statistics *etc.* This situation has changed recently with the direct imaging of bilayers of silica [116, 4] that has provided detailed information regarding atomic positions.

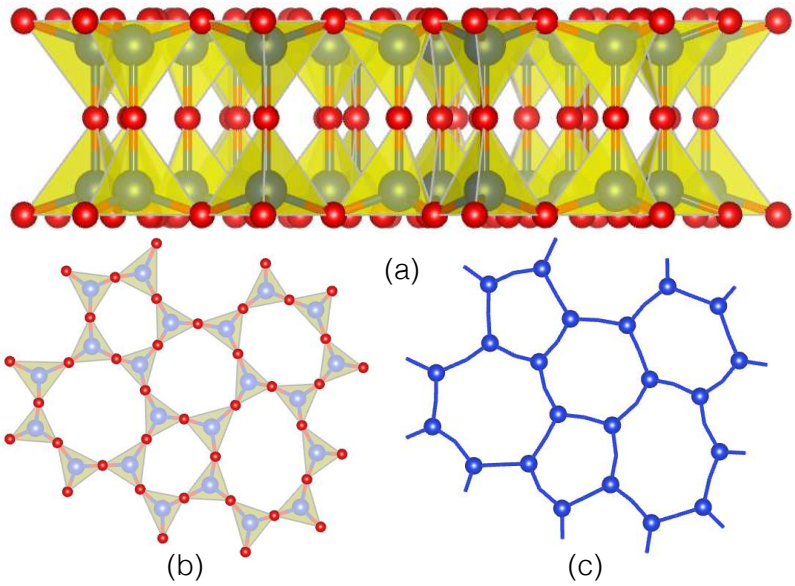

Figure 4.1: (a) A small piece of silica bilayer in which oxygen atoms (red) form a tetrahedral network while silicons (blue) are located at the center of tetrahedra. (b) The top view of the silica bilayer where O and Si atoms are projected into the plane, with O forming a network of corner-sharing triangles. (c) An alternative view where Si atoms form a network of edge-sharing polygons (rings), while oxygens are removed for clarity. This view is stressed in Fig. 4.2.

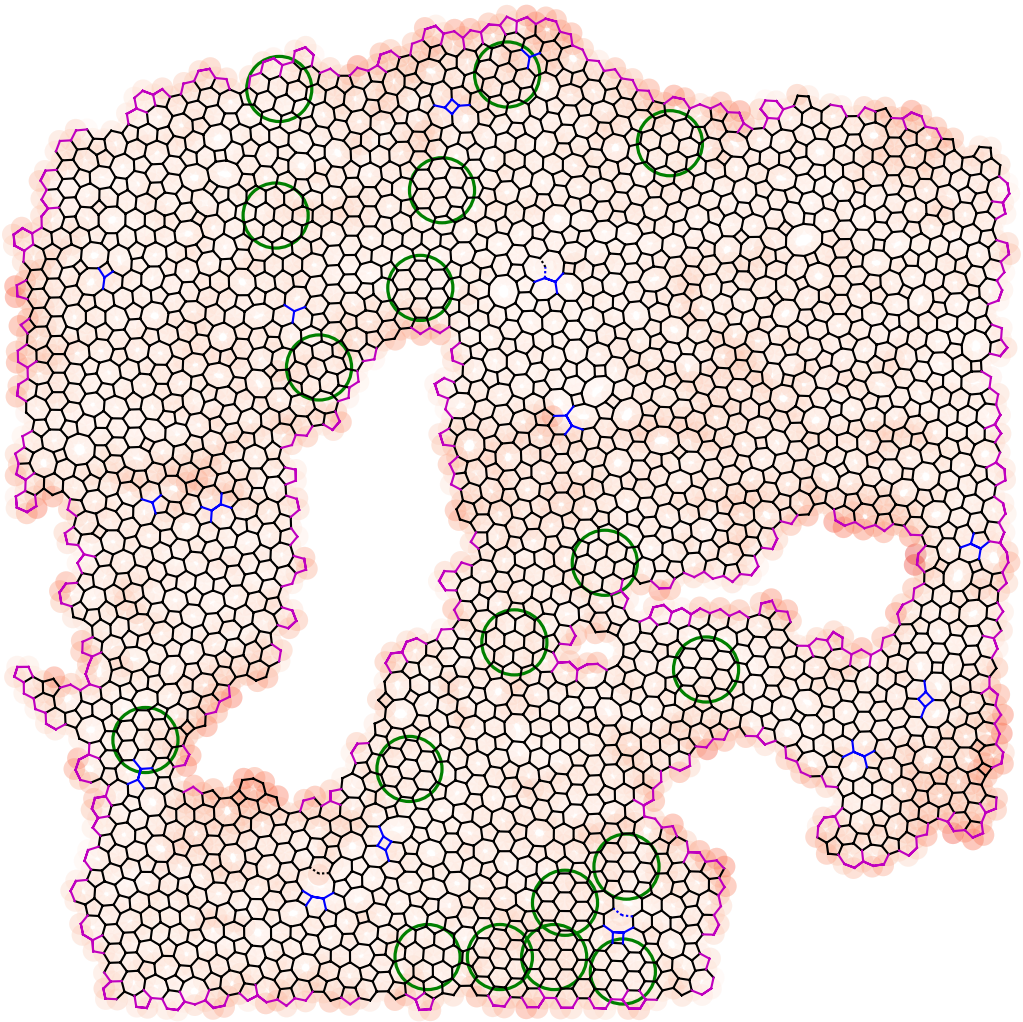

Figure 4.2: The Cornell h network viewed perpendicular to the plane containing the bilayer with the O atoms removed for clarity, and only the top layer of Si atoms shown as *vertices*. The atoms associated with the blue and magenta bonds were not directly imaged but have been added in the computer refinement. The blue and magenta bonds highlight bonds reconstructed within the main body of the sample and at the surface, respectively. Dashed lines highlight small sections in which an under-coordinated Si atom was required for filling. The intensity of the red highlights the difference between the configuration relaxed with the spring and PIM potentials. The green circles show small *crystallites*.

Silica, SiO_2, represents an archetypal network-forming material. At ambient pressure the crystalline and amorphous structures can be considered as constructed from corner-sharing SiO_4 tetrahedral coordination polyhedra (CP) which link to form a network. The complex linking of the CP may result in significant ordering on length-scales beyond the short-range ordering imposed by the system electrostatics (effectively controlled by the relative atom electronegativities) [117, 118, 119, 120, 121, 122].

Recently developed synthetic pathways have allowed thin films of SiO_2 to be deposited on either metallic [123, 29, 116] or graphitic [4] substrates whilst advances in imaging techniques allow for true atomic resolution of the surface structure. Albeit, because the bilayer is a glassy material, it is not commensurate with any substrate, and so we do not include the substrate here.

Some of the thinnest films deposited are bilayers of corner-sharing SiO_4 CP in which all of the Si and O atoms obtain their full (four- and two- respectively) coordination numbers. Amorphous and crystalline films have been grown with both states characterized by the presence of a mirror plane (which houses a layer of O atoms which act as bridges between the two monolayers [124]). Critically, the pseudo-two-dimensional nature of these systems allows the ring structures to be directly observed and hence offers a potentially unique insight into the origin of any ordering on long length-scales. Silica can be considered as a network of silicon atoms in which the nearest-neighbor Si-Si pairs are *dressed* with O atoms. As a result, the crystalline system can be considered as constructed exclusively from a net of six-membered (Si-Si-Si...) rings, whilst the amorphous systems are constructed from a distribution of 4- to 10-membered rings (Fig. 4.1). However, this new experimental information, whilst ground-breaking, is naturally imperfect as the location of each atom has associated with it a natural uncertainty which translates into an uncertainty in atom-atom separations.

In this Letter, we show how value can be added by combining the experimental image with computer refinement that builds in the known local chemistry. Whilst no refinement of the experimental data is required in order to obtain, for example, accurate ring statistics, refinement is required in order to address the geometrical issues associated with the network. For example, value can be added on the effect of the presence of significant unimaged regions as well as on the subtle variations in the structure perpendicular to the resolved plane containing the bilayer.

Here, we focus on a single large sample of a bilayer of vitreous silica imaged by the Cornell group [4] which we will refer to as sample *h*, shown in Fig. 4.2, to distinguish it from previous smaller experimental and computer-generated samples [47]. The sample is $\sim 270 \times 270 \text{Å}^2$ in area containing 19,330 O and 9,492 Si atoms, and is the largest such sample imaged at the atomic level of which we are aware.

Importantly, we are using the whole experimental sample, including voids, rather than selecting a more rectangular shaped section without voids, which would have thrown out most of the experimental data. This is also significant as the full configuration shows a number of interesting features. For example, there are several regions which may be considered nanocrystalline showing relatively large numbers of neighbouring six-membered rings (highlighted by green circles with a diameter of 9 Å). Such regions are to be expected statistically in a CRN and from previous studies [21] we find that about 50% of all rings are sixfold and of these about 2% are surrounded by 6 sixfold rings leading to a little *microcrystallite* of 7 sixfold rings. The total number of rings in the Cornell *h* sample is 1811, where we exclude surface rings that do not have their full compliment of neigboring rings. Thus we expect $1811 \times 0.5 \times 0.02 \approx 18$ of such regions which is fortuitously exactly the number of regions shown by green circles. So this certainly cannot be taken as any evidence for microcrystallites as has been postulated at various times since the original ideas of

Lebedev and coworkers [17].

More obviously the configuration shows three relatively large regions which were unable to be imaged (of approximate dimensions $160\times40\text{Å}^2$, $50\times20\text{Å}^2$ and $10\times10\text{Å}^2$ respectively) which resist reasonable attempts at computational filling (see below). A potential implication is that the underlying surface (on which the bilayer has been grown) in some way distorts the bilayer thus preventing effective imaging or perhaps the network was never formed in these regions because of surface roughness.

To construct the bilayer from the experimental image, O atoms (which are not imaged) are placed midway between Si atoms (which are imaged) thus forming a network of corner-sharing O_3 triangles (each of which has an Si atom at the centre). The Si and O atoms planes are then separated, forming trigonal pyramids with Si atoms at the apices. A mirror image of these pyramids is joined to the original via O-atom bridges to form the completed bilayer, resulting in an initial set of 180^o Si-O-Si bond angles centered around the O atoms in the mirror plane (Fig. 4.1). An important question involves the experimental length metric to ensure the correct calibration of the image. We calculated the mean average length of the imaged nearest neighbour Si-Si distances as 3.097Å, which is close to the expected value of 3.100Å for glassy silica structures [22], confirming the overall accuracy of the experiment, and alleviating the need for any length rescaling. To reconstruct the unimaged regions, we use mean bond length and internal angles of rings to find the correct local topology. The subsequent relaxation of the bilayer will fix the geometry ensuring the proper bond length and angles.

4.3 Computational Details

This relaxation is carried out using model potentials of increasing complexity. In the simplest case, the nearest-neighbour O-O bonds are mimicked by harmonic springs

with lengths set as the mean average (2.645Å). This ensures that the system does not have any internal degrees of freedom and is minimally rigid or isostatic [75, 76]. A hardcore potential is added to prevent overlap of O atoms from different tetrahedra as well as an MSD (Mean-Square Deviation) term which penalizes deviation from the experimental coordinates. This MSD term involves the sum of squares of the refined minus the experimental atomic positions and is important as this maintains the overall area and alleviates the need for additional boundary conditions to maintain the sample area. Although proper boundary conditions for finite pieces of amorphous systems can be designed [48], this simple potential can account for structural information extracted in this Letter. Maintaining the configurational area is critical in avoiding, for example, unphysical overlaps in nearest-neighbour tetrahedra in the absence of formal (electrostatic) repulsions. The balance of the surface extension and the inter-tetrahedral repulsions define an effective flexibility window of acceptable structural solutions, of the type commonly associated with zeolites [125]. As a result, samples with irregular boundary conditions are not a problem.

A second classical model used is a polarizable-ion model (PIM) [126], specifically the TS potential [127] which utilises pair potentials to model the Coulomb, short-range (overlap) and dispersive interactions. The potential employs a combination of reduced ion charges and anion dipole polarisation (as described in reference [126]). The results from the harmonic potential model are used as the input with the PIM further refining the results.

The most sophisticated method applied uses Density Functional Theory (DFT). However, the method is too computationally-demanding to apply to the experimental Cornell h configuration. Therefore, a relatively small 1200 atom periodic computer-generated model (with 200 Si atoms in each monolayer) of a vitreous silica bilayer [64] was used. Density functional calculations were undertaken with the code

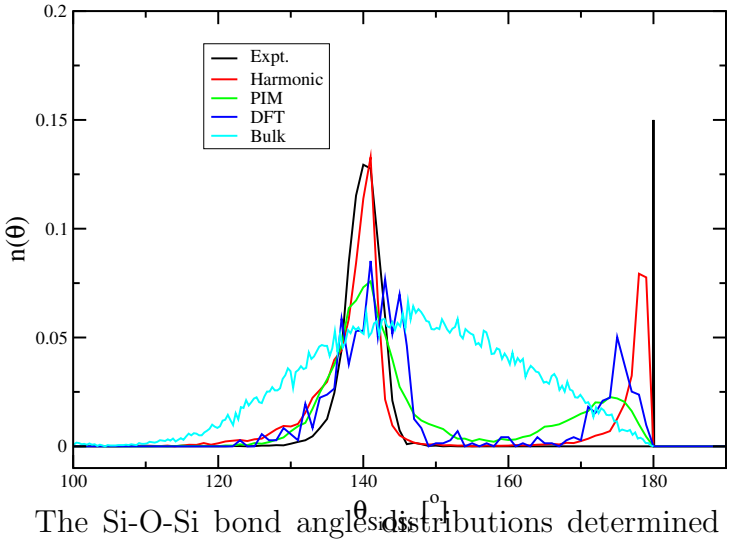

Figure 4.3: The Si-O-Si bond angle distributions determined from the original experimental configuration and from the bilayers obtained using models of increasing complexity as well as for the bulk glass. The peak at $\theta_{\mathrm{SiOSi}} \sim 145°$ arises from the "in-plane" tetrahedral links whilst the peak at $\sim 180°$ arises from the central bridging oxygen atoms between the two planes. The unrefined experimental result for the Cornell *h* sample is shown in black where it was *assumed* that the central bridging angle was exactly 180°. The DFT calculation is on a computer-generated periodic sample and acts as the best guide for what to expect. The other two results are for the refined Cornell *h* sample using both the harmonic model and the polarizable-ion model as described in the text. Both show significant tilting as expected from the results of DFT, while maintaining the central symmetry plane.

SIESTA [128], with single-zeta basis and the local density approximation. Relaxation with a variable cell area resulted in very little change. Stability of the relaxed model was also verified [129].

4.4 Results

The result of the PIM refinement of Cornell *h* is shown in Fig. 4.2. The blue (bulk) and magenta (surface) bonds have been computer-reconstructed, as described earlier. The interior reconstruction was deemed to be successful, as the differences between the spring and PIM models were minor. These differences are shown by the red shading where the darkest red corresponds to an atomic displacement of ~ 0.5Å from

the original (unrefined) coordinates. This strongly suggests that the network existed in these interior areas but was not imaged reliably, rather than the networks growing around a pillar or avoiding surface roughness on the substrate and never existing. At the surface, the difference between the spring and PIM models was much greater as the reconstruction was not contained within a small closed exterior perimeter.

In addition to in-plane information, refinement can provide valuable information in perpendicular direction. As a benchmark of our model potentials, we have studied the Si-O-Si angle, θ_{SiOSi}, as this contains important information on how the tetrahedra are linked. Figure 4.3 shows the distributions of θ_{SiOSi} for three models. The experimental structure (in which linear Si-O-Si bridges between the two monolayers are imposed) shows a bond angle of $\theta_{\mathrm{SiOSi}} \sim 140.3^o$ (with a FWHM of $\Delta\theta \sim 5.2°$) in the bilayer plane. All of the models generate bimodal distributions in which the peak at $\theta_{\mathrm{SiOSi}} \sim 145^o$ may be assigned to the Si-O-Si triplets in the bilayer plane whilst the peaks at $\theta_{\mathrm{SiOSi}} > 175^o$ correspond to the triplets centred around the bridging O atoms in the mirror plane (*i.e.* perpendicular to the bilayer plane). There is not much latitude in the in-plane values of this angle as they must be consistent with the measured area and the known Si-O bond lengths, which leads to a single peak in the $\theta_{\mathrm{SiOSi}} \sim 145°$. Fig. 4.3 shows that the harmonic model reproduces the important high-angle peak at $\theta \sim 178.5°$. The lower-angle peak is at $\theta \sim 140.9°$ ($\Delta\theta \sim 3.8°$) and some way below the DFT result.

The figure also shows the analogous distribution obtained from the model of a bulk glass at ambient pressure using PIM, which is similar to distributions observed in bulk silicates [130, 131]. The bulk distribution is significantly broader than those generated for the bilayer with $\theta \sim 145°$ and $\Delta\theta \sim 36°$. The requirement for the relatively obtuse bond angles which characterise the links between the two layers constrains the in-plane bond angles to a relatively narrow range. For the intra-layer

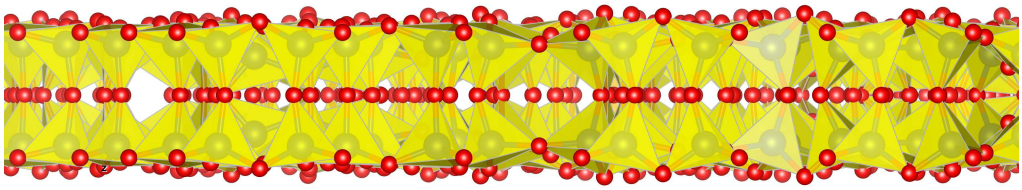

Figure 4.4: A section of the Cornell h network shown along the plane containing the bilayer with O atoms shown in red, and with Si atoms at the center of the yellow tetrahedra. Note the symmetry plane of the central O atoms and also the tilting of the tetrahedra away from the vertical about the central plane.

angles all of the models show peaks at $\theta \sim 140 - 142^{\circ}$ with the harmonic potential showing a far sharper peak retaining the symmetry plane.

However the bridging O angle is tilted and reduced to about 175.1°. A Si-O-Si angle of 180^{o} sits on a local energy maximum [65] and, as a result, tilting is inevitable. A tilt in the inter-layer bond angle is observed in all the models. At the simplest level (harmonic potential) a relatively small deviation from linear ($\theta \sim 178.5^{\circ}$) is shown. As greater detail is added to the models these angles become more acute with both the PIM and DFT results showing peaks at $\theta \sim 175^{o}$. Figure 4.4 shows the configuration perpendicular to the plane containing the bilayer relaxed using the PIM and clearly showing the tilted corner-sharing tetrahedra, with a peak at $\theta \sim 174.9^{\circ}$.

At first sight this suggests an incompatibility with the experimental results where only a single layer is seen, with the second layer of Si tetrahedra being exactly behind and underneath the first. However this can be maintained if there is a symmetry plane involving the central O atoms, such that the upper and lower tetrahedra tilt and pucker in the same way and there is not a second image when the bilayer is imaged from above, as shown in Figure 4.4. This conclusion is supported by an entropy argument in which the bilayer *with* a mirror plane is able to explore configurational space more effectively than one without [124, 132]. There are more degrees of freedom with the symmetry plane present, thus increasing the entropy and lowering the free energy, and hence leading to this unexpected emergent phenomena. Thus symmetry

is induced in a system which at first sight seems a canonical example of a system without symmetry. This argument is confirmed both by detailed atomic computer modeling and by experiment, where no *shadow* is seen beside each atom imaged, so that the second layer must be exactly behind the first layer.

A feature to notice from Fig. 4.2 is that the polygons with silicon atoms at the corners appear regular, having areas close to that of regular polygons as has been previously noted [47]. This feature has been absent in computer generated models of vitreous silica bilayer as the Si-O-Si angle of around 145° in the plane is hard to achieve in models while maintaining the maximal convexity of Si polygons. Nature has found a way and we need to understand better how this is achieved. Note there is no difficulty in achieving regular polygons in samples of amorphous As [64] where there are no bridging atoms to contend with.

4.5 Conclusion

In this Letter we have described how computer-refinement can add value to experimental images of disordered structures at the atomic level. Although this is the first time this has been attempted with an amorphous structure, with advances in imaging, many more such systems are expected to be imaged in the near future. This somewhat parallels the procedures employed to rationalise protein structure where the local chemistry, via bond lengths *etc* is included to produce the best possible structure [133]. We have shown that simple potentials are adequate here, and as well as producing refined coordinates for the bilayer (available upon request), we have shown that the two layers are tilted while maintaining a flat central symmetry plane of O atoms between the upper and lower parts of the bilayer. It is remarkable that such symmetry can exist in disordered system and this can be viewed as a nice clean example of an emergent phenomena.

Future work will help determine how ubiquitous bilayer structures of this type may be. It is possible, for example, that forming such structures for systems such as GeO_2 may be more problematic as a significantly larger tilt ($\theta \ll 180°$) would have to be accommodated [65].

We should like to thank Berlin and Cornell groups for the coordinates of their networks and for useful discussions. This work used the Extreme Science and Engineering Discovery Environment (XSEDE), which is supported by National Science Foundation grant number ACI-1548562 [134]. Support through NSF grants # DMS 1564468 (MFT) and # DMR 1506836 (DAD) is gratefully acknowledged.

Chapter 5

THE QUEST FOR TUNNELING MODES

5.1 Introduction

Glasses are an important class of materials not only because of their wide range of applications, but because some of their properties deviate from that of crystals. In 1971, Zeller and Pohl published their measurements of the thermal conductivity and the specific heat of crystalline and noncrystalline silica (SiO_2) and germania (GeO_2) [11]. They showed that the specific heat of vitreous state is very different from the crystal at temperatures $T < 1$ K (Fig. 5.1). While the heat capacity of crystals followed the expected Debye T^3-law, the glassy states demonstrated an additional dependence which was linear in temperature. Therefore they proposed a modified equation for the heat capacity C_V:

$$C_V = aT + bT^3, \tag{5.1}$$

with a and b being coefficients attributed to the anomalous behavior and the expected Debye model, respectively. The experimental values are: $a = 12 \times 10^{-4}$ J kg^{-1} K^{-2} and $b = 18 \times 10^{-4}$ J kg^{-1} K^{-4} [135].

As a background, it is worth mentioning that the difference between glasses and crystals is not limited to the thermal properties. For examples, Golding and Graebner in 1976 discovered the existence of the so-called "phonon echo" in silica glass [136, 137]. They injected two acoustic pulses into fused silica glass with the identical frequency but a time delay. In addition to the reflected pulses from the boundary, they observed a third pulse with the same exact frequency. A few years later, they also

reported the existence of the acoustic saturation [138]; in saturation the first pulse is much stronger than the delayed acoustic pulse, therefore the first signal saturates the interaction with the energy levels.

This chapter is focused on the tunneling properties of glasses. First we review the thermal properties of solids and then we study the two-level systems which are proposed to explain the anomalous low-temperature behavior of glasses. Such tunneling states, and their geometrical manifestation have puzzled researchers for nearly five decades. 2D glasses are a good new place to look for such states as we have access to the actual coordinates of a glass and the visualization of tunneling modes is easier. We propose a new method in 2D to find such tunneling states and study the properties of the found states. While this method leads to new states, it is unlikely that they account for the low-temperature anomalous properties of glass and more work is required.

5.2 Thermal Properties of Solids

In solid state physics, the specific heat is often studied in three temperature regimes. At high temperatures, a classical solid can be thought of as a collection of the classical harmonic oscillators, each of which has two degrees of freedom (kinetic and potential energy terms) in each spatial dimension. Therefore, a particle in d dimensions has $2d$ degrees of freedom. According to the equipartition theorem, each degree of freedom has an equal share of $k_BT/2$ (k_B is the Boltzmann's constant) of the total energy. With N atoms, there are $2dN$ degrees of freedom and hence the total energy is:

$$U = dNk_BT. \tag{5.2}$$

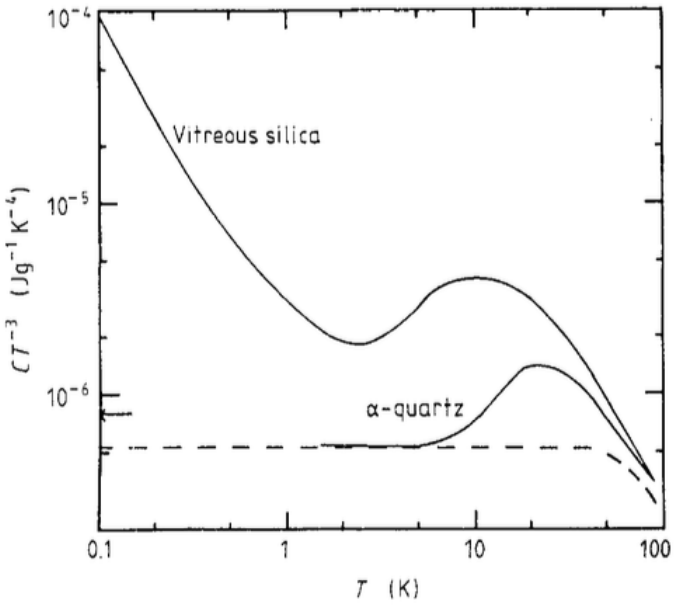

Figure 5.1: The specific heat of silica in crystalline and vitreous states, Reproduced from [10]. The vertical axis represents the specific heat divided by the temperature cubed ($C_V T^{-3}$) and the horizontal axis is the temperature (T) in Kelvin. While at lower temperatures, $C_V T^{-3}$ of the crystalline $\alpha-$quartz tends to a constant value in agreement with the Debye's law, the non-crystalline silica increases like T^2, compatible with the modified Eq. 5.1.

For a mole of the substance ($N = N_A =$ Avogadro's number) the specific heat at constant volume is:

$$C_V = \left(\frac{\partial U}{\partial T}\right)_V = dN_A k_B = dR \tag{5.3}$$

where $R \approx 8.31\,\mathrm{J/K/mol}$ is the gas constant. The above value for $d = 3$ is called the Dulong and Petit value and correctly describes the specific heat of many solids at high temperatures, often down to the room temperature [135].

However, as quantum effects become increasingly important at lower temperatures, the picture of classical harmonic oscillators breaks down. At low-temperatures, the available thermal energy $k_B T$ is significantly smaller than the spacing between energy levels and the energy levels can no longer be thought of as a continuum. According to the law of Boltzmann distribution, in thermal equilibrium the relative population of two states separated by energy $\hbar\omega$ is proportional to $e^{-\hbar\omega/k_B T}$ (Boltz-

mann's factor), where $\hbar$ is the Planck's constant, and ω denotes the angular frequency of harmonic oscillators. Using the distribution law and the quantization of the energy levels, Einstein developed a model which described how the heat capacity decreases at lower temperatures [139, 140]. At high temperature ($\hbar\omega \ll k_B T$), quantum harmonic oscillators behave as their classical counterparts and the Einstein model, hence, explains the high and medium temperature regimes. However, this model predicts that the specific heat approaches zero as $e^{-\hbar\omega/k_B T}$ for $T \to 0$, which is inconsistent with the experimental data as they show at very low temperature, the variation in specific heat is as T^3 not as exponential.

At the very low-temperature ($\hbar\omega \gg k_B T$), thermal properties of solids are dominated by the low frequency lattice vibrations. The low frequency vibrations correspond to the wavelengths λ which are much longer than the typical spacing between atoms. Effectively, in this regime, the solid looks like an elastic continuum medium. Because the available thermal energy is of order of $k_B T$, it seems reasonable to assume only modes with energy $\hbar\omega < k_B T$ can be significantly excited. Debye approached this problem by quantizing the lattice vibrations, i.e. *phonons* and assumed that the solid is isotropic [141]. In agreement with experiments, the Debye model predicts that the specific heat C_V at very low-temperature is proportional to T^d where d is the spatial dimension (i.e. the number of degrees of freedom for a single atom) [135].

To see this, let $e^{i\mathbf{k}.\mathbf{r}}$ be a vibrational wave with the wavevector $\mathbf{k}$ and the wavenumber $k = |\mathbf{k}|$ confined within a $d-$dimensional cubic crystal with periodic boundary conditions (PBCs). The boundary conditions require that $k_i L\,(i = 1, \ldots, d)$ be an integer multiple of 2π. In $k-$space, these points may be represented by a simple cubic lattice with the lattice constant $2\pi/L$. There is one mode in every $(2\pi/L)^d$ unit of the volume. The total number of modes with a wavevector less than k is proportional

to the volume of a sphere in the reciprocal space and equal to:

$$\left(\frac{L}{2\pi}\right)^d \frac{\pi^{d/2}}{\Gamma(1+d/2)} k^d \tag{5.4}$$

where Γ is the the gamma function and $V = L^d$ is the volume. The density of states $D(\omega)$ is:

$$D(\omega) = \left(V \frac{d(\sqrt{4\pi})^{-d}}{\Gamma(1+d/2)}\right) k^{d-1} \frac{\mathrm{d}k}{\mathrm{d}\omega} \tag{5.5}$$

The pre-factor is not important for the scaling of the density of states $D(k)$ as it is independent of k. Using the above, the number of modes between k and $k + \mathrm{d}k$ is proportional to k^{d-1} or ω^{d-1}. The last statement follows from the dispersion relation $\omega = vk$ where v is the wave velocity. Therefore, the number of modes (the density of state) having angular frequency between ω and $\omega + \mathrm{d}\omega$, scales as:

$$D(\omega) \propto k^{d-1} \frac{\mathrm{d}k}{\mathrm{d}\omega} \propto k^{d-1} \propto \omega^{d-1}. \tag{5.6}$$

The internal energy, U of the solid is the sum of the energy of all vibrational modes weighted by the Bose-Einstein factor since phonons are bosons:

$$U \propto \int \mathrm{d}\omega \omega^{d-1} \left(\frac{\hbar\omega}{e^{\hbar\omega/k_B T} - 1}\right) \propto T^{d+1} \int_0^{x_m} \mathrm{d}x \frac{x^d}{e^x - 1} \tag{5.7}$$

where $x = \hbar\omega/k_B T$. Technically, x_m is chosen such that the total number of modes is $3N$ but in $T \to 0$ regime $x_m \to \infty$ and therefore the integral in the above converges to a constant. Finally, we can show that the heat capacity C_V scales as:

$$C_V = \left(\frac{\partial U}{\partial T}\right)_V \propto T^d, \tag{5.8}$$

which for $d = 3$ gives the expected Debye's T^3-law. This is the origin of cubic term in Eq. 5.1 which was predicted as the universal behavior of solids as $T \to 0$. The additional linear term observed in glasses is indeed surprising as the long-wavelength phonons are sound waves propagating through an elastic medium. We

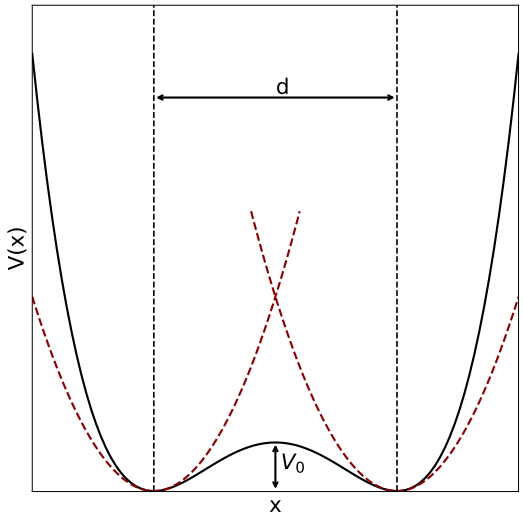

Figure 5.2: A symmetric double-well potential with the separation d between its minima and the barrier height V_b. The harmonic approximations at the minima are shown in dashed red.

know that sound waves can travel through the glasses, therefore there should be little difference between thermal properties of crystalline and glassy states of matter in this temperature regime. Nevertheless, anomalous behavior of the specific heat is observed in numerous studies and glasses have access to additional degrees of freedom compared to crystals. While silica glasses studied here are at the isostatic point and central forces are enough to stabilize the structure, tunneling does occur in low-coordination glasses but additional angular forces are required to stabilize the structure which makes them more complex for a pilot study, therefore we focus on a silica bilayer.

To explain this anomalous behavior, Anderson-Halperin-Varma [142] and Phillips [143] independently proposed a tunneling mechanism in early 1970's [10]. In this model, the atoms in glass unlike atoms in crystal have access to multiple configurations. These configurations sit at local minima of energy landscape while are separated by a barrier (Fig. 5.2). The quantum tunneling of atoms between two local minima provides a linear specific heat, as will be shown shortly. This tunneling is geometrically a conformational change in the position of (a group of) atoms. Since the temperature

is low, this conformational changes should involve a finite number of atoms and it is expected that the atomic rearrangements are localized. The height of energy barrier V_0 is bounded by two extremes. On one hand, the barrier should be small enough that tunneling can occur since the tunneling probability decreases exponentially by V_0. On the other hand, the barrier should be large enough that two localized states are separated.

A detailed account of the two-level systems, and the derivation of their specific heat is given in Appendix B. Appendix C describes the quantum effects of tunneling states by solving the Schrodinger equation for a double-well potential.

Although the two-level systems can successfully explain the linear dependence of the specific heat at low temperature, they neither provide a detailed geometrical mechanism for tunneling nor a process to find such states. The exact mechanism (geometrical realizations) of tunneling is still an open problem after nearly 50 years. In the following section, we present a new formulation of the problem based on the rigidity of the isostatic networks (defined below) and discuss possible approaches to find alternative conformations for an isostatic glass.

5.3 2D Amorphous Networks: Rigidity Theory

We can reframe the problem of tunneling states in the language of graph theory. For examples, silica can be viewed as a network of tetrahedra that are connected at their apex. In 2D, a monolayer of silica can be viewed as a network of corner-sharing triangles. In both cases, the network is a graph which contains the information about which atoms are bonded. Each atom is considered a *vertex* while each chemical bond is an *edge*[1]. In addition, the glassy networks contain information about the bond lengths which are set by quantum mechanics of atoms involved in bonding. In

[1]The terms "site" and "node" are used interchangeably here as are "edge" and "bond".

rigidity theory, the combinations of an underlying graph and the length of edges is called a *framework*. Indeed, silica is a framework where the distance between say oxygen atoms is fixed at ~ 2.626Å. One of the central questions in rigidity theory is the problem of finding realizations of a framework or *graph drawing problem*: Given a graph (how atoms are connected) and the length of edges (distance between the labelled atoms), how many ways are there to draw the graph? If there is only one way to draw the graph, it is called *globally rigid*. A graph with more than one realization can only be *locally rigid*. Note that in counting the number of realizations, trivial motions are ignored because we can translate, rotate, invert or reflect a realization and assign new coordinates to vertices but the drawings are not considered distinct.

We can immediately see how this problem relates to the tunneling states in glasses. If the glass is a framework that can tunnel between multiple conformations, each conformation is in fact a realization of its underlying graph. Therefore glass is not globally rigid and the problem of glassy tunneling states reduces to the problem of finding realizations of a framework.

For the remaining part of this chapter, the focus is on two-dimensional glasses for two reasons. Firstly, silica bilayers are effectively two-dimensional materials since the configuration of the top layer is the mirror image of the bottom layer [9]. The planar nature of a silica bilayer allows us to visualize the geometrical signatures of any possible tunneling states. Secondly, we have a complete characterization of rigidity in two dimensions through Laman's theorem [100], which is yet to be generalized to higher dimensions. In general, to determine whether a framework is rigid is a NP-hard problem [144]. The assumption of a *generic* framework makes the problem much easier. A framework is generic when coordinates of vertices are algebraically independent which loosely means there is no special relationship between coordinates and no symmetry is present in the framework.

The study of the framework rigidity dates back to Maxwell [105]. The idea is based on the balance of the number of constraints N_c and the number of degrees of freedom. Usually constraints are due to the central force bonds when the degrees of freedom are due to the coordinates of vertices. For a framework in d dimensions with N vertices, we need dN numbers to fully describe the position of all vertices. Each edge that is placed between two vertices constrains one of those numbers. Therefore, a naive count would compute the number of remaining degrees of freedom (or *floppy modes*) F as:

$$F = dN - N_B + R \tag{5.9}$$

where N_B is the number of edges and R is the number of redundant edges that are not necessary for rigidity. Constraints can be of other types such as fixing/pinning a vertex in place, or allowing motions only along a vector or on a plane (see Chapter 3 and [103, 48, 145]).

This count can be done rigorously by forming the dynamical matrix (or Hessian matrix of potential energy). The dynamical matrix is symmetric, and positive semi-definite in mechanical equilibrium and its eigenvalues are positive or zero [146]. The number of zero modes is equal to the floppy modes of the system, i.e. deformations that have no energy cost. The number of non-zero eigenvalues is the *rank* of the dynamical matrix. The null space of the dynamical matrix is an $F-$dimensional space which is spanned by the corresponding eigenvectors. The null space contains trivial motions (*e.g.* translations and/or rotations) as well as non-trivial zero modes. However, finding rank of a large matrix is computationally expensive. Fortunately, the *pebble game* is an integer combinatorial algorithm [147] based on Laman's theorem which can determine the rigidity of networks containing up to about 10^6 vertices [101, 102]. The algorithm can decompose the graph into rigid, overconstrained, and underconstrained subgraphs.

A graph is called *isostatic* when it is minimally rigid, *i.e.* it has just enough constraints to support the degrees of freedom with no redundant edges. The isostatic frameworks are on the marginal point of stability and instability and their properties are of much interest [55, 76, 99]. Interestingly, models of glasses are exactly at the isostatic point. In two (three) dimensional silica, every oxygen has $2\times2 = 4$ ($3\times2 = 6$) incident edges which exactly balance 2 (3) degrees of freedom of an atom since the edges are shared between two atoms.

The thread that connects isostaticity of glasses to their tunneling states is a remarkable theorem that states a *generic isostatic* framework has an *even* number of realizations [147, 148]. To be more precise:

Theorem 11. *A finite generic isostatic framework is not globally rigid, but has an even number of equivalent generic frameworks. Each generic framework of the underlying graph is locally rigid. (Equivalent generic networks have the same network topology and bar lengths, and are infinitesimally rigid.)*

This theorem is powerful as it suggests that glasses such as silica *have to* have more than one realization with the same topology (same set of edges). Now, note that the theorem guarantees the existence of such solutions, but the question of their accessibility depends on the energy considerations. In the next section, we justify this theorem using a toy model and will show how various realizations of an isostatic framework can be found.

5.4 An Isostatic Framework: Trihex Example

Although glasses are the main subject of finding tunneling states, a simple example can show the details and shed light on how realizations of a graph are formed. In this section, we study an isostatic framework named *Trihex* (Fig. 5.3). The aim is to

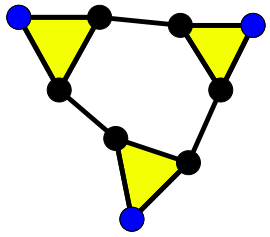

Figure 5.3: Trihex, formed by three corner-sharing triangles arranged around a non-regualr hexagon; an examples of an isostatic framework. Three blue points are pinned to the plane while black points are free to move.

find all realizations of Trihex. It has $N = 6$ vertices free to move with 2×6 degrees of freedom and $N_B = 12$ edges as constraints, which makes the number of floppy modes equal to zero, therefore the framework is isostatic. Note that the blue vertices are pinned (immobilized). Also, the pinned vertices are placed generically (not on an equilateral triangle) but all edges are assumed to have the same length. This situation is similar to the glasses because the bond lengths can be assumed fixed. Let (x_i, x_j) be the coordinates of vertex i. If vertices i and j are connected through an edge with the length s_{ij}, we can write:

$$(x_i - x_j)^2 + (y_i - y_j)^2 = (s_{ij})^2. \tag{5.10}$$

Such an equation can be written for all edges. This gives a set of 12 non-linear equations for Trihex with exactly 12 unknowns (recall the system is isostatic). Each framework realization corresponds to a real solution of this set, assuming three pinned vertices as fixed constraints [2] .

Although Theorem 11 states that the number of realizations is evenly degenerate, it does not provide an exact number. This is due to the fact that given the constraints

[2]The equations can be solved numerically using "NSolve" function in Mathematica. However, this method is limited to graphs with ~ 20 edges based on our numerical experiments.

in a problem, the number of realizations of edge length equations can change by varying edge lengths. In the Trihex example, three vertices are pinned and triangles are equilateral. Therefore it is almost trivial to see that if edge lengths are chosen so short, the triangles cannot span the distance between two pinned vertices. Therefore at that limit, there is no solution/realization[3]. If we take the structure in Fig. 5.3 as an initial structure, we are interested in counting the total number of realizations for a given edge length. This realization are found by solving Eq. 5.10 for uniform edge lengths ranging from 0.95 to 2. The pinned boundary conditions is convenient since no trivial translation or rotation is present [48]. Figure 5.4 shows the results. The red line shows the total number of distinct *complex* solutions for the Trihex which is fixed and equal to 112 computed using Magma [149]. This number is independent of the chosen edge length and is the upper bound on the number of realizations. By changing the edge length, some but not all of complex solutions become real.

The first real solutions appear to be a single point at edge length ≈ 0.969. This is an interesting point as it seems the theorem is violated but in fact there are two solutions at this limit although infinitesimally close. This is the signature of a fully stretched network which has the maximum possible volume or the lowest density. From this point of view, the problem is also related to the flexibility window in glasses where naturally-occurring glasses are found near their low-density limit [150, 132]. As we increase the edge length, the two infinitesimally close solutions diverge and quickly two new solutions join the previous solutions. The number of realizations in Figure 5.4 generally increases up to a maximum number. In fact, two sharp increases happen at ≈ 1.4 and ≈ 2.8 which both are related to the fact that the pins are roughly ≈ 1.4 units apart. When the edge length of the triangles is roughly an integer multiple of this length scale, the triangles can tightly fit together. Figure 5.5 shows some

[3]Zero is still even!

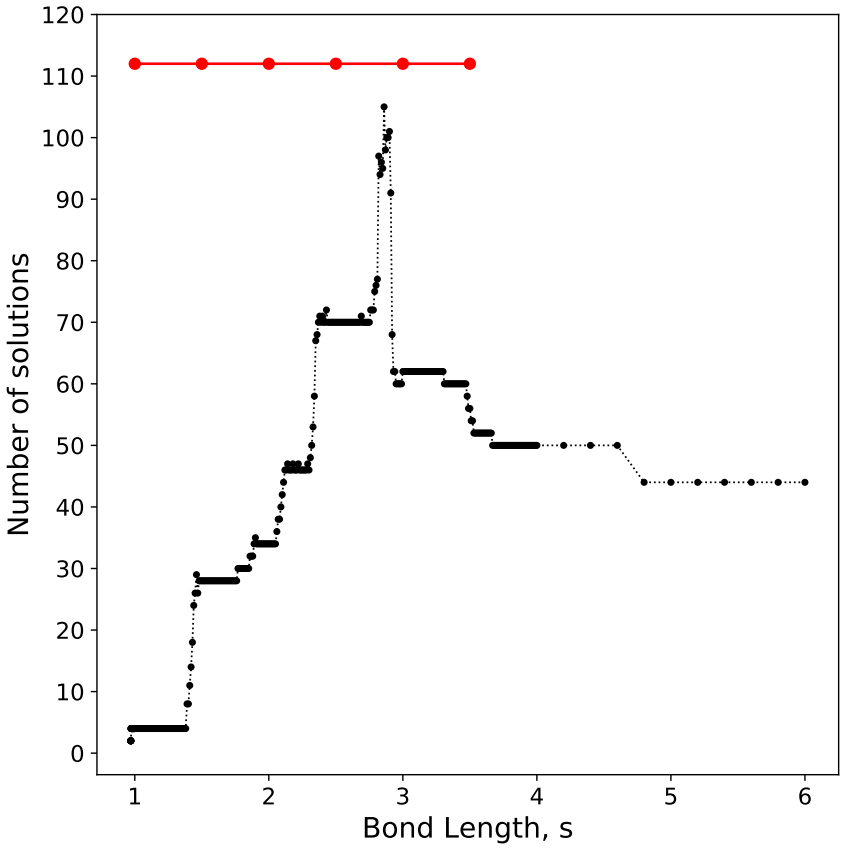

Figure 5.4: Number of realizations of Trihex by varying edge length. The red line shows the number of complex solutions which is fixed at 112.

realizations (out of total 76 possible realizations) for the edge length 2.8.

After reaching a maximum of 104 realizations, the number of solutions rapidly drops. Our numerical experiments show that a subset of solutions survive even at very large edge lengths (high density) and the number of realizations reaches a plateau of 44 solutions. Fig. 5.4 shows the number of solutions for edge lengths up to 6. However, Fig. 5.6 lists these 44 states when the edge length is set to 100, in the units where the distance between pinned vertices is ≈ 1.4. Many solutions in this regime are related by an approximate mirror symmetry, as we expect the three blue pins to be co-incident and the equilateral triangles are roughly arranged around a central point.

Although it is interesting to look at the individual solutions but we need to distinguish various realizations. In addition, it should be monitored how solutions at an edge evolve from the previous solutions. We choose the mean distance of vertices from the centroid of the pinned vertices as the metric. If we plot this metric versus the edge length for each realization, the result is Figure 5.7, showing how some solutions persist for a long range but others disappear. Red and green lines respectively show the linear and quadratic fit to the persistent paths which shows an intermediate growth rate. Previously, we discussed that there is a sharp increase in the number of realizations at s around 1.4 and 2.8. Fig. 5.7 shows that along those values there is a tremendous amount of activity and a large set of solutions are only present in a small region of edge lengths.

The complexity of paths in Fig. 5.7 makes it certainly constructive to look at specific regions in more details. Our observations show that new solutions always come in as a pair. Based on the results, we have observed three mechanisms for appearance/disappearance of solutions: *simple close circuits*, *open circuits* and *retrogrades*, but we have found no evidence of *bifurcation* [151, 152](Fig. 5.8, left panel). A retrograde is a path that bends backward which is a disappearance mechanism; an example is given in the right panel of Fig. 5.8. Open circuits are the persistent paths that continue to exist even at very large edge lengths. An example of simple close circuits is given in Fig. 5.9. The initial solutions at the low-density limit are emphasized in Fig. 5.9 (left panel). Note that first two solutions emerge and then they diverge. At a secondary point, a new branch of solutions appears.

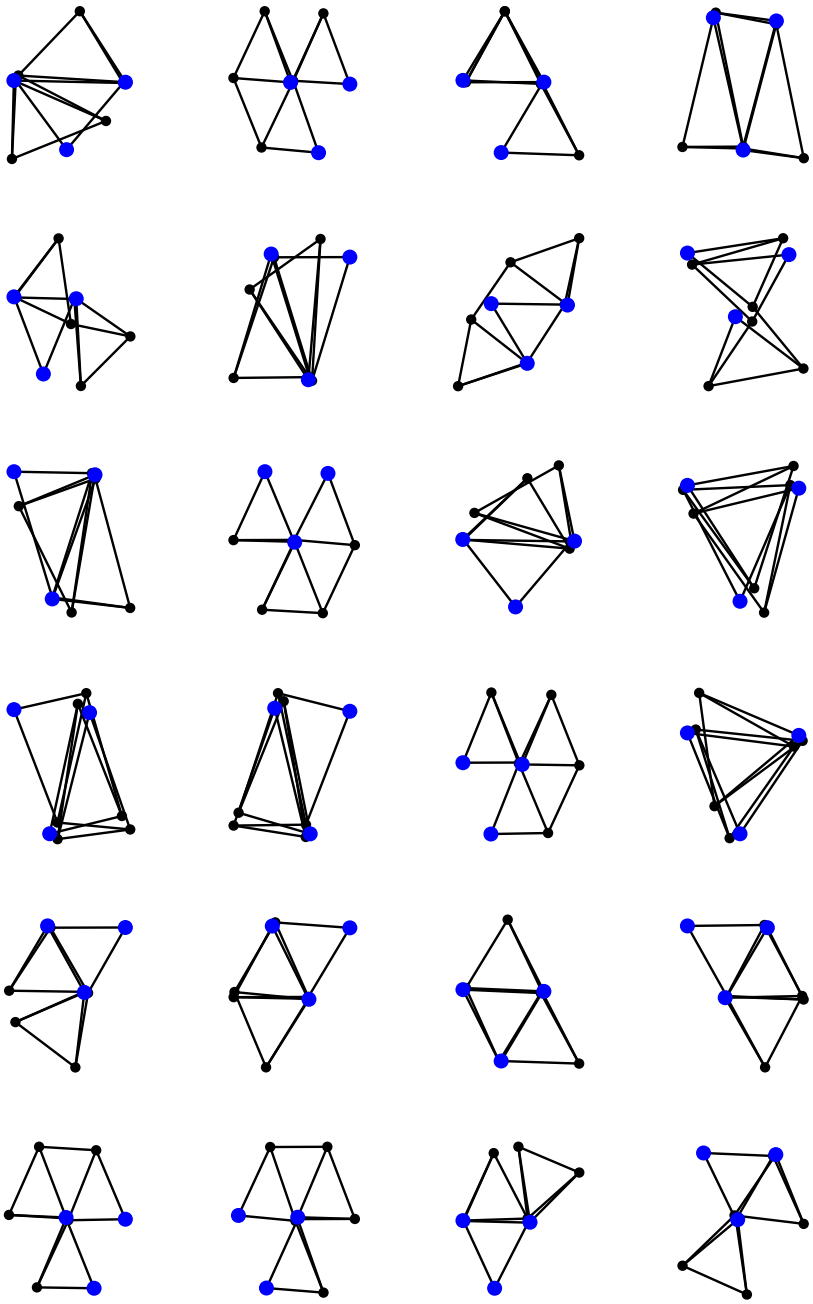

Figure 5.5: Some of the realizations with the edge length equal to 2.8. Note that the structures are generally folded and thicker edges correspond to the overlap of multiple edges.

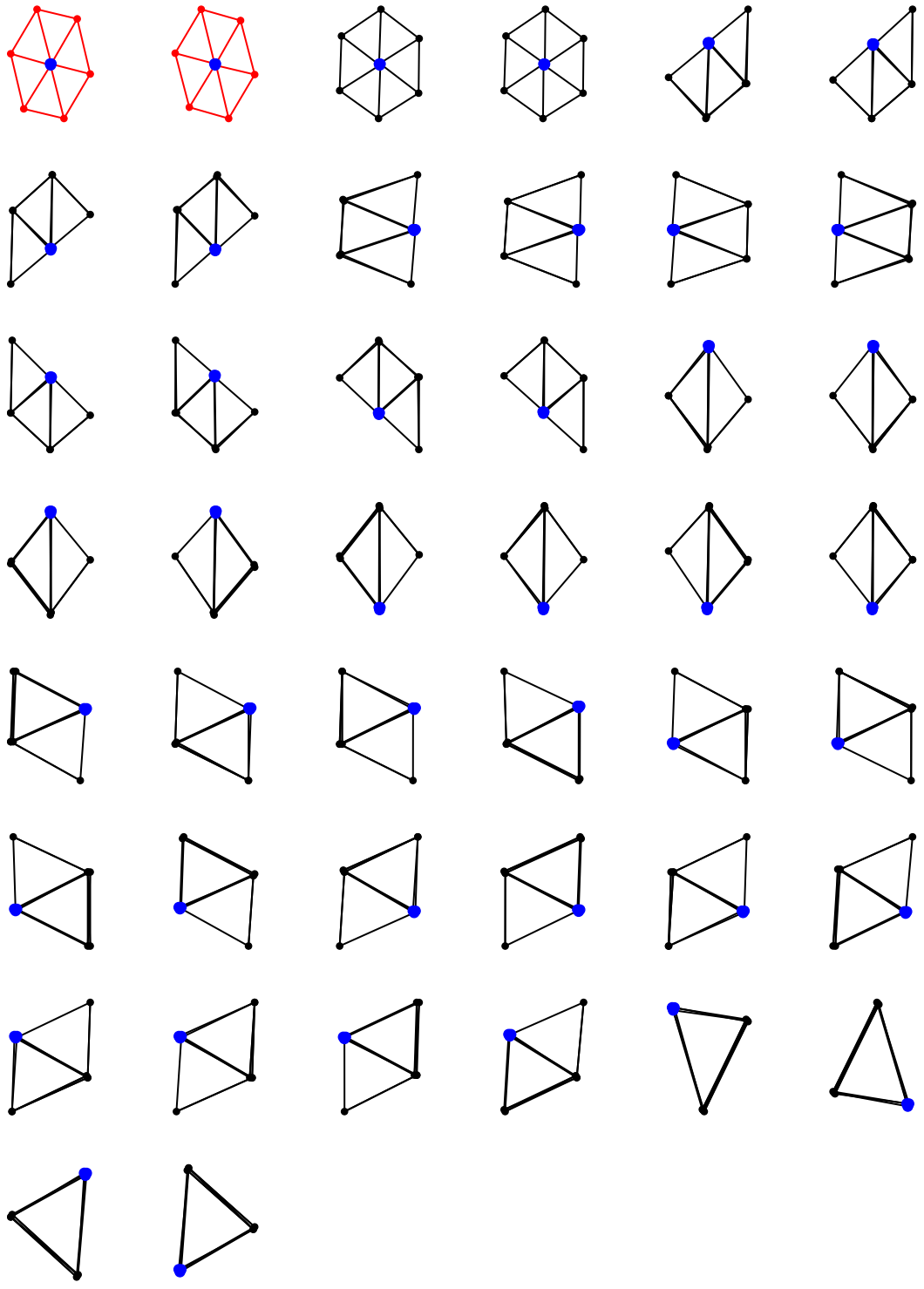

Figure 5.6: The 44 solutions in the large edge length limit. In the units where the distance between the pinned sites is ≈ 1.4, the edge length is set to 100 and three pinned point look like a single point. Similar solutions are related by an approximate mirror symmetry but not rotation. Note that the structures are generally folded and thicker edges correspond to the overlap of multiple edges.

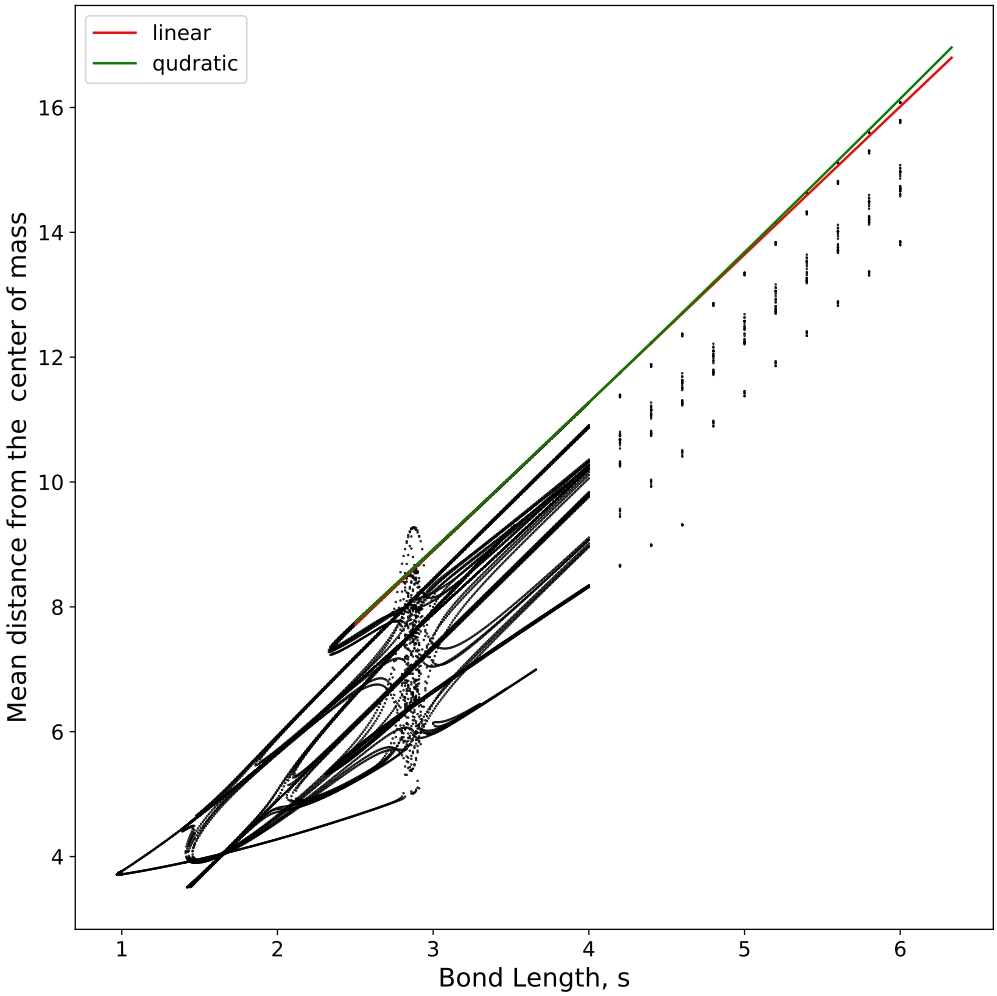

Figure 5.7: (Top) L by varying edge length; (Bottom) The mean distance scales quadratically (green) not linearly (red). The two curves are fitted to the topmost points with edge length between 3 and 4 but are extrapolated to the outside of this window.

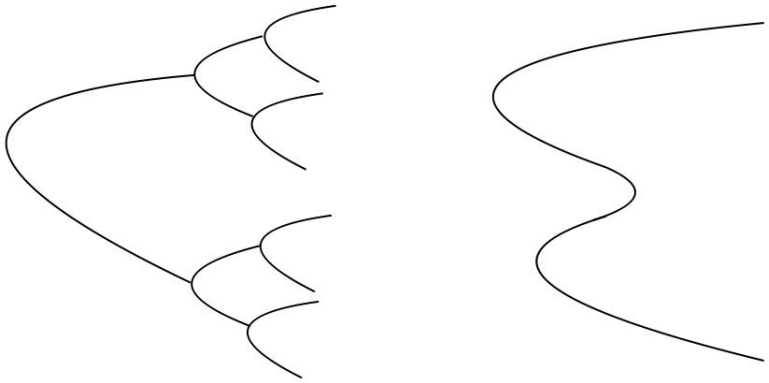

Figure 5.8: The left panel is a bifurcation which we have never observed. The right panel is a "retrograde" which is an alternative way of losing solutions.

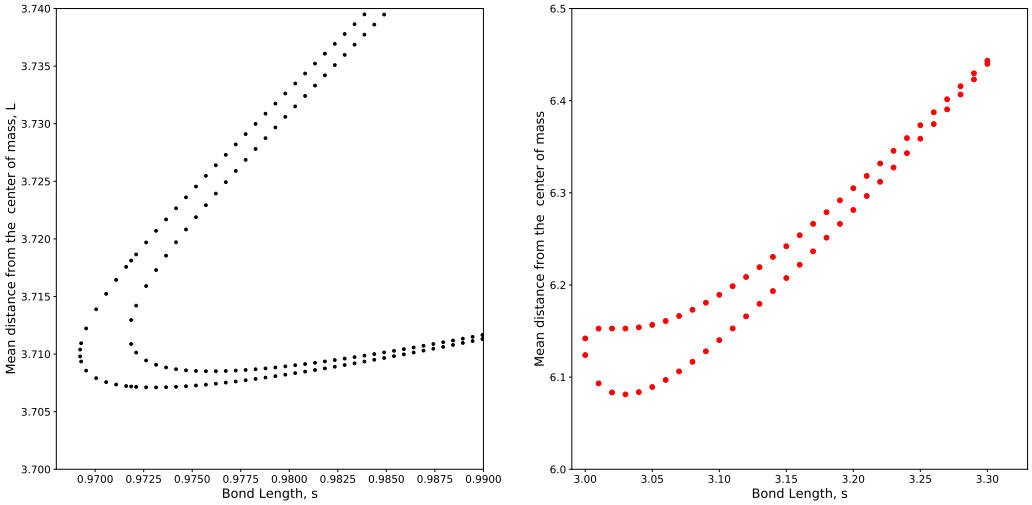

Figure 5.9: (Left) L by varying edge length for the lowest values of edge length; (Right) L by varying edge length for a loop showing how solutions appear and disappear.

5.5 Single Edge-cuts

The discussion in the previous section showed that different realizations of an isostatic network can be found by solving edge length equations. Fig. 5.10 depicts four realizations of Trihex at $s \approx 0.973653$. Their corresponding points are marked by red stars in the left plot. We can think of two paths on this plot as two branches of realizations. The realizations 1 and 4 belong to the initial branch while 2 and 3 lie on the second branch starting at $s \approx 0.972$. The pair of solutions that belong to the same branch indeed have very similar configurations. In fact, the largest difference between the pairs is the reflection of the top connecting edge along horizontal axis. For the pairs that do not belong to the same branch, the motion involves the significant rotation of the bottom triangle. If we would assume that the edges are *harmonic springs* and not fixed-lengths bars, the energy path connecting the pairs on different branches has a much higher energy cost/barrier compared to that of the pairs on the same branch. Note that the whole energy landscape of Trihex at this edge length has only 4 minima. The nice feature of the landscape of Trihex is that the global minimum energy is exactly zero.

This energy perspective makes an important bridge between Trihex examples and glasses. If this picture from studying Trihex remains intact in glasses, we expect to see that solutions play different roles depending on which branch they belong. The Fig. 5.10 is specifically important since the experimental density of glasses is close to the low density edge. So we expect the discussion in this section would somewhat generalize to the 2D glasses. But as discussed, solving edge length equations is computationally expensive for a large system. On the other hand, two-level systems in glasses are rare. To have the slightest hope of finding a tunneling state, we need to study systems that are considerably larger than Trihex. This makes it inevitable

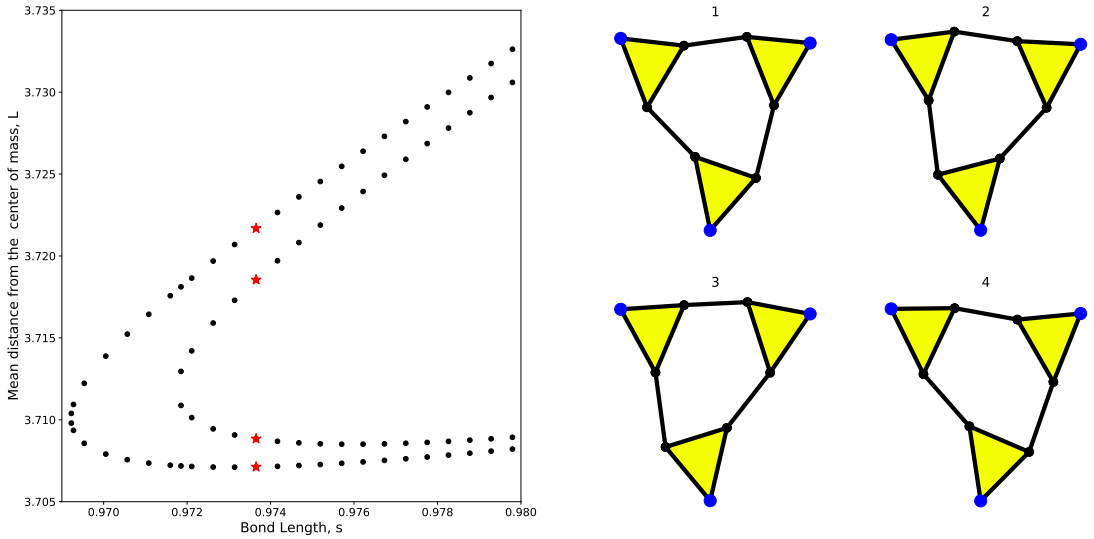

Figure 5.10: The four solutions with the edge length equal to 0.973653 marked with red asterisks. The solutions are numbered from the smallest mean distance from the centroid ($y-$axis) to the largest. The solutions on the same branch show a small displacement but a more significant motion is involved among the solutions from the different branches.

to design an alternative approach to find realizations of a framework starting from already available information.

This approach can be designed using the nature of an isostatic framework which is on the verge of instability. The number of zero eigenvalues of the dynamical matrix of an isostatic framework is exactly equal to the number of trivial motions (or dimension of the null space). Any other motion has a finite cost in energy. But if a single constraint of an isostatic framework is removed, now the null space gains one extra dimension moving along which has zero energy cost. In fact, it can be proven that the traversal along this non-trivial eigenvector is continuous and leads to an even number of realizations since the path is also closed. We state the above observations as a theorem.

Theorem 12. *If a single edge is removed from a finite generic isostatic framework, the resulting mechanism has a configuration space that is a closed, continuous curve,*

on which there are an even number of configurations where the removed edge returns to its original length.

This theorem can be directly written as a step-by-step *single-cut* algorithm [153]:

1. Start from an isostatic network, *i.e.* a rigid network with no redundant edge. The number of trivial motions depend on the imposed boundary conditions. In a system with periodic boundary conditions, only rigid translations are allowed. For anchored boundary condition, no trivial motion exists.

2. Remove an edge from the isostatic network, and form its dynamical matrix. Find the eigenvectors corresponding to zero eigenvalues (the null space). Remove trivial motion eigenvectors to find the one internal degree of freedom.

3. *Eigenvector-following*: Once the non-trivial direction is identified, move all sites along that direction with a small step size. The smaller the step size, the smaller is the error in traversing the circuit, *i.e.* the path that the system takes in high dimensional space. Note that this motion does not change the edge length of any other edge. Also use the dot product of the previous and current directions to make sure we only move forward in the configuration space.

4. Compute the dynamical matrix at the new point and repeat the above process to traverse in the configuration space. Meanwhile monitor the distance between the two vertices that had their connecting edge removed. If we continuously move through this one-dimensional path, we eventually come back to the starting point. Once we are back to the initial point, the sum of distances from the center of mass is plotted against the length of the cut edge, for each point along the path. This gives us a circuit projected in 2D plane in which drawing a vertical line will identify the original point and its conjugate(s) in the configuration

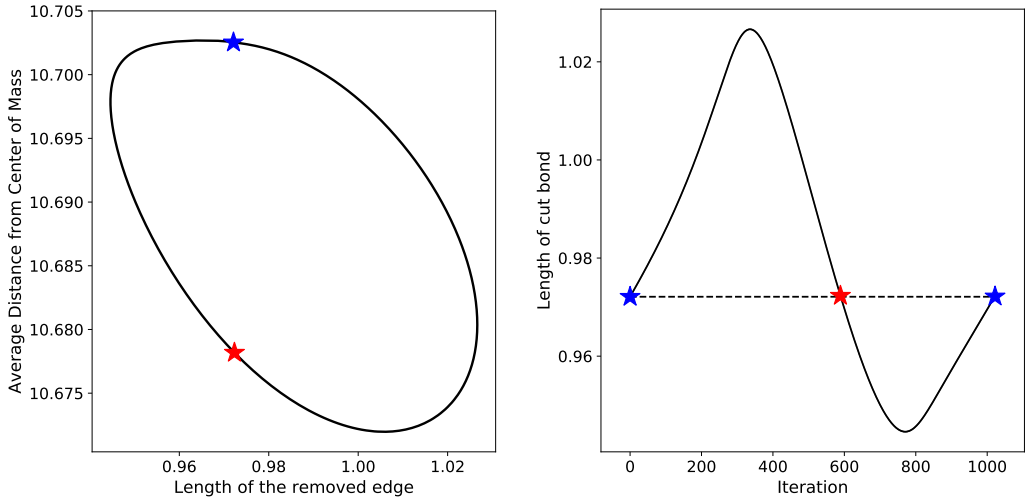

Figure 5.11: (Left) A circuit projected in 2D plane; The vertical axis represents the average distance of all vertices from the center of mass. The horizontal axis shows the distance between two ends of the removed edge. The blue and the red asterisks denote the original and alternative realizations, respectively. A vertical line, drawn at the location of the original bond length, has two intersections with the circuit. (Right) The distance of two ends of the removed edge vs. iteration step by moving along the path. The dashed horizontal line represents the original length. The asterisks correspond to the ones on the left.

space.

Fig. 5.11 shows the result of this algorithm applied to our Trihex example for an edge length about 0.97 which is fairly close to the edge of no solutions. The starting point is shown by a blue asterisk while the conjugate conformation is shown by a red asterisk. The step size is chosen small to traverse a smooth closed path. A vertical line drawn at $s \approx 0.97$ intersects the circuit at two points which correspond to the realizations of the network. The right figure shows the length of the removed edge while moving along the path and how it returns to its original value twice. The first time (red asterisk), we visit a new realization of the network and the second time (blue asterisk) we return to the starting point.

While the circuit of realizations close to the left edge show a fairly simple closed shape, this is not the case for the systems far from this limit. As the edge length

increases, more solutions appear and new branches form. Even some branches can host more than two realizations. Therefore it is expected to have much more complex circuits in which a single edge-cut can lead to more than two solutions. An example of such circuit is shown in Fig. 5.12 for $s \approx 1.43$. Starting from the realization denoted by a red asterisk, a single edge-cut leads to a very complex circuit which passes multiple solutions however not *all* realizations. In this example 10 out of 22 solutions are found using a single-cut. The circuit displays two cusp−like regions on the left side which happens when two edges are approximately co−linear.

The complex circuit showed that not all realizations are accessible through the single cut algorithm. An interesting case study is to start from one of the conformations in Fig. 5.10 and study the possibility of obtaining other three realizations as the system closer to no−solution edge. This is important as the microscopic images of silica bilayers are found near this edge.

Let's start from realization 1 and remove all edges in turn and find (at least a) second realization. Fig. 5.13 shows the results. We observe that independent of the removed edge, the circuit only passes through conformations 1 and 4 which belong to the same branch. This is despite the fact that the system obviously traversed different paths with respect to the cut edge. It seems that these realizations do not have any access to the neighboring branch. In fact, we can make the same statement when we start from the solution 2 or 3. We would never visit solutions 1 or 4 by removing a single bond which are located on a different branch (Fig. 5.14). This means that the above algorithm is not a perfect alternative to the edge length equations as it only finds some solutions in the space of all available conformations.

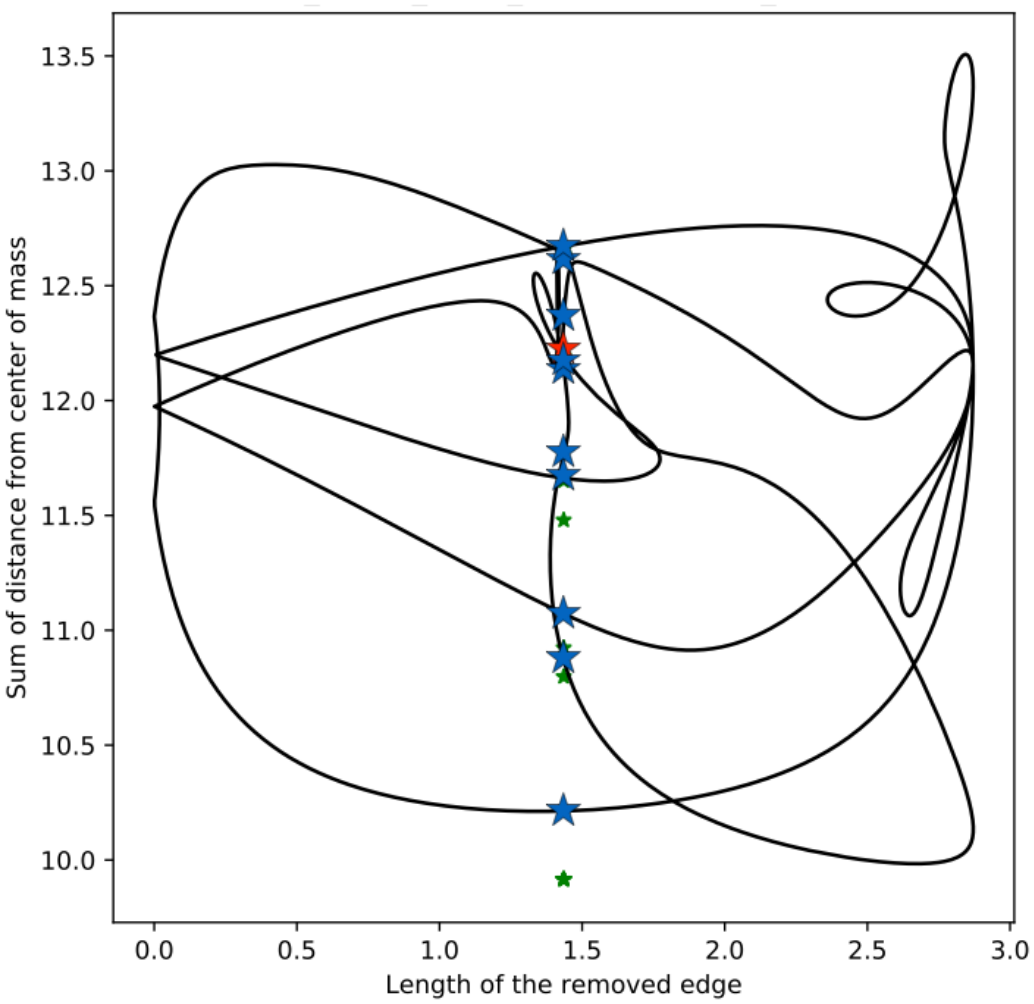

Figure 5.12: The vertical axis represents the total distance of all vertices from the center of mass while the horizontal axis shows the distance between two ends of the removed edge. The total number of solutions at this edge length are 22 but the circuit passes through 10 of solutions which are shown by blue asterisks. The starting realization is marked by a red asterisk. Other solutions are shown by green asterisks. Note that multiple solutions can be overlapped on this scale as the value on $y-$axis is not sensitive to approximate symmetries in the system.

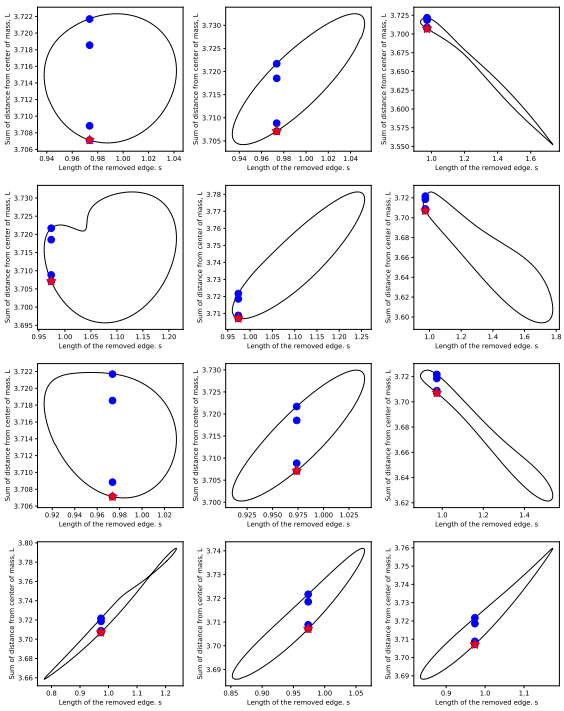

Figure 5.13: Circuits formed by starting from conformation 1 in Fig. 5.10. Each figure corresponds to the removal of a different edge.

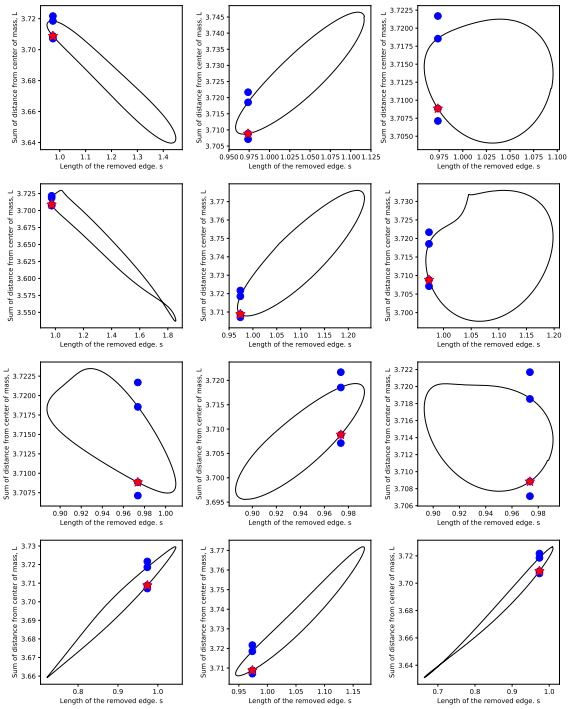

Figure 5.14: Circuits formed by starting from conformation 2 in Fig. 5.10. Each figure corresponds to the removal of a different edge.

To make the connection between various conformations of an isostatic framework and tunneling states, we need to find the energy path between two realizations. When during circuit traversal an edge is cut, the energy cost is zero but this is just a convenient method to find the second solution. To find the energy barrier we add back the removed edge assuming that all edges are harmonic springs with the force constant $k = 1$. To find the exact form of the energy landscape, we should find the transition path with the minimal energy path between the two energy minima which can be achieved by methods such as Nudge Elastic Band [154]. However, we could find a first estimate of this path using the linear interpolation. Let $\mathbf{s}_1$ and $\mathbf{s}_2$ be $2N-$dimensional vectors containing the coordinates of two given realizations with zero energy. We define the following linear interpolation between the states:

$$\mathbf{s}(\Lambda) = \mathbf{s}_1 + (\Lambda + \frac{1}{2})(\mathbf{s}_2 - \mathbf{s}_1). \tag{5.11}$$

Therefore, the energy can be found as a function of Λ, where $\Lambda = -\frac{1}{2}, \frac{1}{2}$ correspond to $\mathbf{s}_1$ and $\mathbf{s}_2$, respectively. With this formulation the midpoint between two conformations is located at $\Lambda = 0$. Using the four solutions in Fig. 5.10, the energy pathways between all possible conformations are given in Fig. 5.15. We find that the energy barrier for the states on the same branch is much lower ($\sim 10^2$ times) than the ones on different branches. This reaffirms what we observed before: solutions on a branch are separated from solutions on the other branch by a high energy barrier. It seems that to make this transition possible through the concept of removing constraints, more complex schemes than single-cut are required. However, our efforts to employ more complex procedures provided no additional solutions compared to the ones found by the single-cut algorithm. For example, the single edge cut can be modified to cutting two edges while a new third edge is added. Or we can remove two edges and explore a two-dimensional surface as opposed to a one-dimensional closed

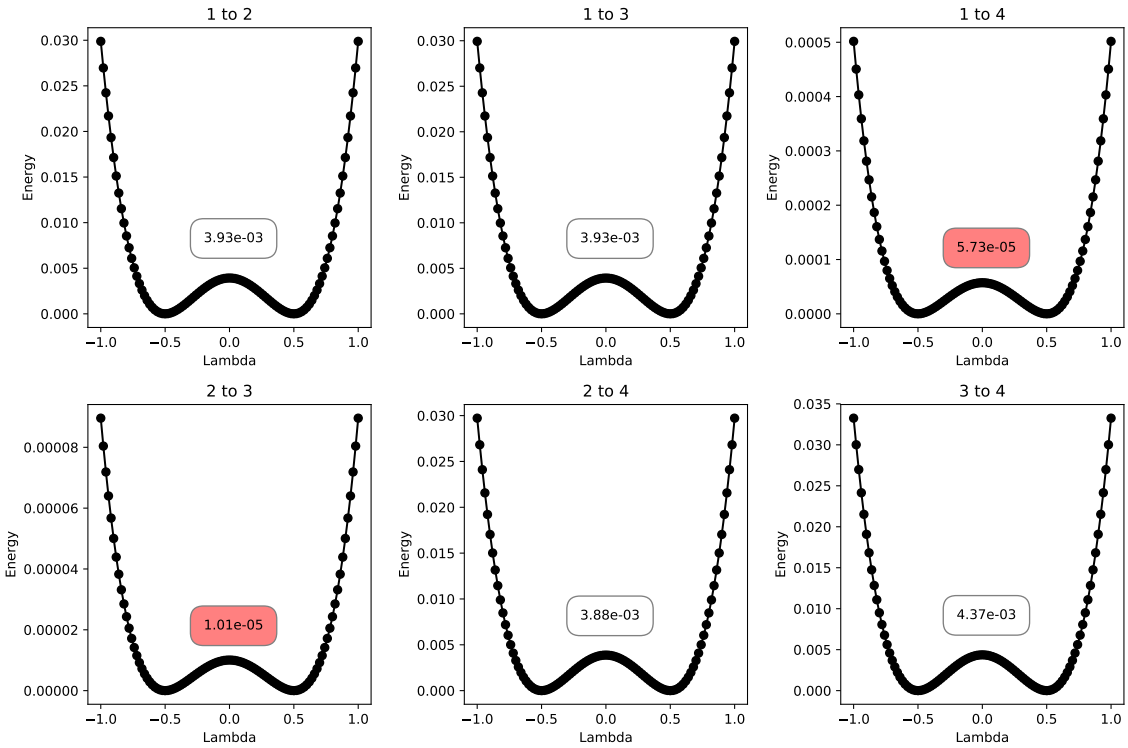

Figure 5.15: Energy barrier between any two conformations in Fig. 5.10 calculated based on the linear interpolation versus the interpolation parameter Λ. The starting realization sits on $\Lambda = -0.5$ and the final realization is located at $\Lambda = 0.5$. The barrier height for the solutions on the same branch is significantly less than the barrier height for the solutions on different branch.

path in the case of cutting an edge. Albeit, there is no guarantee that this surface is continuous or close. None of such methods yielded additional solutions.

5.6 Alternative Realizations of 2D Glass

Trihex, as a toy model, displayed the main features of the realizations and the existence of branches of solutions but we would like to apply these ideas to 2D glasses and link the existence of the tunneling modes to the multiple realizations of a glass structure. 2D glasses are a network of corner-sharing triangles where every vertex is four-fold coordinated. Since each vertex has two degrees of freedom, this network is locally isostatic [48]. But boundary conditions determine the global rigidity of

the framework. For pinned boundary conditions [48] which is useful for networks extracted from the experimental data, the system is at the isostatic point. For the case of periodic boundary conditions, the system contains two redundant bonds which must be removed.

However, 2D glasses are systems much larger than the Trihex and computational limitations must be considered. Solving the set of edge length equations is practically impossible for systems as large as 2D glasses. Therefore, we would not have access to the complete picture of branches and how the solutions evolve on a branch. The single-cut algorithm is guaranteed to provide new realization(s) but is not an exhaustive method and some of the existing solutions will be unreachable by the single-cut algorithm.

To find the alternative relations of a 2D glass structure using single-cut algorithm, the null space (the eigenvectors with zero eigenvalue) of the dynamical matrix $\mathcal{D}$ should be found by diagonalizing this $2N \times 2N$ matrix which for large N is expensive. Numerical experiments show that we are limited to systems with $N \approx 5000$. As the system size becomes larger, there is an additional source of error due to the moving of all particles along the non-trivial zero-mode. Therefore, it is necessary to displace the particles in smaller steps to ensure that the traversed path is smooth. By moving in this high dimensional space, the error is built up which causes the path to be not closed due to the numerical error. If this error is to be removed, we should either choose an extremely small step size or have frequent energy minimization, both of which are expensive.

We apply a slightly modified version of the single-cut algorithm to 2D glasses to avoid the mentioned bottlenecks. Since the existence of the second solution is guaranteed, and only the alternative realization is required to calculate the thermal properties, fairly large steps can be taken along the path with no need to complete the

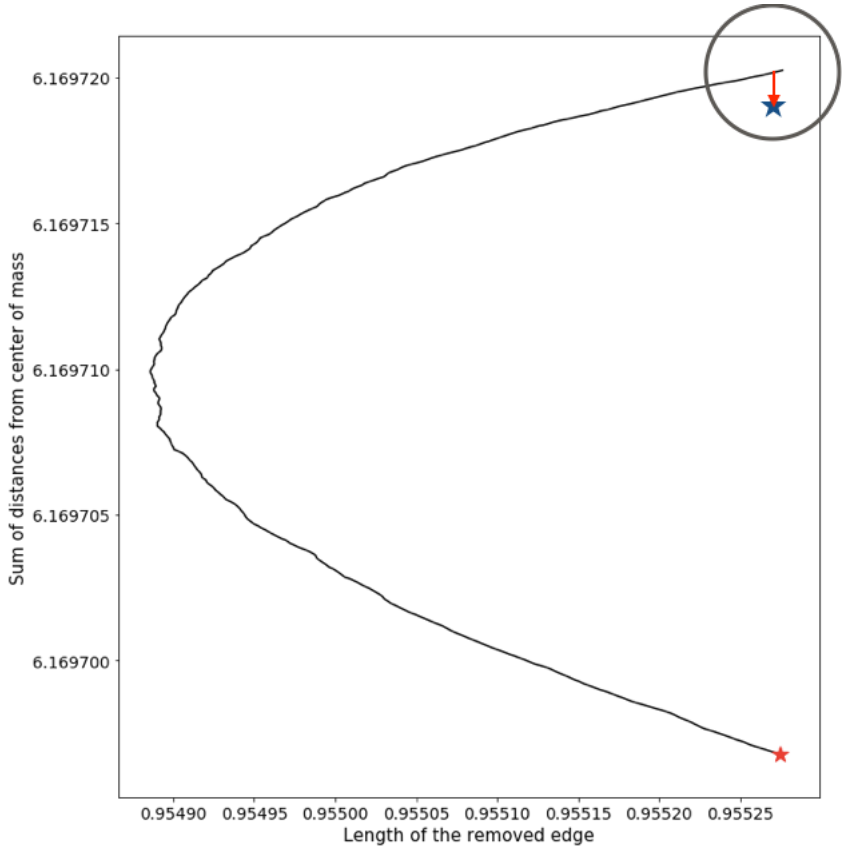

Figure 5.16: The circuit found by applying the modified single-cut algorithm to a 2D glass, in which the path traversal is stopped upon finding a solution. Fairly large steps are taken along the eigenvector with zero eigenvalue as is evident from roughness of the circuit. The black circle is drawn to emphasize the fact that the real solution (indicated by the blue asterisk) with no error in the edge lengths does not exactly lie on the drawn circuit and further energy minimization is required to find the correct coordinates. The red asterisk denotes the original network. The vertical axis represents the total distance of all vertices from the center of mass while the horizontal axis shows the distance between two ends of the removed edge.

circuit exactly. In this adopted algorithm, once the circuit intersects the vertical line denoting the original length of the cut edge, we have found a second realization and the path traversal can be stopped. However, the position of vertices and subsequently the edge lengths have some error which can be refined by the energy minimization to ensure that edge lengths are equal to their original values (Fig. 5.16).

If the circuit is complex enough, it contains more than two realizations. Based on the modified scheme, if the circuit traversal is stopped after finding the first solution,

we might miss a whole set of solutions. The concern can be elevated by noting that glasses are usually found at the extreme of density (edge of the flexibility window). At this limit, we expect to have only two solutions from the discussions in Trihex example. But we also tested this idea by applying the original single-cut algorithm on two 2D networks ($N = 48, 300$) by removing all edges iteratively. It was observed that all circuits give two and only two distinct solutions independent of the removed bond.

The networks of 2D glasses are prepared using WWW algorithm (see Chapter 1) with the periodic boundary conditions while ensuring that the ring distribution and the area of polygons are in agreement with the experimental data. This leads to structures where the edge lengths are no longer exactly equal. Therefore 2D glasses satisfy a stronger definition of being generic. We assume that the structure is in mechanical equilibrium, all edges are harmonic springs at their rest lengths and the dynamical matrix is positive semi-definite.

At this point, two realizations of a 2D glass are available; one is the original network (prepared either experimentally or computationally) and one is the result of the modified single-cut algorithm. They have the same exact topology and bond lengths, but the vertices are displaced between the two states.

From energy considerations of tunneling in glasses, it is expected that motion of atoms in a tunneling mode are relatively localized since the displacement of a large group of atoms extended over a long distance requires a massive energy which is not available at temperatures about 1 K. The Participation Ratio (PR) is a common measure of how localized a state is. If atom i is displaced by the vector $\mathbf{u}_i$ between two conformations, PR is defined as:

$$\mathrm{PR} = \frac{\left(\sum_{i=1}^{N} |\mathbf{u}_i|^2\right)^2}{\sum_{i=1}^{N} |\mathbf{u}_i|^4}. \tag{5.12}$$

For a perfectly delocalized mode $|\mathbf{u}_i| \sim 1/\sqrt{N}$ and PR $\sim N$. For a completely localized mode $|\mathbf{u}_i| \sim \delta_{ij}$, then PR ~ 1. Hence, a small value of PR is the signature of a localized mode. Since it is expected that tunneling modes are localized modes, we expect that by increasing the system size N, the fraction of atoms participating in the mode, namely PR/N, decreases.

The other important aspect is the significance of the atomic displacements in the limit of large systems. If any mode is to be considered a tunneling state, the atoms should be displaced significantly more than their zero-point motion. Assuming a harmonic oscillator, the zero-point amplitude x_0 is of order of:

$$x_0 \sim \sqrt{\frac{\hbar}{m\omega}} = \sqrt{\frac{10^{-34}}{10^{-26} \times 10^{14}}} = 10^{-11}\text{m} = 0.1\,\text{Å}, \tag{5.13}$$

using the order of the mass of an oxygen atom. For an O$-$O bond length of 2.6Å, $x_0 \approx 10^{-2}$ in the unit of the bond length. If the typical motion of the atoms measured by their mean displacement $\sum |u_i|/N$ is less than x_0, such motions are not physically important for the tunneling states however are mathematically correct.

We prepare four networks of corner-sharing triangles under periodic boundary conditions with varying size $N = 48, 300, 1254, 5016$ and randomly remove two edges to satisfy the isostaticity condition. By applying the modified single-edge cut algorithm, the conjugate solutions are found. The different size of the systems allows to study the behavior of the participation ratio and the mean displacement of vertices as a function of N.

Table 5.1 summarizes the results for the mean displacement of atoms and the participation ratio for various systems. By increasing the number of particles, the total displacement $\sum |u_i|$ increases slightly but the average displacement of a typical particle $\sum |u_i|/N$ decreases. In fact, regardless of the system size, this average displacement is smaller than of the zero-point motion x_0 and hence this motions cannot

Table 5.1: Motion magnitude in the unit of the edge length found in simulations for different system size, N.

N	$\sum \lvert u_i \rvert$	$\sum \lvert u_i \rvert / N$	$\sqrt{\sum \lvert u_i \rvert^2 / N}$	PR	PR/N
48	0.09	1.89×10^{-3}	2.12×10^{-3}	21	0.44
300	1.47	4.89×10^{-3}	5.80×10^{-3}	123	0.41
1254	2.03	1.62×10^{-3}	1.84×10^{-3}	595	0.47
5016	2.94	0.59×10^{-3}	0.67×10^{-3}	2283	0.46

be representative of a tunneling state. In addition, all systems exhibit modes that contain $\sim 45\%$ of all vertices in the system. Such an extended mode cannot be a tunneling state since in the limit of Avogadro number of atoms, a massive number of atoms should be involved in such states which is not energetically favorable. Unfortunately, it seems that the single-cut algorithm is not able to find realizations that are sufficiently distant from the initial realizations (evidenced by vanishingly small $|u_i|$ values) and sufficiently localized (evidenced by the constant PR/N value). Although the found modes exist they cannot account for the tunneling states in glass since at very large N the conformations are effectively degenerate.

In order to gain some insights into the thermal properties of the found states, a double-well potential can be formed by the pair of realizations for each system size. For every N, the energy pathway is found by the linear interpolation (Eq. 5.11). Then the numerical value of the energy barrier V_b is extracted from the interpolated curve. The well separation d is calculated as the root-mean-square deviation (RMSD) of atomic positions. The probability of the tunneling scales as $e^{-\lambda}$ (Appendix B) where λ is the tunneling parameter defined by the following equation (derived from ratio of

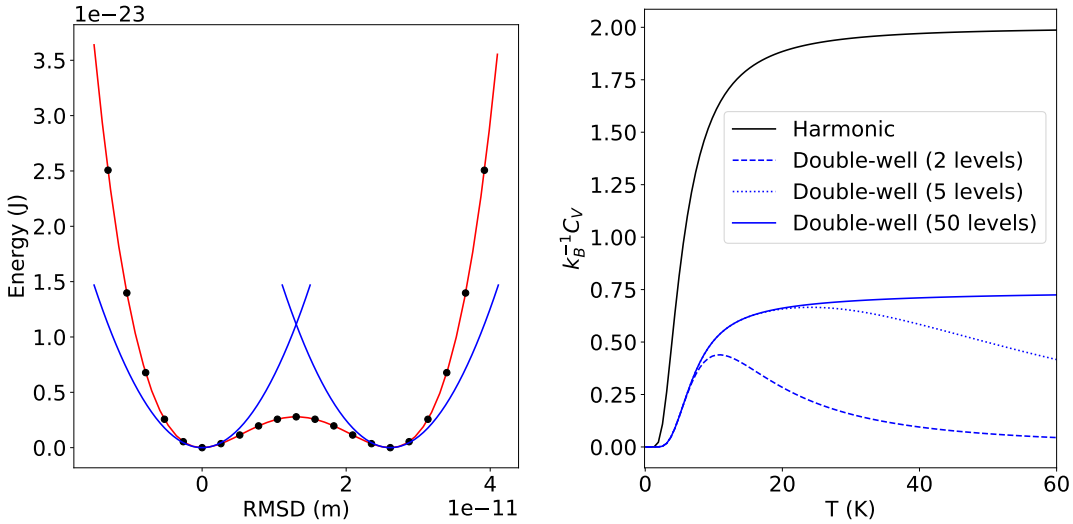

Figure 5.17: (Left) The double well potential found by linear interpolation between the found states for $N = 300$; The energy vs. separation between two realizations. The black circles are found by linear interpolation, the red line is a fourth-order polynomial fit to the data. The blue curves show the harmonic approximations; (Right) The heat capacity of two harmonic wells (black) and the heat capacity from double well potential, for different numbers of energy levels included (blue).

kinetic and potential energies):

$$\lambda = d\sqrt{\frac{2mV_b}{\hbar^2}}, \tag{5.14}$$

where m is the mass of an oxygen atom. For a detailed discussion of the significance of the tunneling parameter, see Appendix B.

Fig. 5.17 (the left panel) shows an example of a double-well potential derived from the system with $N = 300$ atoms. The black points are found using Eq. 5.11 while the red line is a 4th-order polynomial fit of Eq. B.1 to these points. The two blue lines are the harmonic approximations around two equilibrium realizations. For $N = 300$, we have $V_b = 2.79 \times 10^{-24}$ J and $d = 0.3$Å which corresponds to a small value of $\lambda = 0.1$. The energy levels of this double-well potential can be found by solving the Schrodinger equation numerically (see Appenix C). After finding the energy levels, the specific heat of this double-well potential can be found, shown in the right panel of Fig. 5.17. The black curve represents the specific heat of two harmonic oscillators.

Table 5.2: Characteristics values of double-well potentials in SI, found in simulations for four different system size, N.

N	V_b(J)	T_b(K)	d(Å)	λ	$T_{\max}(K)$
48	9.45×10^{-27}	6.84×10^{-4}	0.04	0.0012	16
300	2.79×10^{-24}	2×10^{-1}	0.30	0.10	12
1254	1.44×10^{-25}	1.04×10^{-2}	0.17	0.02	5
5016	3.84×10^{-27}	2.78×10^{-4}	0.12	0.0025	23

Note that the black curve saturates at $C_v = 2k_B$ as expected from the equipartition theorem. The blue lines are the specific heat of the double-well potential when only up to a certain energy level are included in the calculations. In particular, the dashed blue line is the specific heat due to the first two energy levels while the maximum specific heat happens at the temperature $T_{\max}$ which is about 16 K for the above example with $N = 300$. As is evident, even by including 50 of first energy levels the specific heat is less than half that of harmonic oscillators.

Table 5.2 summarizes the characteristics of the double-well potential for four systems in SI units. The barrier height (V_b) of all systems is a very small value which means that the double-well is essentially flat in the middle. The well separation d is also very small and at most about 5% of O−O bond length and λ shows a somewhat monotonic decrease with the system size[4]. $T_{\max}$ which characterizes the temperature at which the specific heat of a two-level system is maximum, happens to be at about ~ 10 K, much higher than the range of temperatures concerning the tunneling states.

To draw a comparison between Trihex and 2D glasses, it seems that the single-cut algorithm can only find solutions that belong to the same branch while realizations

[4]To find the exact dependence of the values on N more samples should be used.

on other branches are energetically inaccessible since they contain motions of larger units such as a rigid triangle (or tetrahedron). Although, we think such branches exist in glasses, it is not computationally feasible to find the branches for such large systems similar to Trihex.

It is worth noting that the above discussion can be directly applied to bulk glasses. We repeated the modified single edge cut algorithm for various silica structures in three dimensions. The only modification required in 3D is that three edges need to be removed to reach the isostatic point. Our results for bulk (3D) glasses were very similar to the two-dimensional case.

5.7 Discussion

It is experimentally shown that glasses exhibit a larger specific heat compared to crystals at very low temperature where implies a larger density of states of low frequency modes. Theoretically, it is postulated that this is due to the tunneling states in glass at very low-temperature. Based on this model, atoms in glass have access to multiple local energy minima and quantum tunneling between two configurations is responsible for the observed linear specific heat.

Glasses such as SiO_2 are at the isostatic point, meaning that degrees of freedom are exactly balanced by the central force constraints. Guided by Theorem 11 which states an isostatic framework has to have an even number of realizations, we applied a single-cut algorithm to find multiple realizations of the framework. The algorithm is based on removing a single constraint in the system which leads to a single degree of freedom. By following this floppy mode, some alternative realizations of the systems are found. These conformations have the same connectivity and the same set of edge lengths as the starting structure but the vertices are displaced with respect to the original structure.

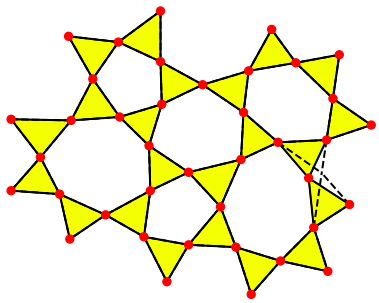

Figure 5.18: A bowtie motif which was proposed to explain the tunneling states in glasses.

By applying this algorithm to the networks of corner-sharing triangles as models of 2D glasses, we found conjugate realizations for several frameworks varying in size. Our algorithm provides only one other realization and this number does not scale with the system size. We estimated the localization and the atomic displacements between the found states and showed that by increasing the system size, the found modes are extended while the atomic displacements become vanishingly small. Also, the thermal properties of such modes were studied as double-well potentials and it was shown the barrier height is very smaller than expected for the tunneling states. Hence, the modes resulted from the single-edge-cut cannot explain the low-temperature anomalous behavior of the specific heat of glasses.

Since this algorithm did not provide modes that describe the expected tunneling states, alternative methods were designed. One approach was to make more complex schemes similar to single cut. For examples, instead of taking out one constraint, two edges were removed. Because now the system has two non-trivial modes, a surface can be explored. This method did not provide any additional solution to the single-cut and, moreover, Theorem 11 does not generalize to surfaces.

A second approach was to activate tunneling modes through local distortions. For examples, consider two triangles with a shared corner which we refer to as a *bowtie*.

Now draw two imaginary lines from the centroids of triangles to the shared corner. The angle between these imaginary lines is smaller than 180° which is dictated by the ring closure in glasses. Now one could imagine that this angle can be flipped through the straight line connecting two centroids (see Fig. 5.18). Historically, such motifs are imagined as a possible mechanism for two-level systems in glasses [155, 156]. Our experiments show that such a perturbation cannot account for the tunneling states as they either lead to an extended state or the system simply returns to its original state after energy minimization.

All the methods mentioned here led to extended states. The reason behind such extendedness can be attributed to the marginality of the network of corner-sharing triangles. Once the system is *globally* isostatic (i.e. two edges are removed from the fully connected framework) (Fig. 5.19, Top), removing a single edge brings the framework to isostatic-minus-one state where in our network all vertices are *hinges* (Fig. 5.19, Bottom). A hinge is a vertex that belongs to more than one rigid cluster. The smallest rigid clusters in our 2D glassy networks are triangles and these triangles can freely hinge about their common vertex. It seems natural that driving the framework along the non-trivial zero-energy mode would cause all vertices to move. It is also conjectured that to have a localized tunneling state at isostatic-minus-one, localized hinges are indeed necessary. This would ensure that the motion of vertices is confined within the region with hinges. Fig. 5.19 shows the results of applying the pebble game algorithm [101] on the network of corner sharing triangles. The top panel demonstrates the system at isostatic point when two edges are removed. Removing another edge makes every vertex a hinge (shown by green) in the bottom figure [157]. Since corner-sharing triangles are always very close to the marginal point, it seems extremely difficult to design any localized state using purely central forces. However, some initial experiments have shown that localized motions can be designed

in frameworks that are far above isostatic point [157]. Hence, it might be possible to use additional forces (constraints) such as angular forces to achieve localized states.

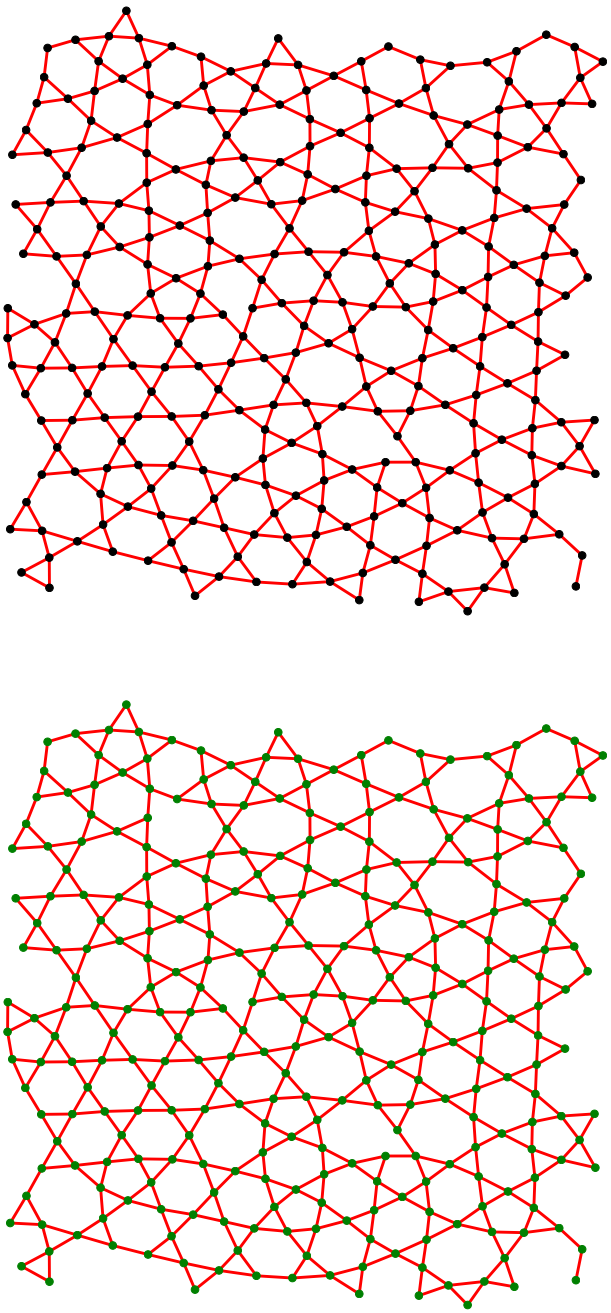

Figure 5.19: (Top) A network of corner-sharing triangles with periodic boundary conditions at isostatic point where two edges are removed. (Bottom) Once an edge is removed from the top network, all vertices are hinges (shown by green points).

Although, our efforts did not lead to a definite characterization of tunneling states in glasses, it uncovered some previously unknown aspects of such structures. We showed that glassy networks have multiple realizations due to their rigidity properties and proposed a method to find those realizations. However, the type of realizations accessible through the single-cut algorithm are not physically significant as they have motions smaller than the zero-point motion of atoms. We also used Trihex to fully characterize the nature of realizations and showed that solutions can be found on multiple branches. The conformations on a branch are accessible though the single cut algorithm but this method could not yield any solution from other branches. Unfortunately, it is not practical to find branches in 2D glasses by the methods used in Trihex example since a set of highly coupled non-linear equations should be solved.

Chapter 6

CONCLUSION

The structure of glasses have been subject of many studies and there is a good agreement between the models and the experimental data. In recent years, a bilayer of silica glass is imaged and has added to the available information from glasses. The images of silica glass reveal an amorphous structure in which the atomic arrangement resembles the continuous random network model which was developed nearly 80 years ago. They show that atoms in silica glass have an arrangement similar to the crystalline structure at very short-range distances, but somewhat random bonding between structural units (SiO_4 tetrahedrons) creates a network that lacks the long-range order.

In Chapter 2, we have used computational models of silica bilayers to investigate order at short-, intermediate- and long-range. The computational models are prepared such that they have a ring distribution similar to the imaged glasses. But their larger size allowed us to measure correlations in much longer distances with better statistics. We presented two distance definitions, namely topological distance and geometrical distance to quantify the range of correlations. The topological distance is a discrete measure counting the number of intervening rings between two given rings. The geometrical distance is the continuous Euclidean distance of two rings where they are replaced by their centroids. Aboav-Weaire law characterizes the tendency of large and small rings to be adjacent. We generalized this law for both distance definitions and showed that the medium-range ordering exists between rings that are about three rings apart. Beyond this distance, the ring correlation quickly fades away. However, the topological distance results in a pseudo-long-range effect because the rings located

at a distance form a non-circular shell. We were successful at relating the strength of correlations to the ring size. It was shown that pentagons and heptagons are strongly correlated with their neighbors while hexagons have weaker correlations with their adjacent rings.

While the computational models have been successful at reproducing the geometrical and topological properties of 2D glasses, there are still some discrepancies between models and experiments. The imaged glassy structures show remarkable symmetric rings which have almost maximum area (closed to being regular polygons) while the employed computational models here should be improved in this respect. In addition, there is some discrepancy between ring arrangements measured by the larger value of Aboav-Weaire parameter for the experimental samples. This possibly requires additional energy terms in the Hamiltonian which are topological in nature and can favor experimentally observed ring arrangements. To this end, new correlation measures should be defined to characterize much more complex correlations between triplet, quadruplet, etc of rings. This is a fruitful future direction to make models closer to nature, to uncover possibly unknown orderings in glass, and finally to remove doubts about the meaning of Aboav-Weaire parameter.

Although the ring structures of bilayers of silica are directly evident from images, their geometrical properties depend on the accurate atomic coordinates. As experimental data have an uncertainty in the position of atoms and their size is finite, structural refinement is necessary to locate the exact position of atoms which in turn leads to restoring the correct bond lengths and bond angles. To accomplish the refinement, a number of issues need to be resolved.

Firstly, silica is a locally isostatic network with marginal mechanical stability and the imposed boundary conditions can greatly influence its mechanical response. We designed two types of boundary conditions for such finite networks to render

the structure effectively isostatic so atoms in the bulk behave as if they belong to an infinite structure. These boundary conditions are discussed in Chapter 3. The first design is a slider boundary condition in which the surface atoms can only move tangent to a one-dimensional slider connecting all the surface atoms. With sliding boundary conditions, a network of corner-sharing triangles is isostatic but for a silica bilayer, additional constraints are necessary. Nevertheless, this boundary condition has the plausible feature that all boundary atoms are involved. The anchored (pinned) boundary condition is the second design in which half of the surface atoms are immobilized. This scheme renders the network isostatic in 2D and 3D and two pinning arrangements are possible for each network.

Secondly, the experimental samples contain unimaged regions varying in size. In order to include the maximum information in our refinement procedure, we preprocessed the experimental networks by reconstructing regions of the network which were not imaged or contained missing atoms (Chapter 4), *if* possible. As rings in the bilayer are very close to being regular, we used angles between bonds to guess the location of missing atoms. Once the network was reconstructed as much as possible, we employed various interactions between atoms to refine structure so bonds have the proper length.

After imposing the proper boundary conditions and reconstructing the network as much as possible, the experimental samples can be refined as explained in Chapter 4. Numerous force fields are proposed for the bulk silica. In the present work, we employed three types of potentials to include the known chemistry such as proper bond lengths in the refinement procedure. In the simplest case, the O-O bonds were treated as harmonic springs which is justified by the fact that tetrahedrons in silica are rigid. We also used PIM potential which in addition to harmonic terms includes polarizability of the atoms in a molecular dynamics setting. The most complex simulations

were carried out using DFT to benchmark the simpler interactions.

Si-O-Si bond angle in the bulk silica is a well-studied structural property and contains information on the linking of the rigid tetrahedrons to form the glassy network. In the bilayers of silica, Si-O-Si bond angle has a greater importance as it reveals both in-plane and out-of-plane structural information. In the bulk silica, Si-O-Si angles exhibit a very broad unimodal distribution with a peak at $\sim 145^\circ$. In contrast, all three potentials in the bilayer of silica result in a bimodal distribution of Si-O-Si angles.

The lower peak corresponds to the in-plane Si-O-Si angles and occurs at $\theta \sim 140 - 142^\circ$ for various potentials which is consistent with the values in the bulk silica. However, a second peak occurs at $\sim 175^\circ$ which is due to the out-of-plane angles (bridging O atoms) and absent in the bulk silica. In initial experimental studies, it was assumed that this bridging angle is fixed at 180° but we have conclusively shown that this angle is less than 180° and the mid-layer is tilted. This result is remarkable as we also showed that the symmetry plane of the bilayer is maintained despite this tilt and regardless of simulation and boundary details; an amazing emergent phenomenon in a system which is the epitome of disorder.

This study provided some preliminary results about the bilayers of silica and many more questions are yet to be answered. As more experimental samples, possibly with larger size, will be synthesized the information about the their ring structure can be included in the simulation to create models in better agreement with the experiments. The existence of the so-called flexibility window in 2D, and its similarity to and differences from 3D zeolites is also of interest. For examples, it is shown that the range of the flexibility window is determined by the density and synthesized zeolites lie at the low-density edge of the window. Our preliminary results confirm the existence of such window in the silica bilayers and indeed experimental samples lie close to the

low-density edge of the window. However, more work needs to be done to completely characterize the nature of solutions in the window, and the mechanisms that limit the extent of the window. Another open problem is whether the Si-O-Si tilt exists in the crystalline bilayer which has several polymorphs.

Additionally, our work on the structural refinement of glasses can be seen as a first step. Similar techniques have been used in the refinement of protein structures where the inclusion of known local chemistry produces the best possible structures. So far in glasses only 2D images of silica glasses are available. However, it is expected that in the near future the confocal microscopy techniques can provide images of glasses in 3D and surely more amorphous structures will be imaged in 2D. The structural refinement techniques presented here can be adopted to improve the quality of the available experimental data in such use cases.

Although the focus of the present dissertation was to maximize the available structural information of silica bilayers, we also explored the low-temperature physics of glasses in Chapter 5. Glasses at low-temperature regime show a range of properties which have been a subject of active research since 1970's. For example, it is well-known that the specific heat of glass at temperatures below 1 K shows a linear term in temperature in addition to Debye's cubic term. Although the two-level states can explain this dependency, the real mechanism behind such tunneling states is still an open problem. Here, we explored the possibility of finding such tunneling states in the imaged bilayers of silica. Any hint as to where a tunneling state occurs and its geometrical signatures are of fundamental interest.

The problem of tunneling states can be rigorously formulated in the context of the rigidity theory. The silica glass is a graph and two-level systems are in fact different drawings or realizations of the same underlying connectivity. The thread to connect these two concepts is a theorem which asserts any *generic* isostatic network

has an even number of realizations. The bilayers of silica are isostatic frameworks therefore there are at least two ways to create configurations which satisfy the same given topology (connectivity of atoms and bond lengths). Note that genericity is an important assumption since existence of symmetry can introduce new degrees of freedom and as a result, the network is no longer isostatic. This theorem implies that for any silica bilayer configuration observed in experiments, we can connect the same atoms but place them at new positions while preserving all topological constraints and bond lengths. We used this theorem and proposed a method to find at least one other realization for a given conformation. The method, termed the single-cut algorithm, is based on the removing a constraint from a network at the isostatic state. As a result, a single degree of freedom appears. The theorem guarantees that by following this non-trivial floppy mode, the framework covers a one-dimensional continuous path and finally returns to its starting point. Along this path, at least one other realization is visited.

First, we applied this algorithm to a toy-model, Trihex, to form a complete picture of number of realizations, and study the impact of density on realizations. This was in particular useful since we had independently found all realizations of Trihex. We showed that solutions appear in pairs but by approaching the low-density limit, two solutions are increasingly degenerate. We also introduced the concept of branches for realizations and also categorized solutions based on the branch they belong to. It was observed that single-cut algorithm can only yield solutions that belong to the same branch.

Then, we applied this algorithm to the two-dimensional representation of silica bilayers which are a network of corner-sharing triangles. We showed that this algorithm would only give one other alternative realization of the network. This was similar to the Trihex example when the density is close the extreme point. As we know, sil-

icates do indeed exist close to this low-density edge. The original and alternative realizations were used to create a double-well energy landscape which was later used to study the resulting specific heat. We observed that by increasing the system size, the displacement between two realizations decreases. This means that for a finite but large system size, the displacement will be smaller than zero-point motion of atoms. The modes are also extended where about 45% of all atoms participate in the mode. It was shown that such modes have contributions near temperatures of ~ 10 K while tunneling states are expected to be effective for temperatures below 1 K.

What we observed in the process of finding tunneling models is an excellent indication of "more is different" [158] concept. Large systems in nature behave in ways that are not necessary a sum of their components due to symmetry breaking. This is evident in going from a small system like Trihex to more complex structures such as 2D model glasses. Although, our results to find tunneling states are null, the method can be seen as an initial step to shed light on various features of transitions in glasses.

One future direction is to remove the required constraint not through the removing a bond but other ways such as a change in volume. A network of corner-sharing triangles with periodic boundary conditions is rigid but has d redundant bonds. This means that before cutting the single constraint, d bonds should be removed to make the network isostatic. This appears to be somewhat unfavorable, as it alters the nature of the original network and this removal does not correspond to a physical process. We can use the lattice vectors in the periodic cell as dynamical variables to let the volume change. In d dimensions, there are d lattice vectors, equivalent of d^2 dynamical variables. If we allow $d+1$ of them to change (fixing d^2-d-1) the network is effectively isostatic-minus-one and there is one non-trivial zero mode in the system. This degree of freedom can be seen as the volume/density change which possibly can unify the problem of graph realizations and the flexibility window problems. But it

might be necessary to find more complex schemes so that the alternative realizations can be found from other branches. Since the energy barrier between such states is higher, more drastic changes to the network connectivity are expected.

The microscopic images of silica bilayers and advances in the modeling have expanded our knowledge of amorphous structures in recent years and future advancements will continue to explain their physics and properties.

[1] A C Wright and M F Thorpe. Eighty years of random networks. *physica status solidi (b)*, 250(5):931–936, 2013. doi: 10.1002/pssb.201248500.

[2] B E Warren. X-ray determination of the structure of glass. *Journal of the American Ceramic Society*, 75(1):5–10, 1934. doi: 10.1111/j.1151-2916.1992.tb05432.x.

[3] Thibault Charpentier, Peter Kroll, and Francesco Mauri. First-principles nuclear magnetic resonance structural analysis of vitreous silica. *The Journal of Physical Chemistry C*, 113(18):7917–7929, 2009. doi: 10.1021/jp900297r.

[4] Pinshane Y Huang, Simon Kurasch, Anchal Srivastava, Viera Skakalova, Jani Kotakoski, Arkady V Krasheninnikov, Robert Hovden, Qingyun Mao, Jannik C Meyer, Jurgen Smet, et al. Direct imaging of a two-dimensional silica glass on graphene. *Nano letters*, 12(2):1081–1086, 2012. doi: 10.1021/nl204423x.

[5] DA Aboav. The arrangement of grains in a polycrystal. *Metallography*, 3(4): 383–390, 1970. doi: 10.1016/0026-0800(70)90038-8.

[6] Frederic T Lewis. The correlation between cell division and the shapes and sizes of prismatic cells in the epidermis of cucumis. *The anatomical record*, 38 (3):341–376, 1928.

[7] Torbjörn Björkman, Simon Kurasch, Ossi Lehtinen, Jani Kotakoski, Oleg V Yazyev, Anchal Srivastava, Viera Skakalova, Jurgen H Smet, Ute Kaiser, and Arkady V Krasheninnikov. Defects in bilayer silica and graphene: common trends in diverse hexagonal two-dimensional systems. *Scientific reports*, 3:3482, 2013. doi: 10.1038/srep03482.

[8] Leonid Lichtenstein, Christin Büchner, Bing Yang, Shamil Shaikhutdinov, Markus Heyde, Marek Sierka, Radosław Włodarczyk, Joachim Sauer, and Hans-Joachim Freund. The atomic structure of a metal-supported vitreous thin silica film. *Angewandte Chemie International Edition*, 51(2):404–407, 2012. doi: 10.1002/anie.201107097.

[9] Mahdi Sadjadi, Bishal Bhattarai, DA Drabold, MF Thorpe, and Mark Wilson. Refining glass structure in two dimensions. *Physical Review B*, 96(20):201405, 2017. doi: 10.1103/PhysRevB.96.201405.

[10] W. A. Phillips. Two-level states in glasses. *Reports on Progress in Physics*, 50 (12):1657–1708, dec 1987. doi: 10.1088/0034-4885/50/12/003.

[11] R. C. Zeller and R. O. Pohl. Thermal Conductivity and Specific Heat of Noncrystalline Solids. *Physical Review B*, 4(6):2029–2041, sep 1971. ISSN 0556-2805. doi: 10.1103/PhysRevB.4.2029. URL `https://link.aps.org/doi/10.1103/PhysRevB.4.2029`.

[12] U Buchenau, M Prager, N Nücker, AJ Dianoux, N Ahmad, and WA Phillips. Low-frequency modes in vitreous silica. *Physical Review B*, 34(8):5665, 1986. doi: 10.1103/PhysRevB.34.5665.

[13] KS Novoselov, D Jiang, F Schedin, TJ Booth, VV Khotkevich, SV Morozov, and AK Geim. Two-dimensional atomic crystals. *Proceedings of the National Academy of Sciences of the United States of America*, 102(30):10451–10453, 2005. doi: 10.1073/pnas.0502848102.

[14] Adrián Leandro Lewandowski, Philomena Schlexer, Christin Büchner, Earl M Davis, Hannah Burrall, Kristen M Burson, Wolf-Dieter Schneider, Markus Heyde, Gianfranco Pacchioni, and Hans-Joachim Freund. Atomic structure of a metal-supported two-dimensional germania film. *Physical Review B*, 97 (11):115406, 2018. doi: 10.1103/PhysRevB.97.115406.

[15] ML Frankenheim. Die lehre von der cohäfion. *Schulz, Breslau*, pages 389–390, 1835.

[16] Peter Debye and Paul Scherrer. Interferenzen an regellos orientierten teilchen im röntgenlicht. i. *Nachrichten von der Gesellschaft der Wissenschaften zu Göttingen, Mathematisch-Physikalische Klasse*, 1916:1–15, 1916.

[17] AA Lebedev. O polimorfizme i otzhige stekla, trud'i gos. opt. inst. 2 1-20 (1921)(in russian); ibid. *Izv. Akad. Nauk SSSR, Otd. Mat. Estestv. Nauk, Ser. Fiz*, 3:381, 1921.

[18] William Houlder Zachariasen. The atomic arrangement in glass. *Journal of the American Chemical Society*, 54(10):3841–3851, 1932. doi: 10.1021/ja01349a006.

[19] W Rosenhain. The structure and constitution of glass. *J. Soc. Glass Technol. Trans*, 11:77–97, 1927.

[20] Adrian C Wright. The great crystallite versus random network controversy: a personal perspective. *International Journal of Applied Glass Science*, 5(1): 31–56, 2014. doi: 10.1111/ijag.12039.

[21] M. Sadjadi and M.F.Thorpe. Ring correlations in random networks. *Physical Review E*, 94(6):062304, 2016. doi: 10.1103/PhysRevE.94.062304.

[22] David A Keen and Martin T Dove. Local structures of amorphous and crystalline phases of silica, SiO_2, by neutron total scattering. *Journal of Physics: Condensed Matter*, 11(47):9263, 1999. doi: 10.1088/0953-8984/11/47/311.

[23] Doris L Evans and Shirley V King. Random network model of vitreous silica. *Nature*, 212(5068):1353, 1966. doi: 10.1038/2121353a0.

[24] RJ Bell and P Dean. Properties of vitreous silica: Analysis of random network models. *Nature*, 212(5068):1354, 1966. doi: 10.1038/2121354a0.

[25] RJ Bell and P Dean. The structure of vitreous silica: Validity of the random network theory. *Philosophical Magazine*, 25(6):1381–1398, 1972. doi: 10.1080/14786437208223861.

[26] LV Woodcock, CA Angell, and P Cheeseman. Molecular dynamics studies of the vitreous state: Simple ionic systems and silica. *The Journal of chemical physics*, 65(4):1565–1577, 1976. doi: 10.1063/1.433213.

[27] LB Vessal, M Leslie, and CRA Catlow. Molecular dynamics simulation of silica glass. *Molecular Simulation*, 3(1-3):123–136, 1989. doi: 10.1080/08927028908034623.

[28] Sean Michael Collins, RK Leary, PA Midgley, Robert Tovey, Martin Benning, C-B Schönlieb, P Rez, and MMJ Treacy. Entropic comparison of atomic-resolution electron tomography of crystals and amorphous materials. *Physical review letters*, 119(16):166101, 2017. doi: 10.1103/PhysRevLett.119.166101.

[29] Daniel Löffler, John J Uhlrich, M Baron, Bing Yang, Xin Yu, Leonid Lichtenstein, Lars Heinke, Christin Büchner, Markus Heyde, Shamil Shaikhutdinov, et al. Growth and structure of crystalline silica sheet on Ru (0001). *Physical review letters*, 105(14):146104, 2010. doi: 10.1103/PhysRevLett.105.146104.

[30] David Kuhness, Hyun Jin Yang, Hagen W Klemm, Mauricio Prieto, Gina Peschel, Alexander Fuhrich, Dietrich Menzel, Thomas Schmidt, Xin Yu, Shamil Shaikhutdinov, et al. A two-dimensional 'zigzag' silica polymorph on a metal support. *Journal of the American Chemical Society*, 2018. doi: 10.1021/jacs.8b02905.

[31] Eric I Altman, Jan Gotzen, Niveditha Samudrala, and Udo D Schwarz. Growth and characterization of crystalline silica films on pd (100). *The Journal of Physical Chemistry C*, 117(49):26144–26155, 2013.

[32] Jin Zhang. Phase transformation in two-dimensional crystalline silica under compressive loading. *Physical Chemistry Chemical Physics*, 19(12):8478–8484, 2017. doi: 10.1039/C7CP00273D.

[33] Jin Zhang. Phase-dependent mechanical properties of two-dimensional silica films: A molecular dynamics study. *Computational Materials Science*, 142:7–13, 2018. doi: 10.1016/j.commatsci.2017.10.005.

[34] Christin Büchner and Markus Heyde. Two-dimensional silica opens new perspectives. *Progress in Surface Science*, 2017. doi: 10.1016/j.progsurf.2017.09.001.

[35] Andrei Malashevich, Sohrab Ismail-Beigi, and Eric I Altman. Directing the structure of two-dimensional silica and silicates. *The Journal of Physical Chemistry C*, 120(47):26770–26781, 2016. doi: 10.1021/acs.jpcc.6b07008.

[36] Jean-François Sadoc and Nicolas Rivier. *Foams and emulsions*, volume 354. Springer Science & Business Media, 1999. doi: 10.1007/978-94-015-9157-7.

[37] Jose Carlos Merino Mombach, RMC De Almeida, and Jose Roberto Iglesias. Two-cell correlations in biological tissues. *Physical Review E*, 47(5):3712, 1993. doi: 10.1103/PhysRevE.47.3712.

[38] W Korneta, SK Mendiratta, and J Menteiro. Topological and geometrical properties of crack patterns produced by the thermal shock in ceramics. *Physical Review E*, 57(3):3142, 1998. doi: 10.1103/PhysRevE.57.3142.

[39] D Weaire and N Rivier. Soap, cells and statistics – random patterns in two dimensions. *Contemporary Physics*, 25(1):59–99, 1984. URL `http://dx.doi.org/10.1080/00107518408210979`.

[40] Joel Stavans. The evolution of cellular structures. *Reports on progress in physics*, 56(6):733, 1993. URL `http://dx.doi.org/10.1088/0034-4885/56/6/002`.

[41] Miguel A Aragón-Calvo. The universe as a cellular system. *ArXiv e-prints*, 2014.

[42] Gudrun Schliecker. Scaling analysis of 2d fractal cellular structures. *Journal of Physics A: Mathematical and General*, 34(1):25, 2001. doi: 10.1088/0305-4470/34/1/302.

[43] DS Franzblau. Computation of ring statistics for network models of solids. *Physical Review B*, 44(10):4925, 1991. doi: 10.1103/PhysRevB.44.4925.

[44] Graham Flegg. *From geometry to topology*. Courier Corporation, 1974. ISBN 9780486419619.

[45] EN da C Andrade and DA Aboav. Distribution of grain size in annealed metals. *Nature*, 207(4992):68, 1965. doi: 10.1038/207068b0.

[46] D Weaire. Some remarks on the arrangement of grains in a polycrystal. *Metallography*, 7(2):157–160, 1974. doi: 10.1016/0026-0800(74)90004-4.

[47] Avishek Kumar, David Sherrington, Mark Wilson, and M F Thorpe. Ring statistics of silica bilayers. *Journal of Physics: Condensed Matter*, 26(39):395401, 2014. doi: 10.1088/0953-8984/26/39/395401.

[48] Louis Theran, Anthony Nixon, Elissa Ross, Mahdi Sadjadi, Brigitte Servatius, and Michael F Thorpe. Anchored boundary conditions for locally isostatic networks. *Physical Review E*, 92(5):053306, 2015. doi: 10.1103/PhysRevE.92.053306.

[49] Simeng Yan, David A Huse, and Steven R White. Spin-liquid ground state of the s= 1/2 kagome heisenberg antiferromagnet. *Science*, 332(6034):1173–1176, 2011. doi: 10.1126/science.1201080.

[50] Qian Chen, Sung Chul Bae, and Steve Granick. Directed self-assembly of a colloidal kagome lattice. *Nature*, 469(7330):381, 2011. doi: 10.1038/nature09713.

[51] Gyu-Boong Jo, Jennie Guzman, Claire K Thomas, Pavan Hosur, Ashvin Vishwanath, and Dan M Stamper-Kurn. Ultracold atoms in a tunable optical kagome lattice. *Physical review letters*, 108(4):045305, 2012. doi: 10.1103/PhysRevLett.108.045305.

[52] Kai Sun, Anton Souslov, Xiaoming Mao, and TC Lubensky. Surface phonons, elastic response, and conformal invariance in twisted kagome lattices. *Proceedings of the National Academy of Sciences*, 109(31):12369–12374, 2012. doi: 10.1073/pnas.1119941109.

[53] Noah P Mitchell, Lisa M Nash, Daniel Hexner, Ari M Turner, and William TM Irvine. Amorphous topological insulators constructed from random point sets. *Nature Physics*, page 1, 2018. doi: 10.1038/s41567-017-0024-5.

[54] Carl P Goodrich, Andrea J Liu, and Sidney R Nagel. The principle of independent bond-level response: Tuning by pruning to exploit disorder for global behavior. *Physical review letters*, 114(22):225501, 2015. doi: 10.1103/PhysRevLett.114.225501.

[55] Varda F Hagh, Eric I Corwin, Kenneth Stephenson, and MF Thorpe. Jamming in perspective. *arXiv preprint arXiv:1803.03869*, 2018.

[56] Varda F Hagh and MF Thorpe. Disordered auxetic networks with no re-entrant polygons. *arXiv preprint arXiv:1805.03708*, 2018.

[57] F Wooten, K Winer, and D Weaire. Computer generation of structural models of amorphous si and ge. *Physical review letters*, 54(13):1392, 1985. doi: 10.1103/PhysRevLett.54.1392.

[58] AJ Stone and DJ Wales. Theoretical studies of icosahedral c 60 and some related species. *Chemical Physics Letters*, 128(5):501–503, 1986. doi: 10.1016/0009-2614(86)80661-3.

[59] PN Keating. Effect of invariance requirements on the elastic strain energy of crystals with application to the diamond structure. *Physical Review*, 145(2):637, 1966. doi: 10.1103/PhysRev.145.637.

[60] Richard LC Vink. A finite-temperature monte carlo algorithm for network forming materials. *The Journal of chemical physics*, 140(10):104509, 2014. doi: 10.1063/1.4867897.

[61] James F Shackelford and Brian D Brown. The lognormal distribution in the random network structure. *Journal of Non-Crystalline Solids*, 44(2-3):379–382, 1981.

[62] Jerry Tersoff. New empirical approach for the structure and energy of covalent systems. *Physical Review B*, 37(12):6991, 1988. doi: 10.1103/PhysRevB.37.6991.

[63] Projesh Kumar Roy, Markus Heyde, and Andreas Heuer. Modelling the atomic arrangement of amorphous 2d silica: A network analysis. *Physical Chemistry Chemical Physics*, 2018.

[64] Avishek Kumar, Mark Wilson, and M F Thorpe. Amorphous graphene: a realization of zachariasen's glass. *Journal of Physics: Condensed Matter*, 24 (48):485003, 2012. URL 10.1088/0953-8984/24/48/485003.

[65] C.J. Dawson, R. Sanchez-Smith, P. Rez, M. O'Keefe, and M.M.J. Treacy. Ab initio calculations of the energy dependence of Si–O–Si angles in silica and Ge–O–Ge angles in germania crystalline systems. *Chemistry of Materials*, 26(4): 1523–1527, 2014. doi: 10.1021/cm402814v.

[66] P K Gupta and A R Cooper. Topologically disordered networks of rigid polytopes. *Journal of Non-Crystalline Solids*, 123(1):14–21, 1990. doi: 10.1016/0022-3093(90)90768-H.

[67] Adrian C Wright. Neutron scattering from vitreous silica. v. the structure of vitreous silica: what have we learned from 60 years of diffraction studies? *Journal of non-crystalline solids*, 179:84–115, 1994. doi: 10.1016/0022-3093(94)90687-4.

[68] Stephen R Elliott. Medium-range structural order in covalent amorphous solids. *Nature*, 354:445–452, 1991. doi: 10.1038/354445a0.

[69] Michael F Thorpe and Ladislav Tichỳ. *Properties and applications of amorphous materials*, volume 9. Springer Science & Business Media, 2012. doi: 10.1007/978-94-010-0914-0.

[70] M M J Treacy, J M Gibson, L Fan, D J Paterson, and I McNulty. Fluctuation microscopy: a probe of medium range order. *Reports on Progress in Physics*, 68(12):2899, 2005. doi: 10.1088/0034-4885/68/12/R06.

[71] D E Bürgler, C M Schmidt, D M Schaller, F Meisinger, T M Schaub, A Baratoff, and H-J Güntherodt. Atomic-scale scanning tunneling microscopy of amorphous surfaces. *Physical Review B*, 59(16):10895, 1999. doi: 10.1103/PhysRevB.59.10895.

[72] Mark Wilson, Avishek Kumar, David Sherrington, and M F Thorpe. Modeling vitreous silica bilayers. *Physical Review B*, 87(21):214108, 2013. doi: 10.1103/PhysRevB.87.214108.

[73] Mark Wilson. Modelling networks in varying dimensions. In *Molecular Dynamics Simulations of Disordered Materials*, pages 215–254. Springer, 2015. doi: 10.1007/978-3-319-15675-0_9.

[74] Christin Büchner, Liwei Liu, Stefanie Stuckenholz, Kristen M Burson, Leonid Lichtenstein, Markus Heyde, Hong-Jun Gao, and Hans-Joachim Freund. Building block analysis of 2d amorphous networks reveals medium range correlation. *Journal of Non-Crystalline Solids*, 435:40–47, 2016. doi: 10.1016/j.jnoncrysol.2015.12.020.

[75] M F Thorpe. Continuous deformations in random networks. *Journal of Non-Crystalline Solids*, 57(3):355–370, 1983. doi: 10.1016/0022-3093(83)90424-6.

[76] Wouter G Ellenbroek, Varda F Hagh, Avishek Kumar, M F Thorpe, and Martin van Hecke. Rigidity loss in disordered systems: Three scenarios. *Physical review letters*, 114(13):135501, 2015. doi: 10.1103/PhysRevLett.114.135501.

[77] J Kotakoski, A V Krasheninnikov, U Kaiser, and J C Meyer. From point defects in graphene to two-dimensional amorphous carbon. *Physical Review Letters*, 106 (10):105505, 2011. doi: 10.1103/PhysRevLett.106.105505.

[78] Christin Büchner, Philomena Schlexer, Leonid Lichtenstein, Stefanie Stuckenholz, Markus Heyde, and Hans-Joachim Freund. Topological investigation of two-dimensional amorphous materials. *Zeitschrift für physikalische Chemie*, 228 (4-5):587–607, 2014. doi: 10.1515/zpch-2014-0438.

[79] Lorna J Gibson and Michael F Ashby. *Cellular solids: structure and properties*. Cambridge university press, 1999.

[80] Gudrun Schliecker. Structure and dynamics of cellular systems. *Advances in Physics*, 51(5):1319–1378, 2002. doi: 10.1080/00018730210140814.

[81] HW Klemm, Gina Peschel, Ewa Madej, Alexander Fuhrich, Martin Timm, Dietrich Menzel, Th Schmidt, and H-J Freund. Preparation of silica films on ru (0001): A leem/peem study. *Surface Science*, 643:45–51, 2016. doi: 10.1016/j.susc.2015.05.017.

[82] M A Fortes and P Pina. Average topological properties of successive neighbours of cells in random networks. *Philosophical Magazine B*, 67(2):263–276, 1993. doi: 10.1080/13642819308207873.

[83] J. K. Mason, E. A. Lazar, R. D. MacPherson, and D. J. Srolovitz. Geometric and topological properties of the canonical grain-growth microstructure. *Physical Review E*, 92(6):063308, December 2015. doi: 10.1103/PhysRevE.92.063308.

[84] T Aste, Kwok-Yip Szeto, and Wing-Yim Tam. Statistical properties and shell analysis in random cellular structures. *Physical Review E*, 54(5):5482, 1996. doi: 10.1103/PhysRevE.54.5482.

[85] Tomaso Aste, Dominique Boose, and Nicolas Rivier. From one cell to the whole froth: a dynamical map. *Physical Review E*, 53(6):6181, 1996. doi: 10.1103/PhysRevE.53.6181.

[86] C J Lambert and D Weaire. Order and disorder in two-dimensional random networks. *Philosophical Magazine Part B*, 47(4):445–450, 1983. doi: 10.1080/1364281.1983.10590681.

[87] C Oguey and N Rivier. Roughness and scaling in cellular patterns: analysis of a simple model. *Journal of Physics A: Mathematical and General*, 34(32):6225, 2001. doi: 10.1088/0305-4470/34/32/302.

[88] S N Chiu. Aboav-weaire's and lewis' laws – a review. *Materials characterization*, 34(2):149–165, 1995. doi: 10.1016/1044-5803(94)00081-U.

[89] J K Mason, R Ehrenborg, and E A Lazar. A geometric formulation of the law of aboav– weaire in two and three dimensions. *Journal of Physics A: Mathematical and Theoretical*, 45(6):065001, 2012. doi: 10.1088/1751-8113/45/6/065001.

[90] DA Aboav. The arrangement of cells in a net. iii. *Metallography*, 17(4):383–396, 1984. doi: 10.1016/0026-0800(84)90075-2.

[91] H Wang and G Q Liu. Generalization of the aboav-weaire law. *EPL (Europhysics Letters)*, 100(6):68001, 2012. doi: 10.1209/0295-5075/100/68001.

[92] Hao Wang, Guoquan Liu, Ying Chen, Arkapol Saengdeejing, Hideo Miura, and Ken Suzuki. Long-range topological correlations of real polycrystalline grains in two dimensions. *Materials Characterization*, 97:178–182, 2014. doi: 10.1016/j.matchar.2014.09.017.

[93] K Y Szeto, T Aste, and W Y Tam. Topological correlations in soap froths. *Physical Review E*, 58(2):2656, 1998. doi: 10.1103/PhysRevE.58.2656.

[94] G Le Caer and R Delannay. Correlations in topological models of 2d random cellular structures. *Journal of Physics A: Mathematical and General*, 26(16): 3931, 1993. doi: 10.1088/0305-4470/26/16/011.

[95] C Oguey. Long range topological correlations in cellular patterns. *Colloids and Surfaces A: Physicochemical and Engineering Aspects*, 382(1):32–35, 2011. doi: 10.1016/j.colsurfa.2011.02.017.

[96] M F Miri and Christophe Oguey. Topological correlations and asymptotic freedom in cellular aggregates. *Colloids and Surfaces A: Physicochemical and Engineering Aspects*, 309(1):107–111, 2007. doi: 10.1016/j.colsurfa.2007.01.013.

[97] Oded Hod, Juan E. Peralta, and Gustavo E. Scuseria. Edge effects in finite elongated graphene nanoribbons. *Phys. Rev. B*, 76:233401, Dec 2007. doi: 10.1103/PhysRevB.76.233401. URL `http://link.aps.org/doi/10.1103/PhysRevB.76.233401`.

[98] M.F. Thorpe. Bulk and surface floppy modes. *Journal of Non-Crystalline Solids*, 182(1–2):135 – 142, 1995. ISSN 0022-3093. doi: http://dx.doi.org/10.1016/0022-3093(94)00545-1. URL `http://www.sciencedirect.com/science/article/pii/0022309394005451`.

[99] T C Lubensky, C L Kane, Xiaoming Mao, A Souslov, and Kai Sun. Phonons and elasticity in critically coordinated lattices. *Reports on Progress in Physics*, 78 (7):073901, 2015. doi: 10.1088/0034-4885/78/7/073901. URL `http://stacks.iop.org/0034-4885/78/i=7/a=073901`.

[100] G. Laman. On graphs and rigidity of plane skeletal structures. *J. Engrg. Math.*, 4:331–340, 1970. ISSN 0022-0833. URL `http://dx.doi.org/10.1007/BF01534980`.

[101] D. J. Jacobs and M. F. Thorpe. Generic rigidity percolation: The pebble game. *Phys. Rev. Lett.*, 75:4051–4054, Nov 1995. doi: 10.1103/PhysRevLett.75.4051. URL http://link.aps.org/doi/10.1103/PhysRevLett.75.4051.

[102] D. J. Jacobs and M. F. Thorpe. Generic rigidity percolation in two dimensions. *Phys. Rev. E*, 53:3682–3693, Apr 1996. doi: 10.1103/PhysRevE.53.3682. URL http://link.aps.org/doi/10.1103/PhysRevE.53.3682.

[103] Ileana Streinu and Louis Theran. Slider-pinning rigidity: a Maxwell-Laman-type theorem. *Discrete Comput. Geom.*, 44(4):812–837, 2010. ISSN 0179-5376. doi: 10.1007/s00454-010-9283-y. URL http://dx.doi.org/10.1007/s00454-010-9283-y.

[104] Jack Graver, Brigitte Servatius, and Herman Servatius. *Combinatorial rigidity*, volume 2 of *Graduate Studies in Mathematics*. American Mathematical Society, Providence, RI, 1993. ISBN 0-8218-3801-6. doi: 10.1090/gsm/002. URL http://dx.doi.org/10.1090/gsm/002.

[105] James Clerk Maxwell. On the calculation of the equilibrium and stiffness of frames. *The London, Edinburgh, and Dublin Philosophical Magazine and Journal of Science*, 27:294–299, 1864. URL http://dx.doi.org/10.1080/14786446408643668.

[106] J. A. Bondy and U. S. R. Murty. *Graph theory*, volume 244 of *Graduate Texts in Mathematics*. Springer, New York, 2008. ISBN 978-1-84628-969-9. doi: 10.1007/978-1-84628-970-5. URL http://dx.doi.org/10.1007/978-1-84628-970-5.

[107] Tiong-Seng Tay. Linking $(n-2)$-dimensional panels in n-space. II. $(n-2,2)$-frameworks and body and hinge structures. *Graphs Combin.*, 5(3):245–273, 1989. ISSN 0911-0119. doi: 10.1007/BF01788678. URL http://dx.doi.org/10.1007/BF01788678.

[108] Walter Whiteley. The union of matroids and the rigidity of frameworks. *SIAM J. Discrete Math.*, 1(2):237–255, 1988. ISSN 0895-4801. doi: 10.1137/0401025. URL http://dx.doi.org/10.1137/0401025.

[109] Walter Whiteley. A matroid on hypergraphs, with applications in scene analysis and geometry. *Discrete Comput. Geom.*, 4(1):75–95, 1989. ISSN 0179-5376. doi: 10.1007/BF02187716. URL http://dx.doi.org/10.1007/BF02187716.

[110] Bill Jackson and Tibor Jordán. Pin-collinear body-and-pin frameworks and the molecular conjecture. *Discrete & Computational Geometry*, 40(2):258–278, 2008. ISSN 0179-5376. doi: 10.1007/s00454-008-9100-z. URL http://dx.doi.org/10.1007/s00454-008-9100-z.

[111] Naoki Katoh and Shin-ichi Tanigawa. Rooted-tree decompositions with matroid constraints and the infinitesimal rigidity of frameworks with boundaries. *SIAM J. Discrete Math.*, 27(1):155–185, 2013. ISSN 0895-4801. doi: 10.1137/110846944. URL http://dx.doi.org/10.1137/110846944.

[112] Neil L. White and Walter Whiteley. The algebraic geometry of stresses in frameworks. *SIAM J. Algebraic Discrete Methods*, 4(4):481–511, 1983. ISSN 0196-5212. doi: 10.1137/0604049. URL `http://dx.doi.org/10.1137/0604049`.

[113] Henry E Fischer, Adrian C Barnes, and Philip S Salmon. Neutron and x-ray diffraction studies of liquids and glasses. *Reports on Progress in Physics*, 69(1): 233, 2005. doi: 10.1088/0034-4885/69/1/R05.

[114] Carol S Marians and Linn W Hobbs. Local structure of silica glasses. *Journal of Non-Crystalline Solids*, 119(3):269–282, 1990. doi: 10.1016/0022-3093(90)90299-2.

[115] Anita Zeidler, Kamil Wezka, Ruth F Rowlands, Dean AJ Whittaker, Philip S Salmon, Annalisa Polidori, James WE Drewitt, Stefan Klotz, Henry E Fischer, Martin C Wilding, et al. High-pressure transformation of SiO_2 glass from a tetrahedral to an octahedral network: a joint approach using neutron diffraction and molecular dynamics. *Physical review letters*, 113(13):135501, 2014. doi: 10.1103/PhysRevLett.113.135501.

[116] Leonid Lichtenstein. The Structure of Two-Dimensional Vitreous Silica. 2012.

[117] Philip S Salmon, Richard A Martin, Philip E Mason, and Gabriel J Cuello. Topological versus chemical ordering in network glasses at intermediate and extended length scales. *Nature*, 435(7038):75–78, 2005. doi: 10.1038/nature03475.

[118] Philip S Salmon. Moments of the Bhatia–Thornton partial pair-distribution functions. *Journal of Physics: Condensed Matter*, 17(45):S3537, 2005. doi: 10.1088/0953-8984/17/45/045.

[119] Philip S Salmon. The structure of tetrahedral network glass forming systems at intermediate and extended length scales. *Journal of Physics: Condensed Matter*, 19(45):455208, 2007. doi: 10.1088/0953-8984/19/45/455208.

[120] Philip S Salmon, Adrian C Barnes, Richard A Martin, and Gabriel J Cuello. Glass fragility and atomic ordering on the intermediate and extended range. *Physical Review Letters*, 96(23):235502, 2006. doi: 10.1103/PhysRevLett.96.235502.

[121] Philip S Salmon, Adrian C Barnes, Richard A Martin, and Gabriel J Cuello. Structure of glassy GeO_2. *Journal of Physics: Condensed Matter*, 19(41): 415110, 2007. doi: 10.1088/0953-8984/19/41/415110.

[122] Mark Wilson. Structure and dynamics in network-forming materials. *Journal of Physics: Condensed Matter*, 28(50):503001, 2016. doi: 10.1088/0953-8984/28/50/503001.

[123] J.Weissenrieder, S.Kaya, J-L.Lu, H-J.Gao, S.Shaikhutdinov, H-J.Freund, M.Sierka, T.K.Todorova, and J.Sauer. Atomic structure of a thin silica film on a Mo (112) substrate: a two-dimensional network of SiO_4 tetrahedra. *Physical review letters*, 95(7):076103, 2005.

[124] Mark Wilson, Avishek Kumar, David Sherrington, and M. F. Thorpe. Modeling vitreous silica bilayers. *Physical Review B - Condensed Matter and Materials Physics*, 87(21):1–10, 2013. ISSN 10980121. doi: 10.1103/PhysRevB.87.214108.

[125] A Sartbaeva, SA Wells, A Huerta, and MF Thorpe. Local structural variability and the intermediate phase window in network glasses. *Physical Review B*, 75 (22):224204, 2007. doi: 10.1103/PhysRevB.75.224204.

[126] Paul A Madden and Mark Wilson. 'Covalent' effects in 'ionic' systems. *Chemical Society Reviews*, 25(5):339–350, 1996. doi: 10.1039/CS9962500339.

[127] Paul Tangney and Sandro Scandolo. An ab initio parametrized interatomic force field for silica. *The Journal of chemical physics*, 117(19):8898–8904, 2002. doi: 10.1063/1.1513312.

[128] José M Soler, Emilio Artacho, Julian D Gale, Alberto García, Javier Junquera, Pablo Ordejón, and Daniel Sánchez-Portal. The siesta method for ab initio order-n materials simulation. *Journal of Physics: Condensed Matter*, 14(11): 2745, 2002. doi: 10.1088/0953-8984/14/11/302.

[129] Bishal Bhattarai and DA Drabold. Vibrations in amorphous silica. *Journal of Non-Crystalline Solids*, 439:6–14, 2016. doi: 10.1016/j.jnoncrysol.2016.02.002.

[130] JA Erwin Desa, Adrian C Wright, Joe Wong, and Roger N Sinclair. A neutron diffraction investigation of the structure of vitreous zinc chloride. *Journal of Non-Crystalline Solids*, 51(1):57–86, 1982. doi: 10.1016/0022-3093(82)90189-2.

[131] Jörg Neuefeind and K-D Liss. Bond angle distribution in amorphous germania and silica. *Berichte der Bunsengesellschaft für physikalische Chemie*, 100(8): 1341–1349, 1996. doi: 10.1002/bbpc.19961000812.

[132] Vitaliy Kapko, C Dawson, MMJ Treacy, and MF Thorpe. Flexibility of ideal zeolite frameworks. *Physical Chemistry Chemical Physics*, 12(30):8531–8541, 2010. doi: 10.1039/C003977B.

[133] Anastassis Perrakis, Richard Morris, and Victor S Lamzin. Automated protein model building combined with iterative structure refinement. *Nature structural & molecular biology*, 6(5):458–463, 1999. doi: 10.1038/8263.

[134] John Towns, Timothy Cockerill, Maytal Dahan, Ian Foster, Kelly Gaither, Andrew Grimshaw, Victor Hazlewood, Scott Lathrop, Dave Lifka, Gregory D Peterson, et al. XSEDE: accelerating scientific discovery. *Computing in Science & Engineering*, 16(5):62–74, 2014. doi: 10.1109/MCSE.2014.80.

[135] Charles Kittel. *Introduction to solid state physics*. Wiley, 2005.

[136] Brage Golding and John E. Graebner. Phonon echoes in glass. *Physical Review Letters*, 37(13):852–855, 1976. ISSN 00319007. doi: 10.1103/PhysRevLett.37.852.

[137] John E. Graebner and Brage Golding. Phonon echoes in a glass at low temperatures. *Physical Review B*, 19(2):964–975, 1979. ISSN 01631829. doi: 10.1103/PhysRevB.19.964.

[138] J. E. Graebner, L. C. Allen, B. Golding, and A. B. Kane. Acoustic saturation in a glass at low temperatures. *Physical Review B*, 27(6):3697–3708, 1983. ISSN 01631829. doi: 10.1103/PhysRevB.27.3697.

[139] Albert Einstein. Die plancksche theorie der strahlung und die theorie der spezifischen waerme. *Annalen der Physik*, 327(1):180–190, 1907. doi: 10.1002/andp.19063270110.

[140] Albert Einstein. Eine beziehung zwischen dem elastischen verhalten und der spezifischen wärme bei festen körpern mit einatomigem molekül. *Annalen der Physik*, 339(1):170–174, 1911. doi: 10.1002/andp.19113390110.

[141] Peter Debye. Zur theorie der spezifischen wärmen. *Annalen der Physik*, 344 (14):789–839, 1912. doi: 10.1002/andp.19123441404.

[142] P. W. Anderson, B. I. Halperin, and C. M. Varma. Anomalous low-temperature thermal properties of glasses and spin glasses. *Philosophical Magazine*, 25(1): 1–9, 1972. ISSN 0031-8086. doi: 10.1080/14786437208229210.

[143] W. A. Phillips. Tunneling states in amorphous solids. *Journal of Low Temperature Physics*, 7(3-4):351–360, 1972. ISSN 00222291. doi: 10.1007/BF00660072.

[144] Timothy Good Abbott. *Generalizations of Kempe's universality theorem*. PhD thesis, Massachusetts Institute of Technology, 2008.

[145] Hakan Guler, Bill Jackson, and Anthony Nixon. Rigidity of linearly-constrained frameworks. *arXiv preprint arXiv:1804.00411*, 2018.

[146] Michael F Thorpe, Donald J Jacobs, NV Chubynsky, and AJ Rader. Generic rigidity of network glasses. In *Rigidity theory and applications*, pages 239–277. Springer, 2002. doi: 10.1007/0-306-47089-6_14.

[147] Bruce Hendrickson. Conditions for unique graph realizations. *SIAM J. Comput.*, 21(1):65–84, 1992. ISSN 0097-5397. doi: 10.1137/0221008. URL `http://epubs.siam.org/doi/abs/10.1137/0221008`.

[148] Steven J. Gortler, Alexander D. Healy, and Dylan P. Thurston. Characterizing generic global rigidity. *American Journal of Mathematics*, 132(4):897–939, may 2010. ISSN 1080-6377. doi: 10.1353/ajm.0.0132. URL `http://arxiv.org/abs/0710.0926http://dx.doi.org/10.1016/j.adhoc.2011.06.016http://linkinghub.elsevier.com/retrieve/pii/S1570870511001491http://muse.jhu.edu/content/crossref/journals/american{_}journal{_}of{_}mathematics/v132/132.4.gortler.html`.

[149] Wieb Bosma, John Cannon, and Catherine Playoust. The Magma algebra system. I. The user language. *J. Symbolic Comput.*, 24(3-4):235–265, 1997. ISSN 0747-7171. doi: 10.1006/jsco.1996.0125. URL `http://dx.doi.org/10.1006/jsco.1996.0125`. Computational algebra and number theory (London, 1993).

[150] Asel Sartbaeva, Stephen A Wells, MMJ Treacy, and MF Thorpe. The flexibility window in zeolites. *Nature materials*, 5(12):962–965, 2006. doi: 10.1038/nmat1784.

[151] Vladimir I Arnol'd. *Catastrophe theory*. Springer Science & Business Media, 2003.

[152] Mitchell J Feigenbaum. Quantitative universality for a class of nonlinear transformations. *Journal of statistical physics*, 19(1):25–52, 1978. doi: 10.1007/BF01020332.

[153] Miranda C Holmes-Cerfon. Enumerating rigid sphere packings. *SIAM Review*, 58(2):229–244, 2016. doi: 10.1137/140982337.

[154] Graeme Henkelman, Blas P Uberuaga, and Hannes Jónsson. A climbing image nudged elastic band method for finding saddle points and minimum energy paths. *The Journal of chemical physics*, 113(22):9901–9904, 2000. doi: 10.1063/1.1329672.

[155] S Hunklinger and W Arnold. Physical acoustics. *Vol. XII*, page 155, 1976.

[156] Kurt Binder and Walter Kob. *Glassy materials and disordered solids: An introduction to their statistical mechanics*. World Scientific, 2011.

[157] Varda F. Hagh. private communication, 2018.

[158] Philip W Anderson. More is different. *Science*, 177(4047):393–396, 1972. doi: 10.1142/9789812385123_others01.

[159] Mark de Berg, Otfried Cheong, Marc van Kreveld, and Mark Overmars. *Computational geometry*. Springer-Verlag, Berlin, third edition, 2008. ISBN 978-3-540-77973-5. doi: 10.1007/978-3-540-77974-2. URL `http://dx.doi.org/10.1007/978-3-540-77974-2`. Algorithms and applications.

[160] Franz J. Király, Ryoty Tomioka, and Louis Theran. The algebraic combinatorial approach for low-rank matrix completion. To appear in *JMLR*, 2015. URL `http://arxiv.org/abs/1211.4116`.

[161] V Narayanamurti and RO Pohl. Tunneling states of defects in solids. *Reviews of Modern Physics*, 42(2):201, 1970. doi: 10.1103/RevModPhys.42.201.

[162] Eugen Merzbacher. Quantum mechanics, thirs edition. *John Wiler & Sons, New York Zbl0102*, 42701(4), 1998.

[163] V Jelic and F Marsiglio. The double-well potential in quantum mechanics: a simple, numerically exact formulation. *European Journal of Physics*, 33(6): 1651, 2012. doi: 10.1088/0143-0807/33/6/1651.

[164] Michael Egmont-Petersen, Dick de Ridder, and Heinz Handels. Image processing with neural networks—a review. *Pattern recognition*, 35(10):2279–2301, 2002. doi: 10.1016/S0031-3203(01)00178-9.

[165] Varda F. Hagh. *On the rigidity of disoreded networks*. Ph.D. dissertation, Arizona State University, 2018.

APPENDIX A

IMPLEMENTATION OF SLIDING AND ANCHORED BOUNDARY CONDITIONS

This appendix extends the discussion in Chapter 3 and offers computational algorithms to implement sliding and anchored boundary conditions for locally isostatic networks.

Implementation details

Algorithms 1–4 in this appendix give a procedural description of the four boundary conditions discussed in this paper, and make clear the subtle differences between them. All of the algorithms in this appendix take as input a finite part of a locally isostatic network and output a globally isostatic one that is appropriate for further study. Which of the boundary conditions is most appropriate will depend on the intended application.

Before describing the algorithms, we give more detail on how to encode a triangle ring network and the associated set of first-order geometric constraints.

Encodings

Computationally, it is convenient to work not only with the body graph G, as in the main body of the paper, but also with its *line graph* G^* that has as its vertices the triangle corners and edges the triangle sides. We denote by n and m the number of vertices and edges in G and n^* and m^* the same quantities for G^*. Vertices in G are denoted by $v, w, \ldots$ and vertices in G^* by $v^*, w^*, \ldots$. We assume that there is a constant-time mapping $\tau : V(G) \to V(G^*)^3$ that maps each vertex v of G to the associated triangle $\{v_v^*, w_v^*, x_v^*\}$ in G^*. For each boundary vertex v of G, $\tau(v)$ will have a unique degree 2 vertex, which we denote by $T(v)$.

Experimentally, G^* will always be immediately visible. It is also computable in time $O(n)$ from G. If G is planar with given facial structure [1] , then G^* also has an natural planar embedding, and vice-versa. Further, if G^* contains no pair of facial triangles with a common edge, then G is determined by G^*. This is the case in all of our examples.

We also assume that we have access to the coordinates of the vertices of G^*. We denote these by $p(v^*) = (x_{v^*}, y_{v^*})$ for each vertex v^* of G^* and call p a *placement*.

[1] For example, given as a doubly-connected edge list. See, e.g., Section 2.2 of the textbook by de Berg, et al.[159]

First-order geometric constraints

The allowed first-order motions $\dot{p}$ of a triangle ring network G satisfy the system

$$\langle p(v^*) - p(w^*), \dot{p}(v^*) - \dot{p}(w^*) \rangle = 0 \qquad \text{for all edges } v^*w^* \in E(G^*). \tag{A.1}$$

We assume that p maximizes the rank of (A.1), which happens for almost all choices of p. By the theorems in this paper, this rank is equal to m^* when G is a triangle ring network.

Now identify a set $S^* \subset V(G^*)$ of vertices to which we will add one slider constraint. Assign a vector $s(v^*) = (a_{v^*}, b_{v^*})$ to each $v^* \in S^*$. The slider constraints on the first-order motions are:

$$\langle s(v^*), \dot{p}(v^*) \rangle = 0 \qquad \text{for all } v^* \in S^*. \tag{A.2}$$

To guarantee that the combined system (A.1)–(A.2) achieves its maximum rank ($2n^*$ for our sliding boundary condition), it is sufficient to pick each $s(v^*)$ uniformly at random from the unit circle. [2]

Implementing slider-pinning

Algorithm 1 shows how to implement the sliding boundary condition of Theorem 3.

[2] See the appendix of Király et al.[160] for a detailed justification of this and similar statements relating genericity and random sampling.

Algorithm 1 Sliding boundary conditions.

Input: Triangle ring network G, line graph G^*.

Output: Slider constraints implememented the sliding boundary condition.

1: Initialize S^* to the empty set.

2: For each boundary vertex v of G, add $T(v)$ to S^*.

3: For each v^* in S^*, generate a random vector $s(v^*)$ on the unit circle, and use it to create a slider constraint of the form (A.2).

Implementing immobilized vertices

To implement Theorem 4, we could put two independent sliders at vertices of G^*. However, it is simpler to regard (A.1) as a matrix and then discard the columns corresponding to immobilized vertices.

Algorithm 2 Pinned boundary conditions.

Input: Triangle ring network G with an even number of boundary vertices, line graph G^*, boundary cycle C.

Output: Linear constraints pinning (A.1).

1: Let M be the matrix of the system (A.1).

2: Pick a vertex v_0 on C. Set $v = v_0$. Set $b = 1$.

3: If $b = 1$, discard the columns in M corresponding to $T(v)$, and set $b = 0$. Otherwise set $b = 1$. Replace v with its successor on C.

4: If $v = v_0$, output M. Otherwise, go to step 3.

Observe that the loop implemented in steps 2–4 shows how to obtain the free corners of the boundary vertices of G.

Implementing anchoring with additional bars

Anchoring with additional bars amounts to adding edges to G^*. Thus, we describe them graph theoretically only. If the geometric constraints are desired, simply use the new graph to write down (A.1).

Algorithm 3 Anchoring with bars I.

Input: Triangle ring network G, line graph G^*, boundary cycle C.

Output: An isostatic graph containing G^*.

1: Enumerate the boundary vertices $v_1, \ldots, v_t$ of G, ordered along C.

2: Set $H = G^*$.

3: Add edges $T(v_1)T(v_2), \ldots, T(v_3)T(v_2)$ to H.

4: Output H.

The left panel of Figure 3.8 takes the graph H from Theorem 7 to be a "zig-zag triangulation" of a polygon, which is easily seen to be isostatic. This next algorithm gives the implementation of Theorem 7 using this choice.

Algorithm 4 Anchoring with bars II.

Input: Triangle ring network G with an even number of boundary vertices, line graph G^*, boundary cycle C.

Output: An isostatic graph containing G^*.

1: Enumerate alternating boundary vertices $v_1, v_3, \ldots, v_t - 1$ of G, ordered along C.

2: Set $H = G^*$.

3: Add edges $T(v_1)T(v_3), T(v_3)T(v_5), T(v_1)T(v_5)$ to H.

4: For $i = 7, 9, \ldots, t-1$, add the edges $T(v_{i-2})T(v_i), T(v_{i-4})T(v_i)$ to H.

5: Output H.

APPENDIX B

THERMAL PROPERTIES OF TWO-LEVEL SYSTEMS

A symmetric double-well potential can represent a tunneling state (see Fig.5.2). The abscissa corresponds to a configuration coordinate of a group of atoms while the ordinate is the energy. A double-well potential with a barrier height of V_b centered around $a/2$ and with the well separation d can be written as:

$$V(x) = \frac{16V_b}{d^4}\left(\left(x - \frac{a}{2}\right)^2 - \frac{d^2}{4}\right)^2. \tag{B.1}$$

The potential is invariant under parity so the eigenstates will be symmetric and anti-symmetric solutions and the state of the system is a linear combinations of symmetric and antisymmetric eigenstates [161]. The solutions of the Schrodinger equation with the double-well potential can be obtained numerically as will be discussed shortly. However, WKB approximation implies that the splitting between two lowest energy levels has an exponential dependence on the barrier height and the well separation (see Ref. [162], Chapter 5):

$$\text{energy splitting} = k_B T_0 = \Delta_0 = \hbar\Omega e^{-\lambda}, \quad \lambda = d\sqrt{\frac{2mV_b}{\hbar^2}}. \tag{B.2}$$

λ is called the tunneling parameter and Ω is the angular frequency of oscillations (phonons) in one well assuming a harmonic approximation:

$$\Omega = \sqrt{\frac{1}{m}\frac{d^2V(x)}{\mathrm{d}x^2}} = \sqrt{\frac{32V_b}{md^2}}, \tag{B.3}$$

where m is the mass of the particle. The energy scale of such phonon is $E_{\text{phonon}} = \frac{1}{2}m\Omega^2 d^2$. If the tunneling state is to contribute into the thermal properties, T_0 should be of order of environment temperature T. It is constructive to find the order of the quantities involved in the tunneling paramter. At $T_0 = 1$ K, the splitting energy is $\Delta_0 \approx 10^{-4}$ eV. For an oxygen atom with the mass $m_{\text{O}} \approx 10^{-26}$ kg and the force constant $K_{\text{OO}} = 600$N/m, $\Omega = \sqrt{K_{\text{OO}}/m_O} \approx 10^{14}$ Hz, hence $\hbar\Omega \approx 10^{-2}$ eV. This leads to $\lambda \approx 5$. For $d \approx 1$ Å, the barrier should be of order $V_b \approx 10^{-4}$ eV.

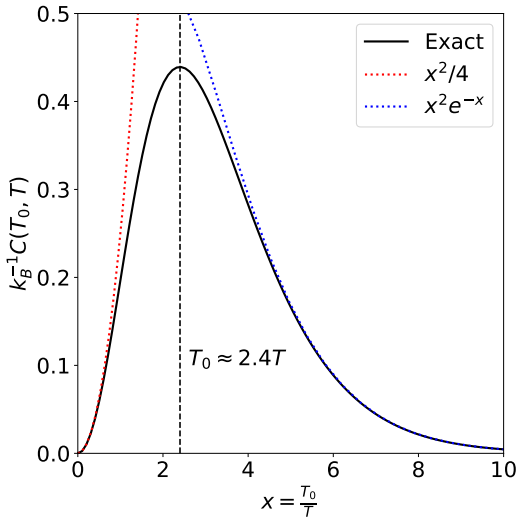

Figure B.1: The specific heat of a two-level system. The maximum specific heat occurs at $T = T_{\max} \approx T_0/2.4$ (the balck dashed line). The red and blue dashed lines show low- and high-temperature limits of the specific heat.

Transition of atoms between two energy levels separated by an energy equal to Δ_0 would contribute to the specific heat. Indeed, it can be shown that the dependence of the specific heat is linear in temperature. To this end, let E_1 and $E_2 = E_1 + \Delta_0$ be the energies associated with the two-level system while Δ_0 is the tunnel splitting in Eq. B.2. The partition function Z reads:

$$Z = \sum_i e^{-\beta E_i} = e^{-\beta E_1} + e^{-\beta E_2} = e^{-\beta E_1}\left(1 + e^{-\beta \Delta_0}\right), \tag{B.4}$$

while the average total energy $\langle E \rangle$ of the system is:

$$\langle E \rangle = -\frac{\partial \ln Z}{\partial \beta} = \frac{1}{Z}\sum_i E_i e^{-\beta E_i} = E_1 + \frac{\Delta_0 e^{-\beta \Delta_0}}{1 + e^{-\beta \Delta_0}}. \tag{B.5}$$

The variation of the energy with respect to temperature is the specific heat C_v of the

two-level system ($\beta = (k_B T)^{-1}$):

$$\begin{aligned} C_v(\Delta_0, T) = \frac{\partial \langle E \rangle}{\partial T} &= k_B \frac{\langle E^2 \rangle - \langle E \rangle^2}{(k_B T)^2} \\ &= k_B (\beta \Delta_0)^2 \frac{e^{-\beta \Delta_0}}{(1 + e^{-\beta \Delta_0})^2} \\ &= k_B \left(\frac{T_0}{T}\right)^2 \frac{e^{-T_0/T}}{(1 + e^{-T_0/T})^2}. \end{aligned} \tag{B.6}$$

It is worth to look at the behavior of the specific heat at two extremes:

$$C_v(\Delta_0, T) = \begin{cases} \frac{1}{4} k_B \left(\frac{T_0}{T}\right)^2 & T_0 \ll T \\ k_B \left(\frac{T_0}{T}\right)^2 e^{-T_0/T} & T_0 \gg T \end{cases} \tag{B.7}$$

Figure B.1 shows the specific heat and its low and high temperature limits and the Schottky anomaly where the maximum specific heat occurs at $T_{\max} \approx T_0/2.4$.

Glassy structures contain an ensemble of such two-level systems which naturally span a wide range of values of the tunnel splitting. In order to find the specific heat of this ensemble, we need to specify the density of splitting energy $\rho(\Delta_0)$ which weights the specific heat of individual two-level systems. The exact form of this distribution possibly depends on the specific microscopic motions involved in the tunneling. We can relate the distributions of splitting energy and tunneling parameter through the definition of the tunneling parameter (Eq. B.2):

$$\rho(\Delta_0) \mathrm{d}\Delta_0 = \rho(\lambda) \frac{\mathrm{d}\lambda}{\mathrm{d}\Delta_0} \mathrm{d}\Delta_0 \propto \rho(\lambda) \frac{\mathrm{d}\Delta_0}{\Delta_0} \tag{B.8}$$

However, splitting energy has an exponential dependence on the tunneling parameter which means a small variation in λ corresponds a large range of Δ_0. But as the range of acceptable Δ_0 is small (as temperature is very low), therefore we can assume that the distribution of λ and Δ_0 are constant. Finally, we can compute the specific heat

of an ensemble of two-level states:

$$\begin{aligned}\int_0^\infty C_v(\Delta_0,T)\rho(\Delta_0)\mathrm{d}\Delta_0 &= k_B\int(\beta\Delta_0)^2\,\frac{e^{-\beta\Delta_0}}{(1+e^{-\beta\Delta_0})^2}\rho(\Delta_0)\mathrm{d}\Delta_0\\ &= k_B\rho_0\beta^{-1}\int(\beta\Delta_0)^2\,\frac{e^{-\beta\Delta_0}}{(1+e^{-\beta\Delta_0})^2}\mathrm{d}\left(\beta\Delta_0\right)\\ &= k_B^2\rho(0)T\int_0^\infty\frac{\chi^2e^{-\chi}}{(1+e^{-\chi})^2}\mathrm{d}\chi\\ &= \left(\frac{\pi^2}{6}k_B^2\rho(0)\right)T\\ &= aT. \end{aligned}\tag{B.9}$$

In the above we have defined $\chi=\beta\Delta_0$ and a is the anomalous coefficient in Eq. 5.1. The upper bound in the integral is set to ∞ as the integrand tends to zero for large values of χ. This proves that an ensemble of two-level systems has a specific heat linear in temperature. Therefore, two-level systems can explain the anomalous behavior of glasses at low temperatures. By comparing the above equation to the linear term in Eq. 5.1, we can estimate the distribution of states. For the experimental data of silica, one finds that $\rho(0)=0.05$ states per eV per SiO_2 group. This means that for $\Delta_0<0.1$ eV, there is 1 two-level system for every ~ 200 tetrahedral SiO_4 groups [142]. This means tunneling modes are rare events and explains why finding them has been an open problem for nearly 50 years.

The above discussion showed how the picture of tunneling states can describe the anomalous behavior of glasses at low temperature. However, if we find any two-level system in the glass, the full quantum description requires solving the Schrodinger equation which appears in Appendix C.

APPENDIX C

QUANTUM MECHANICS OF DOUBLE-WELL POTENTIAL

To fully understand the quantum behavior of a two-level system, we should solve the Schrodinger equation for the double-well potential. If $\psi(x)$ and E represent the wavefunction and energy, respectively, the Schrodinger equation is:

$$H\psi(x) = -\frac{\hbar^2}{2m}\frac{d^2\psi}{dx^2} + V(x)\psi(x) = E\psi(x) \tag{C.1}$$

with $V(x)$ being the potential energy from Eq. B.1 and H is the hamiltonian. To solve the equation in a more traceable and general fashion, first we rewrite the Schrodinger equation for the double-well potential in dimensionless units. Let $2\lambda\delta^2 = d^2$, $x - a/2 = \delta z$, and $4\epsilon V_b = \lambda(E - V_b)$ (note that λ is the previously defined tunneling parameter but δ is newly defined). In the dimensionless form, the potential energy and the Schrodinger equation are:

$$\begin{aligned} V(z) &= V_b\left(\frac{2}{\lambda}z^2 - 1\right)^2 \\ H\psi(z) &= \left[-\frac{1}{2}\frac{d^2}{dz^2} - z^2 + \frac{1}{\lambda}z^4\right]\psi(z) = \epsilon\psi(z). \end{aligned} \tag{C.2}$$

Note λ, ϵ, and z are dimensionless but δ has the dimension of length. The above equation corresponds to a Schrodinger equation where $\hbar = m = 1$ with an energy eigenvalue of ϵ while the effective potential is $-z^2 + z^4/\lambda$. Note that the spacing between the original energy levels ΔE and dimensionless energy $\Delta\epsilon$ is:

$$\Delta E = (4V_b/\lambda)\Delta\epsilon. \tag{C.3}$$

If $\lambda \ll 1$, the potential is effectively quartic and we can qualitatively find the behavior of energy levels using Born-Sommerfeld condition. Let $z^4 = \epsilon\lambda y^4$ and z_0 denotes the

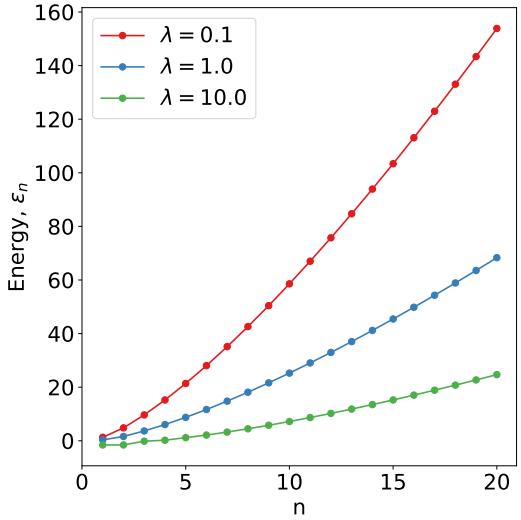

Figure C.1: Energy levels for dimensionless double-well potential for various values of the tunneling parameter, λ.

classical turning point for energy ϵ, we find:

$$\begin{aligned}(n-\frac{1}{2})\pi &= \int_{-z_0}^{z_0}\sqrt{2(\epsilon-\frac{z^4}{\lambda})}\mathrm{d}z \\ &= \int_{-1}^{1}\sqrt{2(\epsilon-\epsilon y^4)}\,(\epsilon\lambda)^{1/4}\,\mathrm{d}y \\ &= \epsilon^{3/4}\lambda^{1/4}\sqrt{2}\int_{-1}^{1}\sqrt{1-y^4}\mathrm{d}y \\ \Rightarrow \epsilon_n &\approx 1.37\left(\frac{1}{\lambda}\right)^{1/3}\left(n-\frac{1}{2}\right)^{4/3},\ n=1,2,3,\ldots. \end{aligned} \tag{C.4}$$

The energy levels of quartic potential grow as $n^{4/3}$, faster than the energy levels of a harmonic oscillator which grow as n. Obviously, the spacing between levels is also not constant. In fact, the Schrodinger equation of the full potential has no exact solution, and the $n^{4/3}$ scaling can be used as check for the following numerical procedure.

To find eigenstates and eigenenergies, we use the embedding method developed in Ref. [163] by expanding the eigenstate $\psi(z)$ in the basis of eigenstates of a square-well potential. From elementary quantum mechanics, the eigenstates of a square-well potential ϕ_n are sinusoidal functions confined between $0 < z < a$ with energy E'_n for

Table C.1: Eigenenergies of the dimensionless double-well potential

λ	ϵ_1	ϵ_2	ϵ_3	ϵ_4	$\epsilon_2 - \epsilon_1$
0.001	6.6511	23.8648	46.8691	73.2336	17.2137
0.01	3.0383	10.9556	21.5873	33.7826	7.9173
0.1	1.3022	4.8189	9.6557	15.2257	3.5167
1	0.3380	1.6127	3.6619	6.0508	1.2747
10	−1.5654	−1.5504	−0.1458	0.2121	0.0150

level n:

$$\begin{aligned} \phi_n &= \sqrt{\frac{2}{a}} \sin(\frac{n\pi z}{a}), \\ E'_n &= \frac{n^2\pi^2}{2a^2},\ n = 1, 2, 3, \ldots \end{aligned} \tag{C.5}$$

If we write ψ as a sum of ϕ_n's and then plug the sum back into the dimensionless Schrodinger equation, the eigenstates converge to that of Equation C.2 provided that $a \gg d$. In fact, the exact matrix representation of the Hamiltonian has the following form:

$$H_{mn} = n^2\delta_{mn}E'_1 + \int_0^a \mathrm{d}z\phi_m(z)\left(-(z-a/2)^2 + \frac{(z-a/2)^4}{\lambda}\right)\phi_n(z). \tag{C.6}$$

The eigenvalues of Hamiltonian matrix H are the energy eigenvalues ϵ. This method is very convenient since the integral can be evaluated using familiar numerical packages. Table C.1 lists the values for four smallest eigenvalues and the splitting between the first two energy levels. Figure C.1 shows the twenty smallest energies for various values of λ. Note that for $\lambda = 0.1$ the scaling is consistent with $n^{4/3}$ variation, derived in previous paragraph. For $\lambda \approx 10$ which is close to our expectation from the experimental data, the two low-lying states are inside the wells, very close in energy and far from other excited states and effectively a two-level system.

APPENDIX D

COMPUTATIONAL DETAILS

Research in physics increasingly benefits from computational tools and techniques. Over the course of my doctoral work, I have invested significant amount of time and effort developing software that are routinely used in my research and can potentially be used by other researchers. This appendix presents a summary of software used in this Dissertation.

I chose to write most of my research software in `Python` because of its flexibility and great collection of open source packages such as `Numpy` and `Scipy` which are nowadays fundamental for scientific computing with Python. However, some of more resource-intensive work were done in `C++`.

D.1 Structural Refinement

Chapter 4 discussed the refinement of silica bilayer structure in two dimensions. The atomic coordinates were found manually by selecting atoms on the microscopic images. With the advancement of microscopy techniques, it is expected to see more images from amorphous materials in the near future. It would be interesting to develop methods to automatically extract the coordinates of atoms, perhaps using object detection techniques in neural networks (especially convolutional neural networks) [164].

We can consider the structure of silica bilayer as a network of corner-sharing triangles. Hence each oxygen atom is connected to four nearest neighbors oxygens. KD-tree is an algorithm for quick nearest-neighbor lookup and an implementation exists in `scipy` as `scipy.spatial.KDTree`. I used this implementation to find four nearest neighbors for oxygen atoms. Note that, if an atom i is among four closest neighbors of another atom j, the inverse is not necessarily true. Therefore some atoms will be over-coordinated. The shortest bonds are maintained and others removed such that all oxygens have coordination 4.

Using coordinates and bonds, a glass structure is represented by these two lists. The coordinates are a list of N lines, for example:

```
6.17284    2.80260
6.55525    3.05472
6.41071    3.25547
...
```

Then each atom is labelled from 0 to $N-1$. This is convenient as both `C++` and `Python` have zero-based indexing for arrays. The connectivity list or edge list of the graph shows two ends of a bond:

```
0 3
0 13
1 2
...
```

After the determination of coordinates and bonds, the above two lists are imported in software, and a molecular dynamics program is used to find forces on atoms and to minimize the energy. The potential energy includes the known local chemistry such the chemical bond length. The total potential energy is a combinations of three contributions [9]: bonds as harmonic springs, mean-square deviation (MSD) from experimentally determined positions, and hard-core potential to avoid the overlap between oxygen atoms. Although employing MSD made the use of boundary conditions unnecessary, the studies were carried out on the effect of boundary conditions on realizations of a network of corner-sharing triangles (discussed in Chapter 3). In particular, the flexibility window of these networks are of great interest. To implement the anchored boundary conditions, the force on pinned atoms were set to zero.

For sliding boundary conditions, the force on surface atoms were projected onto a given vector which either was fed in as an input or was randomly generated.

D.2 Rigidpy

The network glasses such as silica are rigid structures. Rigidity theory has had a significant impact on our understanding of mechanical properties of materials. Rigidity theory studies the response of a material to mechanical deformations. My colleague Varda F. Hagh and I developed a `Python` library which provides a convenient API (application program interface) to study the rigidity of a network/graph. The library is named `Rigidpy` and extensively uses efficient vector operations present in `Numpy` and `Scipy`. The mathematical details and background are given in [165]. It is freely available at `https://github.com/vfaghirh/rigidpy`. The library has three main components:

1. **Framework rigidity**: The collection of a graph and an embedding (assigning coordinates to vertices) of that graph is called a framework. This submodule creates the framework from coordinates and edge list of the structure. The framework object can be used to compute rigidity matrix, stress matrix, Hessian matrix, dynamical matrix, and finding eigenvalues and eigenvectors of dynamical matrix. Various boundary conditions are implemented, as well.

2. **Geometrical optimization**: This submodule optimizes the the graph geometry and finds the closest local energy minimum for the given edge lengths.

3. **Circuit Follower**: To find realizations of a graph with zero energy, `CircuitFollower()` can be used. The submodule is built based on `Framework` object, and `id` of a bond to be removed is passed as an input. `CircuitFollower()` follows the non-trivial eigenvector of the dynamical matrix with zero eigenvalue. The traversal

is done in small steps (step size is adjustable) to ensure that the error remains within the acceptable range. The stopping criterion is where the root-mean-square-deviation of the current coordinates from the original coordinates is less than the set value, which is given as an input. This function returns a `dictionary` object containing coordinates of vertices, the distance between two ends of removed edge, etc and can be used to plot the projected circuit. This submodule was used in Chapter 5.

To see a detailed "How to" guide on rigdipy, please see: `https://github.com/mahdisadjadi/rigidpy_manual/blob/master/rigidpy_intro.ipynb`.